Wesleyan University

Planet Hunting and Characterization with K2

by

Prajwal Niraula
Class of 2018

A thesis submitted to the
faculty of Wesleyan University
in partial fulfillment of the requirements for the
Degree of Master of Arts
with a Planetary Science Concentration

Middletown, Connecticut April, 2018

We can now say, with statistical certainty, that there are more planets than stars in the galaxy.

—Jill Tarter at AAS 229

Acknowlegdments

Thanks to Wesleyan's Astronomy Department for providing me with a home where I could explore and pursue my passion. I am grateful to Prof. Seth Redfield for helping me to find the spirit of an exoplanteer within myself. Thanks for leaving your door open for any discussions, and letting me bother you with all sort of questions bubbling in my head. I am also thankful to P. Wilson Cauley and Girish Duvvuri, both of whom helped me getting started in the early days of my research. And I cannot help thanking Markov Chain Monte Carlo maestro Kevin Flaherty, not only for his help with MCMC but also with any questions related to planetary science and disks forming planets. Also, Ismael Mireles deserves a special thanks for his work to improve our existing pipeline. And I also want to thank Ryan Adler-Levine for his discussions on the Trojan objects. Prof. Roy Kilgard should get the sincerest apologies and thank you, for it was him who I bothered when there were computer and network issues.

In the course of my research, I got a chance to collaborate with `KESPRINT`, an exoplanet group bringing experts from different continents. The discovery paper and subsequent analysis of the GJ 9827 system presented in this thesis would not have been possible without such opportunities. I am particularly thankful to Prof. Davide Gandolfi from University of Torino, Italy for his role in making this collaboration effort work.

And special thanks goes to to Evan Carter, with whom I shared the office for two years. His cheerfulness lightened the whole basement, if not the whole astronomy department. Thanks to Sophia Flury for making those coffee runs to the graduate student office. Also thanks to Zach Lambros, Cail Daley, Kristen Luchsinger, Simon Wright, Avi Stein, Gloria Fonseca, Rachel Aronow, Julian Dann, Jessica Klusmeyer, Julia Zachary, Hunter Vannier, Michel Henderson, Terra Ganey and Jonas Powell for making the basement the best place to be. Also thanks to friends from Earth and Environmental Scic department Melissa Luna, Reid Perkins, and John Hossain for making Wesleyan a more holistic experience. I am glad that our paths crossed, and hope they cross again in the future.

Additionally, I want to thanks my parents who have shared the ups and downs of my research, and patiently heard my complaints when things did not work. Their moral support has been very crucial in bringing this work to a conclusion. And lastly, I must also thanks *K2* team at NASA, who made *K2* such a successful mission and thereby has made a lot of research, including this work, possible.

Contents

Chapter 1

Introduction

We have entered into a different era of exoplanet research. No longer are we asking whether exoplanet exist or not. Our questions have become deeper and more discerning. The scientific quest for the search for exoplanets started as early as the 1950s, when brilliant astronomers of the day such as Otto Struve conjectured about the existence of exoplanets based on the argument of the angular momentum conservation (Struve 1952). Should all the angular momentum of the nebular cloud be present in the star, the star would have to spin too rapidly to be stable, therefore most of angular momentum has to be imparted and planet formation was the way of of doing so. For instance, in our own solar system, while circa 99% of the mass is locked in the Sun, more than 98% of the angular momentum is distributed among the planets. This inspired early astronomers like Struve to start looking for planets around other stars. Struve was not alone in hypothesizing on the existence of the exoplanets, and most of the astronomers going back to the sixteenth century such as Giordano Bruno believed in the existence of planets around other stars primarily based on the Copernican argument that nothing is special about the Earth or the solar system, ergo there should be other systems like ours in the Universe.

However, turning scientific hypothesis into scientific fact is not an easy task, and often requires growth and maturation of suitable technologies. The progress in the field of exoplanets lends insight into how science itself works. For three decades, the field fumbled its way through the dark passage to discovery of the first exoplanet. During this course, discovery claims were made (van de Kamp 1969) and falsified (Black 1980). And every failure led to new understandings, and showed how daunting the challenge itself is. Finally, the first undisputed discovery of the planet by astronomers was made by Wolszczan & Frail (1992) around a pulsar using pulsar timing variation. A few years later, a planet around a sun-like star was discovered by Mayor & Queloz (1995) using the radial velocity (RV) technique. By this time, given the complicated history of false discoveries, the authors were extra-cautious in the claim. Luckily, they were shortly vindicated by verification through another independent group (Marcy & Butler 1995). The discovery served as the cornerstone in the history of exoplanet research showing the technology had come along a long way. Thus, spawned a whole new area of astronomy - the field of exoplanets, where the progress today only appears to be accelerating.

Before we talk about how we discover and characterize exoplanets, it becomes important to define the term - what is a planet? In light of many trans-Neptunian objects discovered in 2006, the International Astronomical Union (IAU) redefined the planetary criteria in resolution B5: "A planet is a celestial body that (a) is in orbit around the Sun, (b) has sufficient mass for its self-gravity to overcome rigid body forces so that it assumes a hydrostatic equilibrium (nearly round) shape, and (c) has cleared the neighborhood around its orbit." Using this definition, Pluto was demoted to dwarf planet. However, this definition does not strictly apply to exoplanets. For instance, due to gravitational interaction, sometimes planets can get ejected out from the system rendering the first criterion not universally applicable. Such planets are called Steppenwolf planets or rogue planets (Abbot

& Switzer 2011), and are expected not only exist, but some of them might already been detected (Delorme et al. 2017). Also, not all planets may be in stable states due to dynamical interactions, rendering the third criterion that was invoked to demote Pluto often difficult to be strictly applied to the field of exoplanets. Besides, it is hard to characterize the orbital parameters of exoplanets with same precision as solar system planets. Thus, using a strict definition as has been adopted for the solar system planets may not be the right way to go about this. The best alternative might be coming up with a general definition as was done by Soter (2006): "A planet is an end product of disk accretion around a primary star or substar." Of course, there are problems with this definition. However, given the diversity of the exoplanets, it may almost be impossible to come up with a single neat definition that will capture the essence of every single planets that have been discovered. And exoplanet, also sometimes referred to as extra-solar planet, is any planet that lies outside our solar system or does not revolve around the Sun.

1.1 Detection Techniques

Many techniques have been used over the years for the detection of exoplanets. While the first exoplanets were discovered using the pulsar timing variation, most of the planets today are found using transits, and RV method. At the same time, there are other emerging and promising methods such as direct imaging, astrometry and gravitational lensing. In addition, there are many discovery methods as shown in Figure 1.1 such as the orbital brightness modulation or transit timing variation which are more involved methods that build on traditional photometry. These techniques are varied, and in many cases, complementary to one another.

Techniques such astrometry still has not made an incontestable discovery (the one shown in Figure 1.1 turned out to be a brown dwarf (Sahlmann et al. 2013)), although with *Gaia*, a multiyear scale astrometric survey (Lindegren & Perryman 1996), this status is likely to change. In fact, *Gaia* might even become the most prolific instrument to discover exoplanets as one of the estimates expects *Gaia* to be able to detect around 70,000 ($\pm$ 20,000) planets, most of which will be within 500 pc (Perryman et al. 2014). In this section, I will however be focusing on transits and RV methods as these are two main techniques I have used for planet discoveries and characterization in the following chapters.

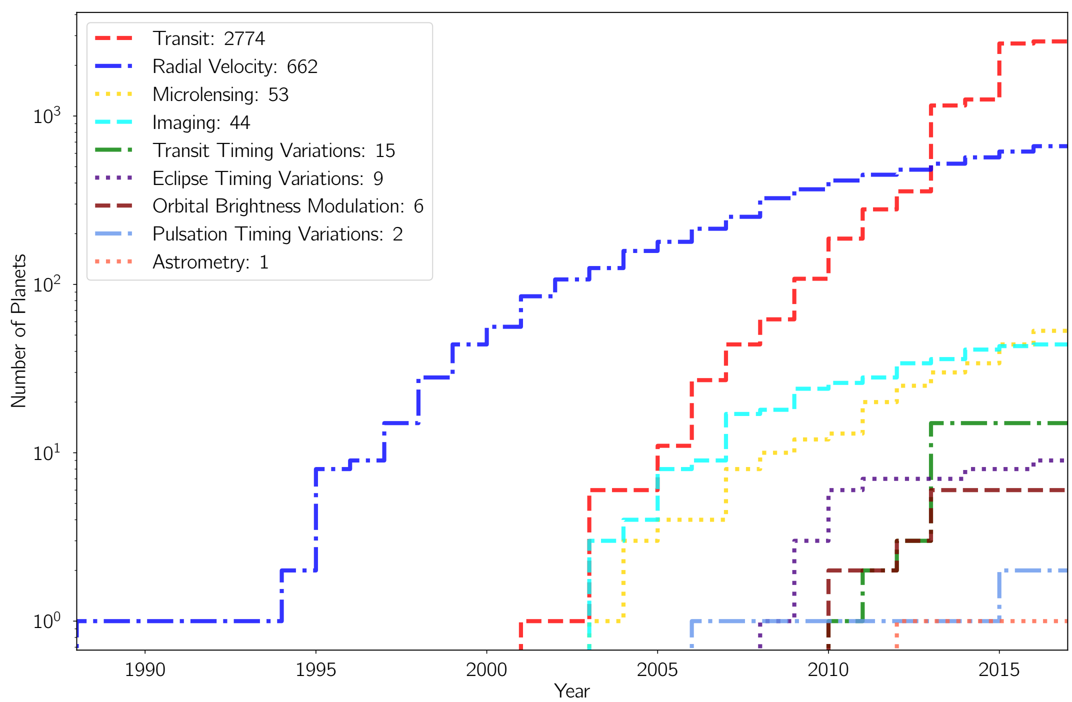

Figure 1.1: Cumulative numbers of planets discovered per year by different detection method in years leading up to 2017 as is recorded in exoplanetarchive.ipac.caltech.edu. Transit method currently dominates the number of the planet discovered with around 3000 discoveries.

1.1.1 Transit Method

Transit search is the most successful techniques for discovering exoplanets to date. The success of this technique comes from the space missions such as COnvection ROtation and planetary Transits *CoRoT* (Bordé et al. 2003), a pioneering European mission, and *Kepler* (Borucki et al. 2010) which provided continuous temporal coverage with a high duty cycle (∼92%). In addition, these missions have been able to achieve very high photometric precision of 10–100 ppm for typical targets, which is much better compared to ground observation by avoiding the turbulent atmosphere of the Earth, and have facilitated an unprecedented progress in fields such as asteroseismology (Lund et al. 2017) as well as phase curve studies (Esteves et al. 2013). But ground based photometric observations also have made some significant contributions in the discovery of transiting planets. For instance, the now famous TRAPPIST-1 system was originally observed by a ground telescope (TRAPPIST) when transits from 3 super-Earths were originally identified. It was then followed up with *Spitzer*, which led to discovery of additional 4 planets (Gillon et al. 2016). With the future missions reaching even better precision and looking at even more extensive lists of targets such as Transiting Exoplanet Survey Satellite (*TESS*) (Ricker et al. 2015) recently launched on April, 18 2018, and CHaracterising ExOPlanet Satellite (*CHEOPS*) in 2018 (Broeg et al. 2013), PLAnetary Transits and Oscillations of stars (*PLATO*) in 2022/24 (Rauer et al. 2014a), and Atmospheric Remote-sensing Infrared Exoplanet Large-survey (*ARIEL*) in 2026 (Puig et al. 2016), the number of planets discovered by transit is on the verge of rising even more dramatically.

A transit, however, does not happen in every system that hosts an exoplanet. A special geometrical arrangement, that the planet inclination is closer to 90° is

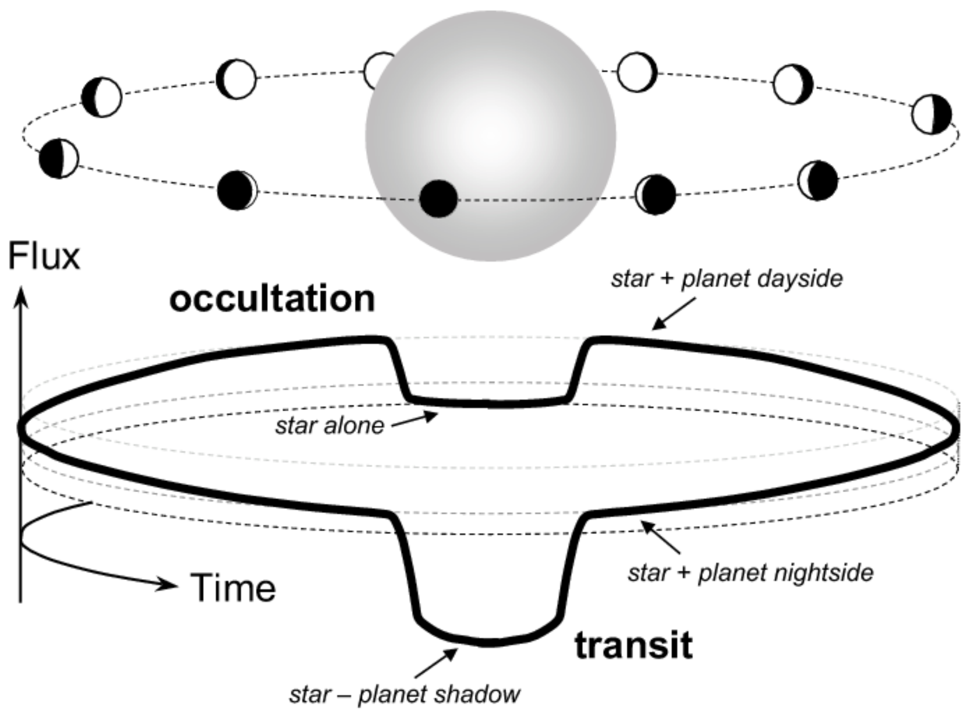

Figure 1.2: Figure showing the occurrence of transit and occultation adopted from Winn (2010).

required. As shown in Figure 1.2, during transit the secondary object (planet) passes in front the primary object (star). The secondary eclipse or occultation occurs when the secondary object passes behind the primary object. For a circularized orbit the two are separated by a phase of 0.5, but not for an eccentric orbit. In fact, the timing of the secondary eclipse can help to precisely constrain the orbital parameters such as eccentricity (Huber et al. 2017).

Transits can provide various information on the planet itself. It gives a direct measure of the size of the planet with respect of its host star by measuring the transit depth (δ) as in Equation 1.1:

$$\delta = \left(\frac{R_p}{R_*}\right)^2, \tag{1.1}$$

where R_p is the planetary radius and R_* is the stellar radius. However, transit fitting allows more orbital parameters to be constrained strongly such as scaled semi-major axis (a/R_*), inclination (i), and impact parameter (b). Parameters such as eccentricity (e) and argument of periastron (ω), however can only be poorly constrained. The primary source of this constraint comes from the shape of the transit itself. For instance, transit duration depends on the period (P), the scaled semi-major axis (a/R_*), and impact parameter (b) as below:

$$T = \frac{P}{\pi} \sin^{-1} \left[\frac{R_*}{a} \frac{\sqrt{(1+\sqrt{\delta})^2 - b^2)}}{\sin i} \right]. \tag{1.2}$$

Transit methods have also empowered the exoplanet community in venturing into new arenas of science. With *Kepler*, the expected photometric precision is 25.4 ppm for $V = 12$ for 30 minutes cadence (Borucki et al. 2008). This in turn has allowed astronomer to start looking for exo-moons (Heller 2018) and Trojan objects (Hippke & Angerhausen 2015). Additionally, such precise photometry has allowed the discovery of non-transiting planets as was the case of Kepler-76b through phase curve modulation (Faigler et al. 2013), the details of which will be dealt in the Chapter 4. Note that often the primary bottleneck for precision is shot noise of the source itself. By using a larger collecting area or a longer integrating time, it is often possible to obtain a higher precision light curve. However, using a longer integration time than the transit itself dilutes the signal, thereby making it harder to detect. For a star like our Sun, 30 minute cadence used by *Kepler* is a reasonable time scale, but for for stars like white dwarf transits for which transits are shorter by a factor of 5–50 for similar orbital configuration, and smaller cadence would be preferable. Although, most of the white dwarfs are very faint, thus the detection threshold is often limited by photon noise itself.

The most fundamental parameter of a planet that is not directly constrained by transit, is its mass, which requires other complementary methods such as radial velocity or astrometry. Such complementary methods are also desired because it is hard to validate the signal from transit alone, which often tend to have higher false positive probability. There are ways in validating a planetary signal using the fit parameters. One of the way is to estimate the stellar density as follow:

$$\rho_* \approx \frac{3\pi}{GP^2}\left(\frac{a}{R_*}\right)^3. \tag{1.3}$$

Gauging the plausibility of stellar density can provide indications in regards to the validity of the signal itself. Yet, such validation alone is not sufficient in distinguishing false positives caused by certain astrophysical phenomena such as eclipsing binaries. This has led to the development of more sophisticated statistical tools such as `vespa` (Morton et al. 2016), which can give a reasonable estimation of the false positive probability. But even this tool is not foolproof (e.g. Cabrera et al. 2017; Shporer et al. 2017), and has to be used with caution. However, precise photometry can sometimes open doors for validation just by looking at the ellipsoidal variation usually for hot Jupiters (Mislis & Hodgkin 2012). Again, there are only a handful targets for which such validation procedures are possible.

Kepler/K2

Kepler has a prolific history of planet discovery. Launched on March 6, 2009, it monitored around 150,000 main sequence stars while orbiting in a heliocentric Earth trailing orbit. It observed a patch of the sky with an area of 110 square degrees for four years (Borucki et al. 2010). However, with the failure of two reaction wheels, *Kepler* was repurposed as *K2* (Howell et al. 2014). In order to attain a stable pointing, *K2* uses radiation pressure from the Sun and its symmetrical design for the roll angle drift. This technique has led to achieve photometric precision rivaling the original *Kepler* mission (80.5 ppm for $V = 12$ magnitude star compared to 25.4 ppm) through some data processing. More on the *K2* data reduction and the detrending process will be discussed in Chapter 2.

Unlike the original mission, *K2* has widened its net with more diverse targets. This led to the discovery of a disintegrating planet around a white dwarf (WD 1145+017 Vanderburg et al. 2015), a five planet multiplanetary system K2-138 (Christiansen et al. 2018), planets in the Beehive Clusters (Obermeier et al. 2016) as well as discoveries of more than 200 more exoplanets. *K2* also has tried to accommodate other science with Campaign 9 dedicated to gravitational microlensing effects, and Campaign 10 dedicated to the study of dwarf galaxies. *K2* also have been used in studying optical variability of Active Galactic Nuclei (Aranzana et al. 2018) and in this current campaign (Campaign 17) will be probably be providing an unparalleled supernova light curve.

TESS

TESS lauched on April, 18 2018 6:51PM EST. Orbiting in a 13.7 days elliptical orbit around the Earth, the satellite will observe almost all of the sky during its operation. With four cameras on board, it will simultaneously observe an area of 2300 deg^2 at any time, and due to its closer proximity to the Earth than *Kepler*, the data can be downloaded at higher downlink speed. The number of planets discovered by *TESS* is expected to far surpass the number of discoveries by *Kepler*. Sullivan et al. (2017) predicts discoveries of about 20,000 new planets with *TESS* during its two years of operation as shown in Figure 1.3. *TESS* will observe almost full sky, with observation time scale of different fields ranging from

27.4 days to 351 days, the longest observed region at ecliptic poles coinciding with the Continuous Viewing Zone of *James Webb Space Telescope (JWST)*. This is because one of the primary goals of *TESS* is to find planetary candidates which are ideal for atmospheric characterization with *JWST*. While there are handful of optimal targets that *JWST* can look at, *TESS* is expected to quite extensively expand the list. In addition, since *TESS* targets are 10–100 times brighter than those surveyed by *Kepler*, most of the planetary candidates could be followed up with RV observations.

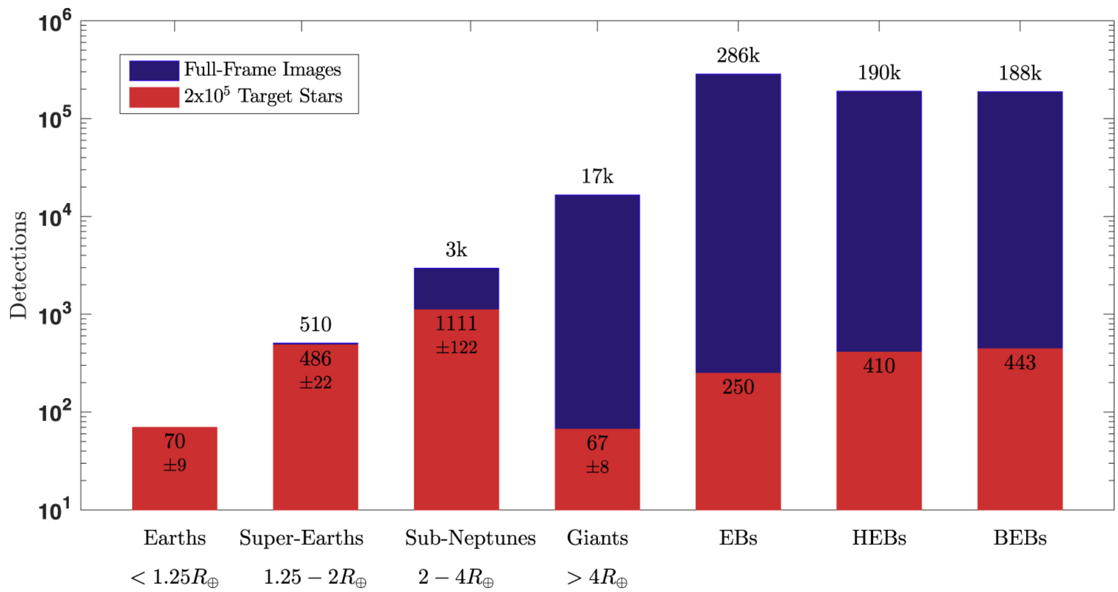

Figure 1.3: Size distribution of different planets expected to be discovered with *TESS* as reported in Sullivan et al. (2017).

1.1.2 Radial Velocity

Radial velocity (RV), also known as wobble method, is one of the earliest techniques developed for detecting exoplanets. With 662 planets discovered in this way in the years leading up to 2018, RV is a mature technique. It has come a long way with a series of technological improvements over the course of the

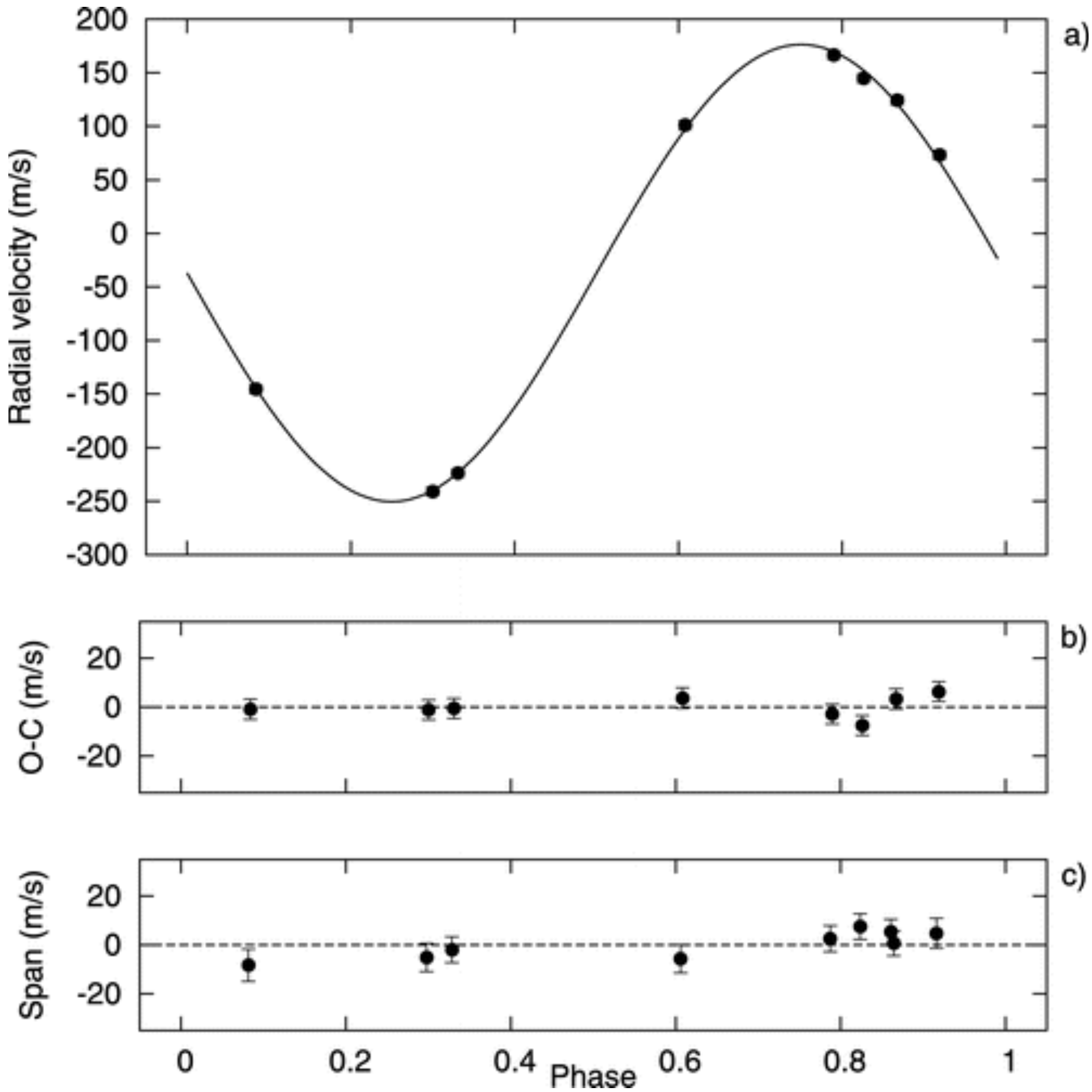

Figure 1.4: The RV measurement of HAT P 7b reported Pál et al. (2008) along with the fit. The O-C is figure in the middle planet shows the residual of the fit.

twentieth century tackling different issues in order to improve its precision. As the planet moves around the common center of mass, the star also moves around it with the same characteristic period as the planet. This movement of the star can be measured by measuring the shifting spectral lines as the star moves away or towards the line of sight. The precise nature of this shift over the orbital period is determined by the mass of the star, mass of the planet, period, eccentricity, inclination, and angle of periastron. For a circular orbit, a sinusoidal variation is expected as is seen for HAT-P-7b planet (Figure 1.4). The RV technique does not provide the mass itself, but an upper constraint on the mass of the planets. There is a degeneracy between the inclination and the mass of the secondary object as shown Equation 1.4, which is not possible to disentangle from RV observations alone. Only by using complementary methods such as transit or astrometry, the actual mass can be determined. Yet, not many planets ($< 5\%$) discovered through RV is likely to be transiting. The semi-amplitude K_1 of the RV method is given by:

$$K_1 = \frac{28.4329\ m\ s^{-1}}{\sqrt{1-e^2}} \frac{m_2 \sin i}{M_{Jup}} \left(\frac{m_1 + m_2}{M_\odot}\right)^{-2/3} \left(\frac{P}{1yr}\right)^{-1/3}, \tag{1.4}$$

where m_1 is the mass of the primary object (star), m_2 is the mass of the secondary object (planet), e is the eccentricity, and P is the period in years. The mass of the primary object (m_1) can be spectroscopically measured, and eccentricity (e) as well as period (P) can be obtained by fitting RV data as shown in Figure 1.4.

1.2 Importance of Exoplanetology

Exoplanetology, at its heart, is trying to answer the questions that humanity have wondered since being captivated by the stars in the night sky - why do we exist, and how did we come to be? We have divided and conquered different parts of this puzzle: the birth of the universe, the formation of the solar system, the beginning of life in the Earth, and the evolution of unicellular organism all the way to human beings. Not all of these questions have been answered to the same level of satisfaction. And for a long time, the evolution of planets remained a harder problem to solve as for most of the scientific history we were but stuck with a single system that could be studied. Now armed with the new discoveries, we have not only learnt about the exoplanets but can also have been able to put our own solar system in the context of larger numbers of planetary systems.

When planets as hot Jupiters were discovered in very close orbits to their host stars, astronomers realized that planetary configurations are not as stable as were originally imagined. This led to the development of formation models of solar system such as the Nice model, which include short violent events such as Uranus and Neptune switching their ordering (Tsiganis et al. 2005). Besides, we now know that our solar system is not a typical planetary system. In our search for exoplanets, we discovered planets in orbits much closer to the star itself than Mercury, and a distribution of size looking like Figure 1.5. Many of these planets have orbital radius smaller compared to orbital radius of Mercury. Secondly, there are no super-Earths or mini-Neptunes in the solar system which are the most common type of exoplanets so far discovered.

But perhaps the most vital question that we are trying to solve with exoplanets is about the occurrence of exolife. The primary mission for *Kepler* was to find Earth like planets around Sun-like stars. As the reaction wheel broke at the beginning of the fourth year, the original mission had to be discontinued, which has been particularly detrimental to finding long period planets. But fortunately, short period planets were more numerous than expected. Most of these planets are too hot to sustain lives. However, for smaller stars, habitable zones occur at a closer distance to the host star i.e., shorter period orbits, which are easier to find with short term transit surveying missions. Also as shown in Equation 1.4, the RV technique prefers lower mass stars. Thus, the last couple of years have seen a major push for looking the planets around the smaller stars, which is what

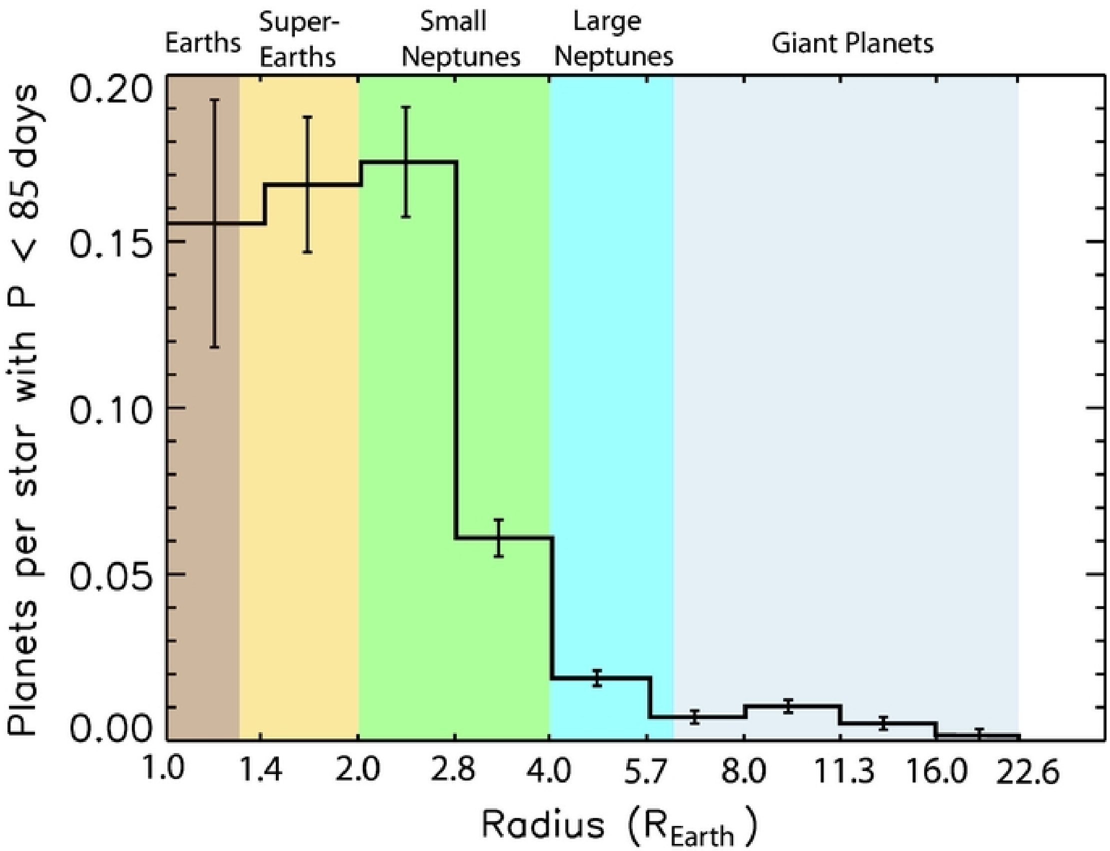

Figure 1.5: Planetary size distribution occurrence calculated for main-sequence FGKM stars from the Q1–Q6 *Kepler* data adopted from Fressin et al. (2013).

TESS will be particularly focusing on.

With thousands of planets discovered, our pursuit of exolife is going through a rapid development. Analogous to the solar system, late-G to mid-K stars are usually considered promising grounds for exobiology (Cuntz & Guinan 2016). However, the question about habitability remains complicated as ever. One of the fronts where gradual progress has been made is in the atmospheric characterization. Such ideas started in our own solar system when we made observations of the Earth's atmosphere using *Galileo*. The detection of spectral signatures of methane along with oxygen was interpreted as biomarkers of the Earth (Sagan et al. 1993), all that remains is to do conduct similar studies for exoplanets. However, we know that atmosphere of the Earth looked different at different epochs over the course of its history (Kaltenegger et al. 2007). Given this, using biomarkers to detect the uncontestable signs of exolife will always be a tricky business. Also, unfortunately, the transmission spectroscopy would only be possible for a handful of planets, and most of them with temperature too hot to be habitable. This was one of the reasons the TRAPPIST-1 system discovery was welcomed with a great excitement, as it has three planets, TRAPPIST - e, f, and g, that are in the classical habitable zone of the system, zone where liquid water can exist. But even in TRAPPIST, questions has been raised about the habitability given a number of flares were observed, which is bound to have effects on the climate of the planets (Vida et al. 2017).

Given the never ending debate surrounding habitability, one of the promising ways to settle the debate would to be send probes to directly image the exoplanetary systems. And we are indeed aspiring to send relativistic probes, a project known as Breakthrough Starshot (Kipping 2017). The concept involves using light-sails and radiation pressure of giant lasers to propel small robotic chips at about 20% of speed of light to Alpha Centauri system (Lubin 2016). But even at this speed it will take 20 years to reach the system, and 4 years to send the data back to the Earth. The recent finding of a planet in a classical habitable zone (Anglada-Escudé et al. 2016) orbiting Proxima Centauri as well as the disk surrounding the Proxima Centauri (Anglada et al. 2017) might now provide a stronger motivation for the mission.[1] But with this previously uncharted technology, the feasibility of the project itself is still under question. However, if successful, this would be a very remarkable feat for all of the scientific community.

[1]Although, the presence of the disk has been more recently disputed by MacGregor et al. (2018).

Keeping all of these things aside, let us for a moment assume that we found that intelligent life forms in another planet. The implications in terms of philosophy, religion and economy is unimaginable. We may not realize that these days may be nearer in the future than we think. But there is a long way to go forward, and there are also major technological hurdles awaiting us along the way. Hence, while it may appear that we have a made a major dent in the field of exoplanet, all we have done is merely scratched the surface. The most exciting feats and discoveries, I believe, are still to come.

1.3 Summary of Contents

This thesis will primarily deal with the selected targets observed by *K2*. The details of reduction process and vetting process will be described in Chapter 2. A triple planetary system (GJ 9827) was discovered among the stars in our Campaign 12 targets and the detailed analysis on this system will be presented in detail in Chapter 3. In Chapter 4, I will describe the analysis of phase curves among the discovered K2 planets. In the same Chapter, I will discuss how phase curves can lead to the detection of Trojan objects, and the attempts to date on this front. This will be followed up with a short conclusion and the ideas for the future work and their prospects.

Chapter 2

Data Reduction

When the second of the four reaction wheels on board *Kepler* broke down in 2012, the repurposing of the most precise operating photometer led to the birth of *K2*. Balancing against the solar radiation pressure using the symmetrical geometry of the spacecraft, *K2*'s field of view drifts over its observation time, which is then corrected by firing the thruster in the direction opposite to the drift every 6-8 hours. This ingenuity allowed *K2* to achieve photometric precision rivaling the original *Kepler*, despite operating on only two reaction wheels (Howell et al. 2014), which theoretically speaking allows pointing stability in only two directions. However, it also meant that *K2* required more subtle handling of data than *Kepler* mission, as well as a rigorous data processing methods.

What *K2* lacked in the observation baseline, it more than made up in the diversity of the target choices. *K2* observed various parts of the ecliptic as shown in Figure 2.1 with a typical observation duration of around 80 days. And like primary *Kepler* mission there are primarily two modes of observation: short cadence (SC) with integration time of 58.8 s, and long cadence with integration time of 29.4 minutes. By studying a diverse range of targets, *K2* has led to some exciting discoveries such as a disintegrating planetary objects around a white dwarf (WD 1145+017) (Vanderburg et al. 2015), a multi-planetary system with five planets (Christiansen et al. 2018), re-monitoring of TRAPPIST system (Luger et al.

2017), and planet occurrence rates in cluster environments (Obermeier et al. 2016). Besides, the overlaps between different campaigns such as Campaign 5 (Apr 24, 2015 – Jul 11, 2015), Campaign 16 (Dec 7, 2017 – Feb 25, 2018), and Campaign 18 (May 12, 2018 – Aug 2, 2018), will provide some long term observation baselines (refer Figure 2.1). All of these things in combination have made *K2* an enviably successful mission.

2.1 Reduction Strategies

In order to address these new data issues, many research groups have built their own detrending methods for *K2*. These methods can be largely divided into two major categories: parametric, and non-parametric. One of the most popular parametric detrending algorithm is Self Flat Fielding, which was adopted from *Kepler*, and improved for *K2* by Vanderburg & Johnson (2014), and Vanderburg et al. (2016). Perhaps, their readily made available light curves after each campaign has served in heightening its popularity. The main assumption going into `K2SFF` detrending is that the brightness of the targets remains constant over short duration, and the major change in flux comes from the drifting of the target outside of the aperture. This creates a very characteristic light curve with a sawtooth pattern (see Figure 2.2). While different pixels have different responsivity, the idea is that as the star drifts across the aperture the loss of flux captured takes some arbitrary functional form which can then be removed by modeling it. However, when the target is rapidly fluctuating on time scales shorter than six hours, `K2SFF` has a hard time producing a good light curve.

Other detrending algorithms like `K2Phot`[1] (Van Eylen et al. 2016) have used

[1] https://github.com/vincentvaneylen/k2photometry

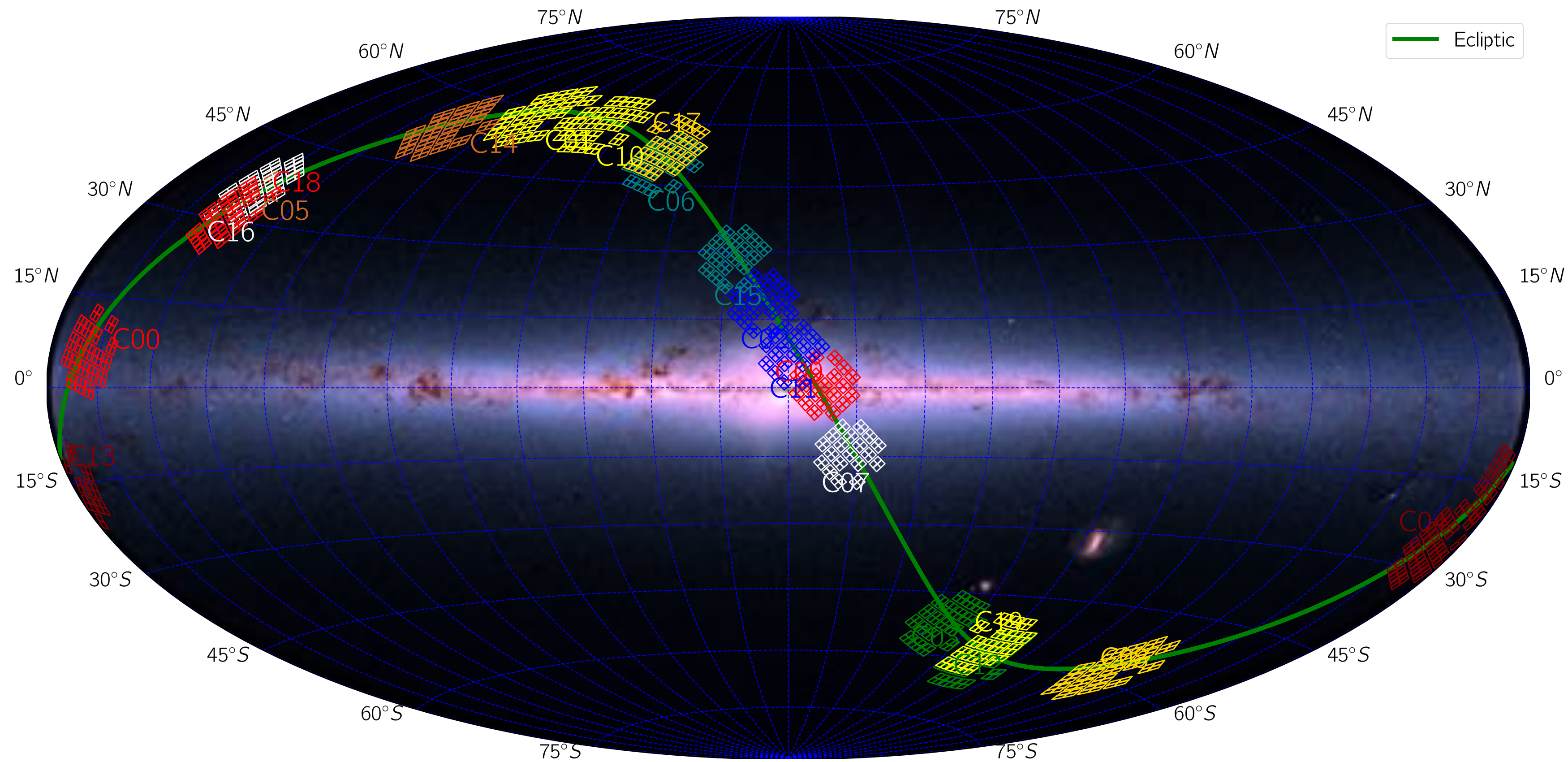

Figure 2.1: Different K2 fields of observation in galactic coordinates up to Campaign 18 are shown. *K2* observed different parts of the ecliptic planet with field overlapping between subsequent campaigns. Note that Campaign 5 and Campaign 18 fields overlap perfectly.

multi-dimensional dependency on the centroid variables as below:

$$M = t_0 + t_1 T + x_1 X_c + x_2 X_c^2 + y_1 Y_c + y_2 Y_c^2 + z X_c Y_c, \tag{2.1}$$

where the X-centroid (X_c) and the Y-Centroid (Y_c) were used independently for fitting, while also allowing a cross term between the two centroids. Note that $t_{0,1}$, $x_{0,1,2}$ and $y_{0,1,2}$ are coefficients that are determined by fitting the data with least square fit methods. This code is publicly available, and I have extensively used this method for detrending. Another parametric approach was suggested by Huang et al. (2015) by using a different functional form as in:

$$\begin{aligned} f(m) = c_0 &+ c_1 \sin(2\pi X_c) + c_2 \cos(2\pi X_c) + c_3 \sin(2\pi Y_c) + c_4 \cos(2\pi Y_c) \\ &+ c_5 \sin(4\pi X_c) + c_6 \cos(4\pi X_c) + c_7 \sin(4\pi Y_c) + c_8 \cos(4\pi Y_c), \end{aligned} \tag{2.2}$$

where c_i are the coefficients which are to be determined by fitting, $f(m)$ is the modeled flux, and X_c, Y_c represent the centroid of the target star. In addition, Huang et al. (2015) focused on finding the centroid of the targets with greater precision by using an astrometric solution because the photometric precision is often directly related to the positional precision of the stars. In my code, I have chosen a polynomial as the functional form, primarily because it is easier and computationally less expensive to fit a polynomial than sinusoidal functions. However, using the latter functions would probably be better when it comes to identifying the intrinsically periodic signals of a stellar light-curve.

Among the non-parametric approaches, the most popular one is `Everest` (Luger et al. 2016), which is able to produce light curves rivaling the photometric precision of `K2SFF`. It was developed by Deming et al. (2015) for *Spitzer*, which is referred to as Pixel Level Decorrelation. `Everest`, in particular, is agnostic in terms of the functional form of the light curve and uses a higher order of pixel level decorrelation and combines it with Gaussian Process to obtain its final light curve. This approach allows `Everest` to detect the contamination of eclipsing binaries in the background, which in other detrending methods such as `K2SFF` has passed as the planetary signals (Cabrera et al. 2017). A Gaussian Process based, but still a parametric approach in that it hyperparametrizes the data, is taken by `K2SC` which models the stellar light curve while taking into account pointing induced errors, stellar intrinsic variability and white noise (Aigrain et al. 2016). Another non-parametric approach is referred to as eigen-light curve, which used light curves of different stars within a campaign as basis vectors to model the light curve of the target star. This method was developed as proof of concept for targets in Campaign 1 (Foreman-Mackey et al. 2015).

A comprehensive comparison of different methods to understand the strengths and weakness of different pipelines has yet to be done, as such an undertaking would require a deep understanding of different arrays of pipelines. This is further complicated by the fact that not all the codes are publicly available. For most of the targets, the photometric precision of the most pipelines are not very different, but when it comes to “harder” targets - targets with shallower transits, rapidly varying stars, or targets with atypical or variable light curves, it becomes important to be aware of the artifacts that can be introduced by the different pipelines. Such an undertaking, however, lies beyond the scope of this thesis. I will be mindful of this fact when it comes to phase curve modulation, and will use light curve from different detrending algorithm. But most of the detrending algorithm produce light curves of similar quality as can be observed in Figure 2.3, and Figure 2.4.

Unlike *Kepler*, *K2* does not come with pre-defined aperture. In the `K2SFF` pipeline, a 2D Gaussian function was fitted in each frame to get the centroid of the target. Using such a fitting procedure is known to produce better results when the field is crowded, or when there is blending of the sources, or the primary target is located at the wing of a brighter variable source (Lund et al. 2015). For such crowded fields and dimmer targets, a PSF based photometry performs better as has been demonstrated for some of the crowded field in *K2* such as M35, Praesepe, and M67 clusters (Libralato et al. 2016; Nardiello et al. 2016). Since we do not deal with such areas, I have not modified our code to handle increased complexities that comes from a very crowded field. But this is something I am looking to implement in the future.

For this research, I have implemented `K2SFF`, whose code is not publicly available. The primary idea in this method is to use the eigenvector of the drifting centroid of the stars to find the direction of maximum change, rotate the drifting centroids in the direction of the maximum change, and fit a high order polynomial between the drift distance (arclength) as a function of locally normalized photometric variation. In this chapter, I will demonstrate the process of detrending using EPIC 212110888 or K2-34. K2-34 is known to host a Jupiter-sized exoplanet (Hirano et al. 2016; Lillo-Box et al. 2016; Brahm et al. 2016), and I will be showing how our version of `K2SFF` or `K2Phot` will be able to detrend, and detect the planet without much trouble. I will also point out anything I have chosen to do differently and the reasons behind it.

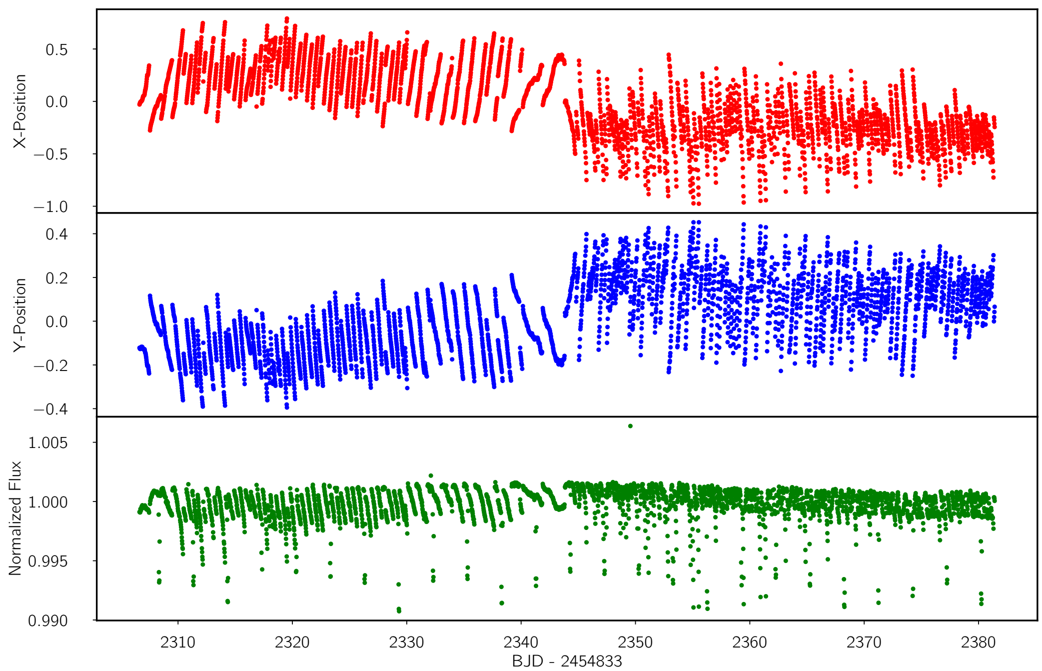

Figure 2.2: The drifting of the star though centroid and the characteristic saw-tooth nature of the flux.

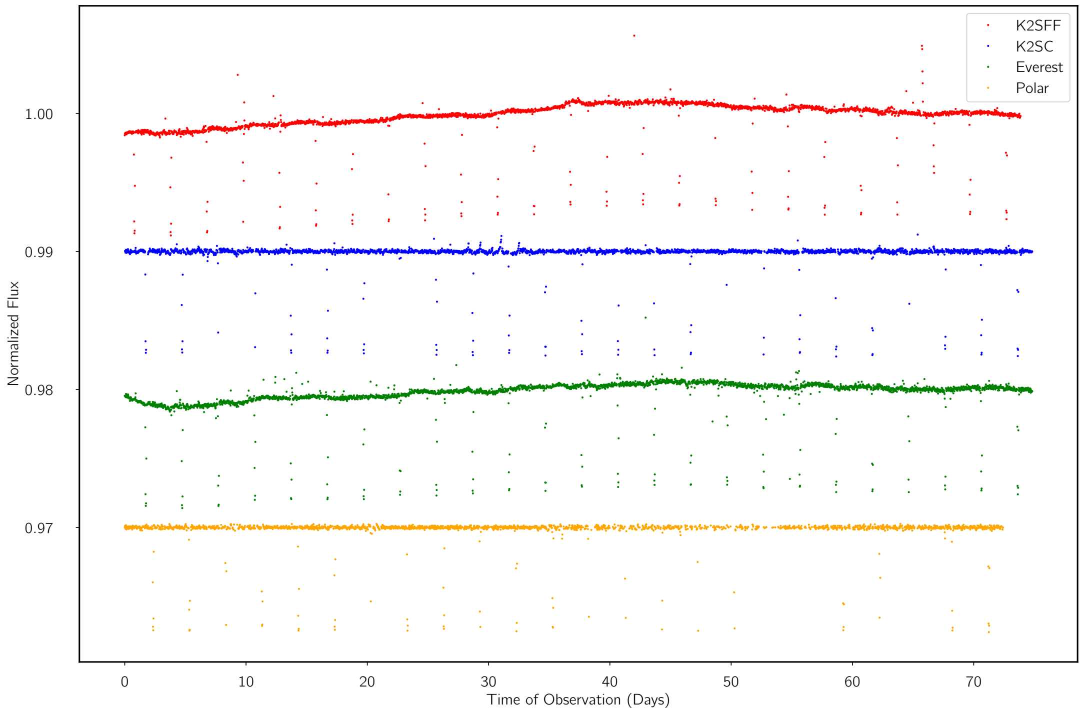

Figure 2.3: Light curve from different pipeline for target EPIC 212110888 or K2-34. The light curves obtained from different detrending algorithm are offset for the purpose of clarity. Note the light curve from `K2SFF` as well as `Everest` are not flattened, and show variation related to star spots modulation.

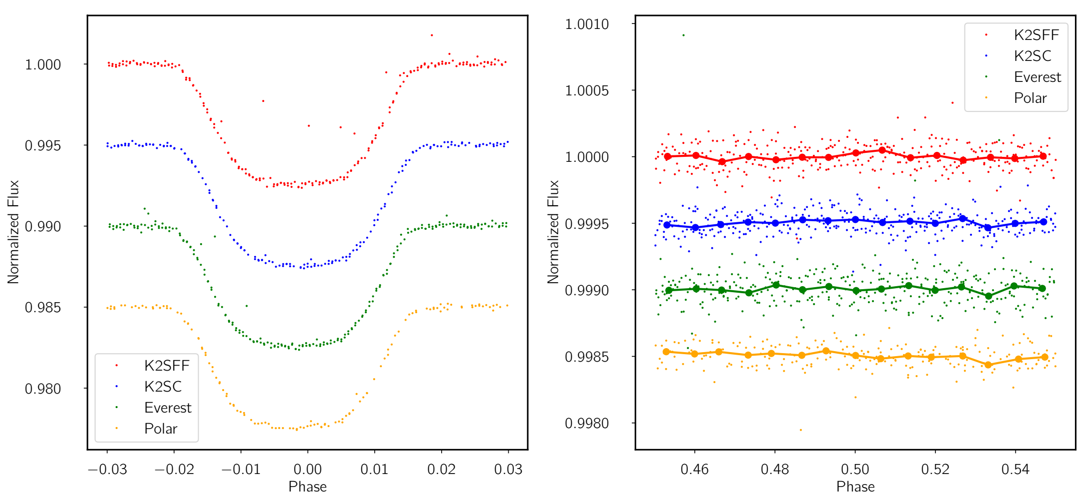

Figure 2.4: Transit of K2-34 obtained from using different detrending algorithm. All of the light curves fail to show a statistically significant secondary eclipse.

2.2 Reduction Pipeline

There is a strong correlation between the position of the centroid of the star with the locally normalized flux as shown in Figure 2.5. The local normalized flux is found by spline fitting the raw light curve by iteratively rejecting the outliers. This models the stellar continuum flux, and can be used to normalize the flux. The centroid of the star is calculated from the weighted mean of the flux for the entire time series. A more robust, but computationally expensive method, would be to fit a Gaussian function to the PSF. However, my attempt to use 2D Gaussian function against a flux weighted centroid finding algorithm produced a light curve of similar quality, hence the latter algorithm has been used primarily because of its simplicity and lower associated computational cost. In order to estimate the background value, I use the median value in the aperture, and fit the spline over time to avoid any outliers. The flux in the selected aperture is summed up, and the background is subtracted.

Once these photometric time series are obtained, then the values are decorrelated against the stellar centroid drift using `K2Phot` or `K2SFF`. In `K2SFF` the relationship between the arclength (the distance the centroid of the star moves) and normalized flux is fitted using a fifth order polynomial for data chunks of every 3 days. After such a relation is found, the flux variation due to positional shift is detrended as shown in Figure 2.5. Since this is a re-iterative process, there is room for outliers which for instance can be data taken during the thruster fire events or transit events. The *K2* pipeline already marks the different outliers in the data from the data pre-conditioning *K2* pipeline. A strict criterion would be to use only data whose Quality Flag are equal to 0. However, it is also possible to impose a laxer requirement by allowing flags such as 32768 which is raised when the “Spacecraft is not in fine point” (Van Cleve et al. 2016) in case the data is too sparse or the pipeline marks too many data points as outliers.

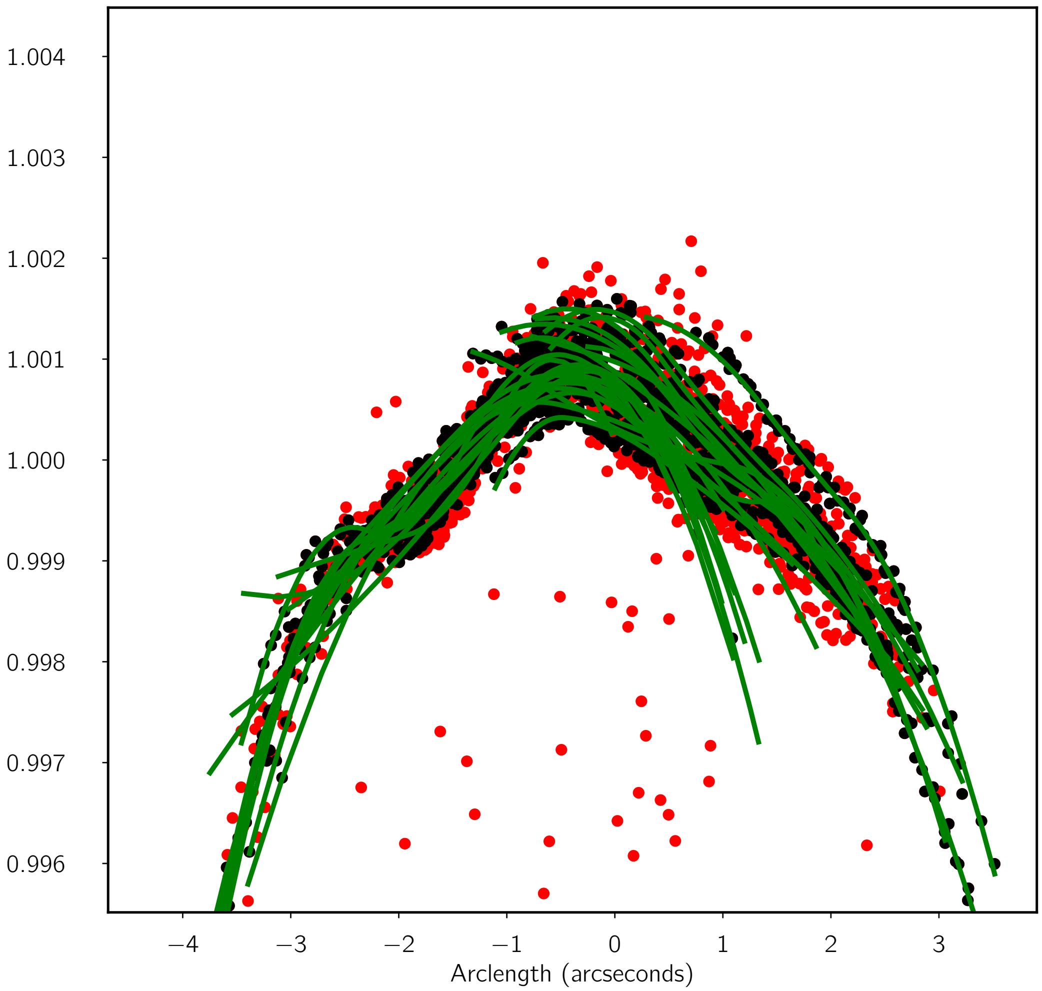

Figure 2.5: Self Flat Fielding (SFF) showing the relation between the position and the flux. The red points, excluded in the fit, are potentially related to thruster firing event or the transit. These points are rejected by performing a re-iterative process fitting a fifth degree polynomial. The red points are the outliers that were not used in fitting the polynomial, and every green line is the polynomial fit for a chunk of the data.

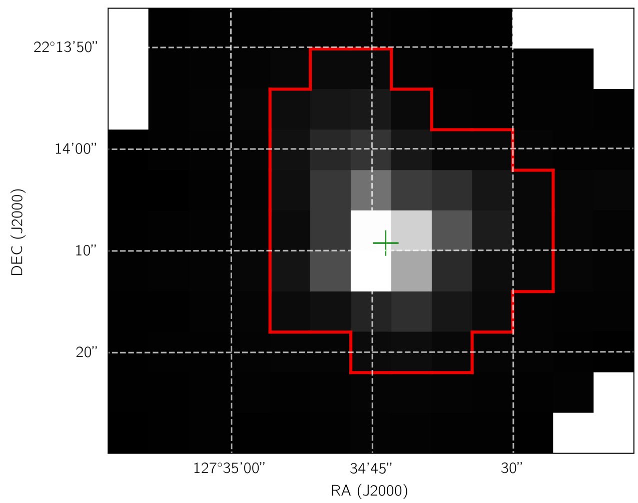

Figure 2.6: The aperture selected for K2-34 from the median stacked image is shown with an red outline.

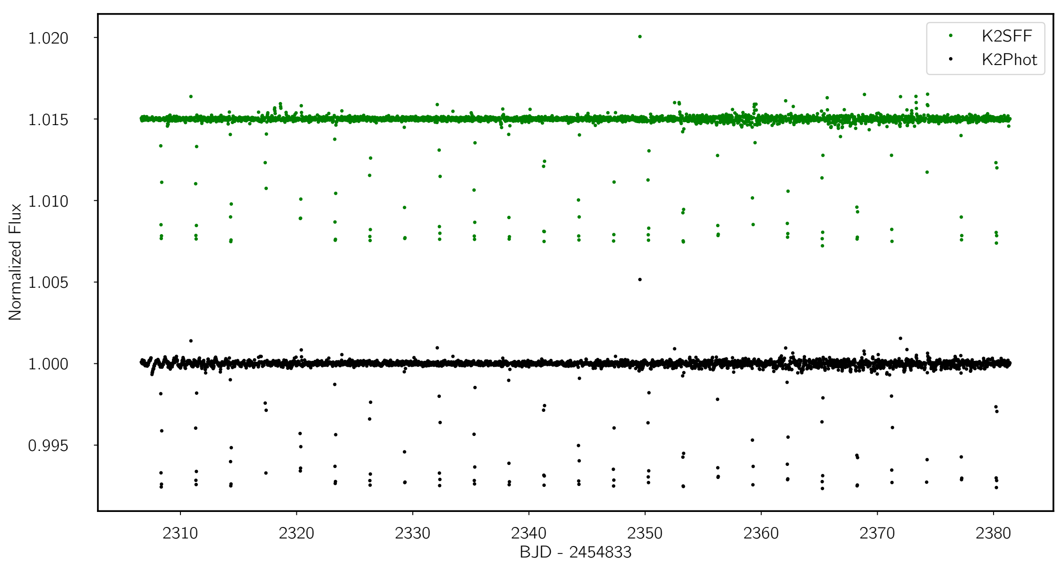

Figure 2.7: Detrended and flattened light curve from our pipeline, which is of comparable quality compared to light curve from other pipelines as shown in Figure 2.4.

2.2.1 Aperture

Unlike the original *Kepler* mission, *K2* is complicated by the drifting of the field. Thus, the PSF has to be constructed on a frame to frame basis, which is computationally expensive. Often a simple aperture photometry (SAP), method of summing up all the fluxes in an aperture without weights, is good enough for most of the targets. There is no universal way of building an aperture, and this is often left for trial and error using a combination of different algorithms. For instance, a simple way to construct the aperture is to use the median pixel factor from the average stacked image. However, crowding and blending make this complicated, and such a field would require more specialized treatment. Since individual pixels are 4 arcseconds, blending and source confusion pose a worse problem for *Kepler* than telescopes with higher spatial resolution. For crowded fields, I use the watershed algorithm implemented in `scikit` library[2] to find the right boundary as shown in Figure 2.9. This algorithm will be described in greater detail in subsubsection 2.3.

For K2-34, the selected aperture selected is shown in Figure 2.6. In order to obtain the aperture, the time series is collapsed to form a median stacked image. From this image, the suitable aperture is found by constructing the largest contiguous region that has a flux value larger than 2 times the median value in the median stacked image. This threshold for defining aperture is arbitrary, but often good enough as pointed out in Van Eylen et al. (2016). Due to the drifting of stars in the field, it is difficult to find which set of pixels make the best combination for the aperture. The process of choosing the aperture is left to trial and error in order to produce the best photometric data. However, once a target is found to be interesting due to potential presence of planetary signal, different combinations of apertures can be used to produce an optimal light curve. A common way of finding the best aperture is to use an increasing aperture radius from the known or the calculated location of the star, and choose the best light curve obtained

[2]http://scikit-learn.org/stable/

among the different produced light curves. This method was employed for GJ 9827 or EPIC 246389858, which will be discussed in Chapter 3.

2.2.2 Flattening

Before looking for the planetary signal, it is necessary to flatten or normalize the light curve. Flattening in the `pyke`[3] library, the official pipeline for *Kepler*, is carried out using a Savitsky-Golay filtering technique. This process uses a sliding filter which leaves the short term features such as transit or flares unchanged, while fitting out the longer term trends such as stellar modulation. For our pipeline, we use an iterative spline fitting in order to fit for the time series. We also use a local variance based flattening technique to deal with discontinuities in the light curve. Flattening can also introduce an unintended signal into the light curve when looking for smaller signals such as phase curves, and particularly difficult for light curves with long period planets. This is a point which will be revisited in greater detail in Chapter 4. But for a typical transit, the flattening process is relatively straightforward and does not interfere with the transit signal.

2.2.3 Bright Targets

White et al. (2017) has particularly focused on the getting precise photometry of bright stars through a process referred to as halo photometry. They were able to substantially improve the photometry for bright stars, compared to more conventional techniques described above. The method involves rejecting the columns suffering from column bleeding, and assigning weights to each pixel with halo emission based on their variability. For seven Pleiades stars, White et al. (2017)

[3]https://github.com/KeplerGO/pyke

reported obtaining a light curve better by a factor or 2–3 compared to traditional methods. As most of our targets do not need such special care, I have not implemented this algorithm. But this will be a line of research that will be pursued by our research group in the future.

2.3 Planetary Signal Search

A search for planetary transit signals is often conducted on a processed and flattened light curve. In this process of preparing the light curve, the effects such as flares or cosmic rays can be simply removed by ignoring the positive outliers that significantly deviate from the median value. On this flattened light curve, there are multiple methods available for conducting a planetary search. Among them, box least squared (henceforth `BLS`) proposed by Kovács et al. (2002) remains one of the most successful methods in searching the planetary signal. The `BLS` algorithm can be modified for a trapezoidal signal search as a trapezoid is a better representation for a transiting signal compared to a rectangle. This is particularly important when looking for shallower planetary signals or shorter transiting signals. However, for our search we have been using `BLS` implemented in `python` by Daniel Foreman Mackey[4]. Recently, a different method known as notch filter has been shown to work for relatively shallower transit (Rizzuto et al. 2017), which works even on an unflattened light curve. However, by tuning the level of the threshold, and the process for flattening in our search we can arbitrarily tease out weaker transit signals. Besides, we can always find the transiting signals by visually inspecting them later, thus an arbitrary SNR value above 3 can be assigned for the detection threshold, and all of such threshold crossing events were

[4]https://github.com/dfm/python-bls

manually checked. For K2-34b, the `BLS` algorithm is easily able to find the period with high precision as shown in Figure 2.8. Harmonics of the signal can also be seen in the periodogram at the integer multiples of the true period.

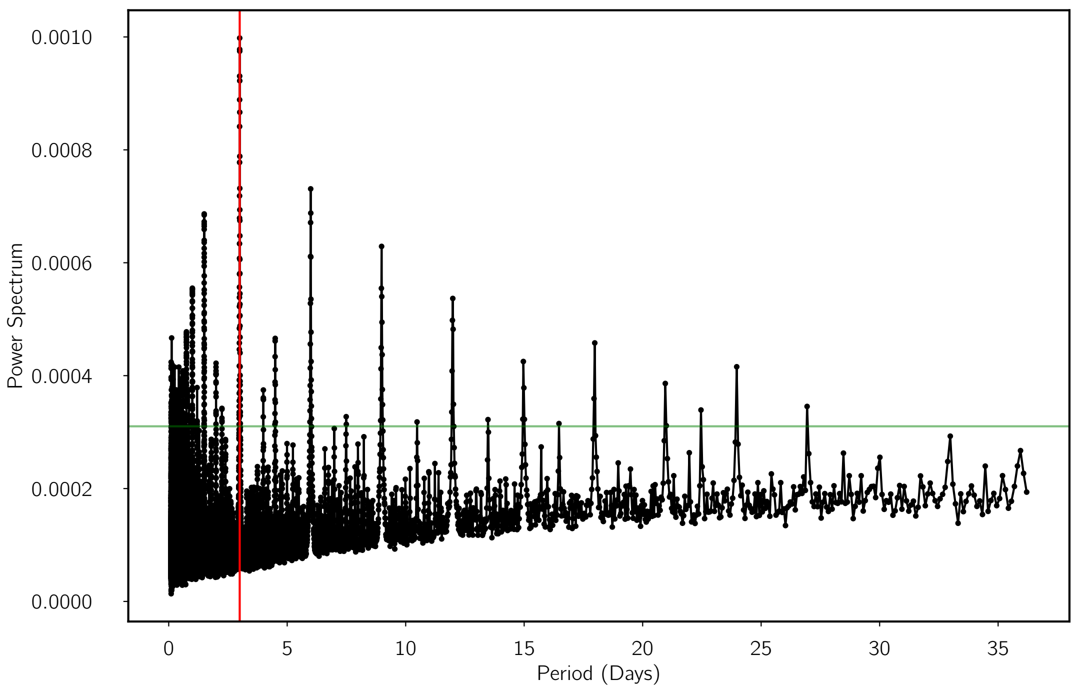

Figure 2.8: Figure depicting the power spectrum `BLS` periodogram for K3-34. A significant peak is observed at period of 2.995622 days, which is marked by red line. The green line marks the 4 times the median value of power, which is often used as the detection threshold value for follow-up evaluation.

Long Period Planets

It has been common practice in the exoplanet community to only consider transits with at least three occurrences. For an 80 days observation, a typical observational run length for *K2* campaigns, the largest possible planetary period fulfilling this criteria is 40 days. However, it is indeed possible to find plan-

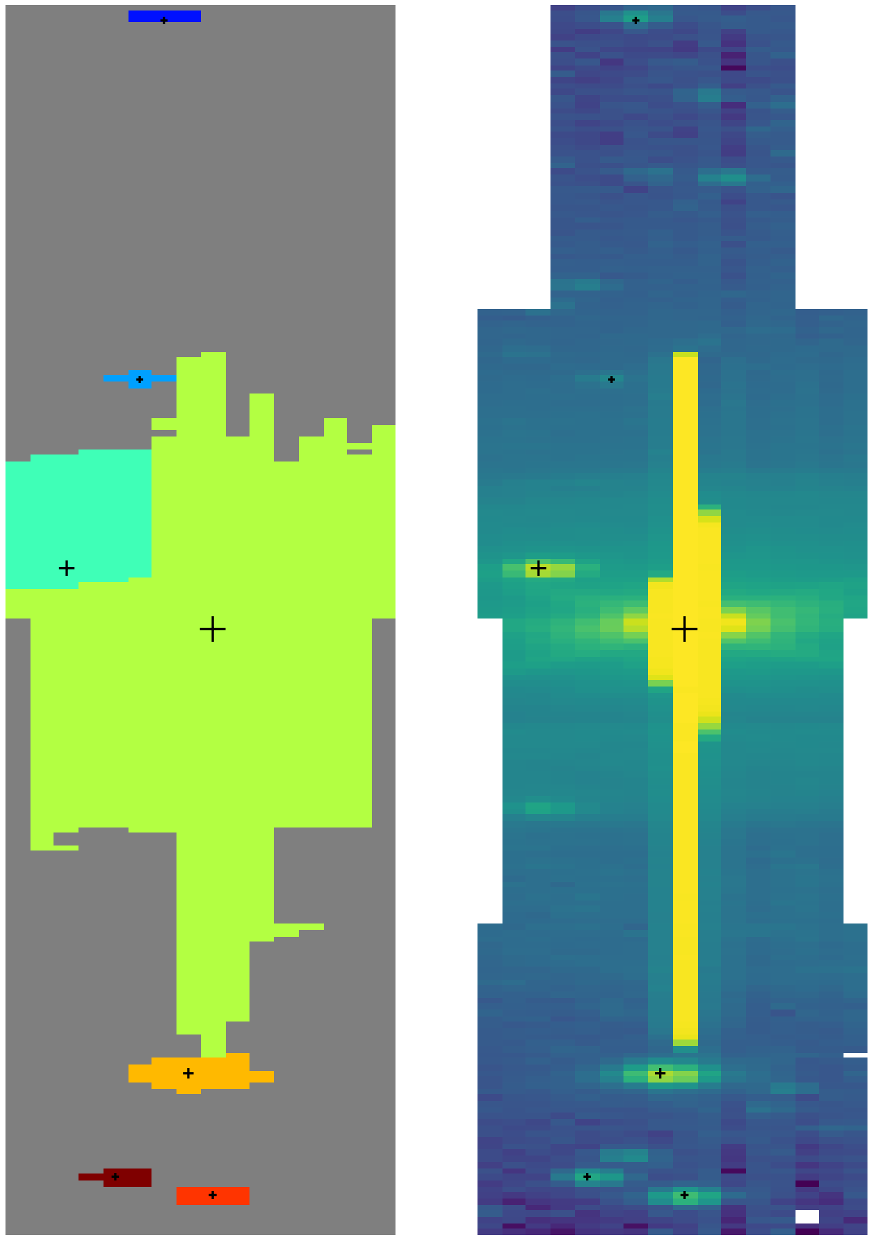

Figure 2.9: Multiple stars captured during the observation of a bright star (EPIC 212110888) from Campaign 5 by *K2* . The black cross hairs mark the location of different stars. The image on the left show the apertures selected for each star, and the image on the right shows median stacked image of the field. The aspect ratio has been altered to make the stars easier to spot.

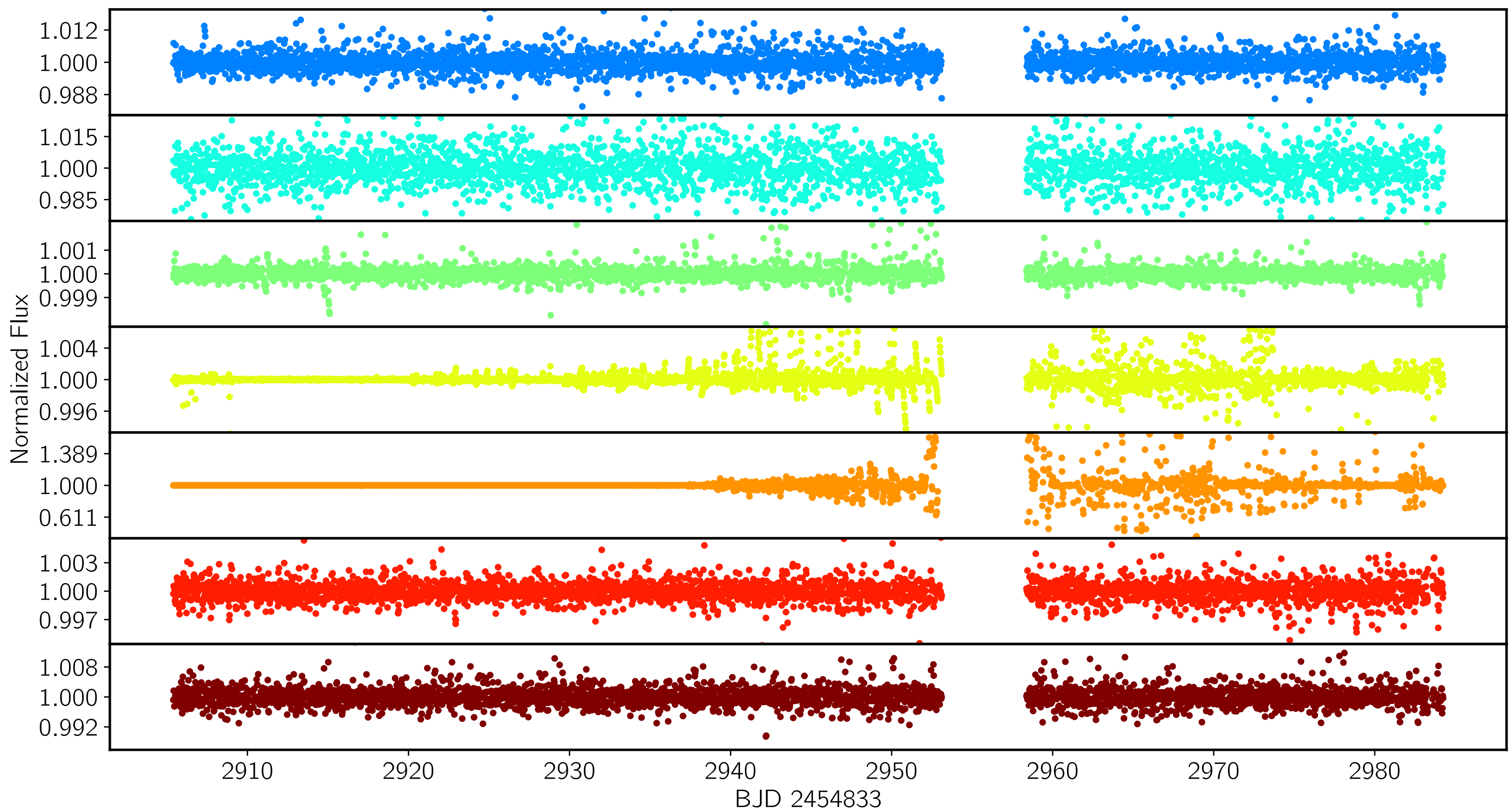

Figure 2.10: Flattened light curve from multiple stars captured serendipitously in frame of EPIC 212110888 during Campaign 5. The same color is adopted as in Figure 2.9 for the flattened light curve. For the orange aperture, which is close to the bright stars, imperfect aperture boundaries will have the greatest effect due to its closeness to the bleeding column, as is also evident in the above light curve.

ets with orbital periods longer than 40 days. If multiple planets are detected, such multiplicity can be helpful in verifying the nature of such transits, as multiplicity drastically reduces the false probability rate of the exoplanet (Lissauer et al. 2012). In such cases the transit duration as discussed in Equation 1.2 can be used to roughly constrain the orbital parameters, as well as the period. Since the probability of transit falls dramatically for the longer transit as with $P^{-\frac{5}{3}}$ (Foreman-Mackey et al. 2016), long period planets are always difficult to find. The long term planetary signals are also difficult to vet using RV, as shown in Equation 1.4 although would be easier with astrometry. Besides, the transit ephemerides of such systems often cannot be pinpointed with enough precision for follow-up observations. Despite all these challenges, there has been growing number of interest in longer period planets (Foreman-Mackey et al. 2016; Bryan et al. 2016) particularly because presence of such planets have major implications on the migrations, architecture, as well as occurrence rates.

Serendipitous targets

Often due to crowding, a star at the periphery can be serendipitously captured in the field of the view. This is more often the case in *K2*, which observes bright targets with larger apertures, as shown in Figure 2.9. For our pipeline, we automatically look for the stars in the field and perform the detrending and planetary search algorithm for all of these targets. So far, no signal of planetary origin has yet been found among these types of targets. However, since these targets occur near the brighter targets, they may be particularly hard to follow-up and validate. Thus, not a lot of effort seem to have been put onto these type of targets. As many of the serendipitous targets occur in a crowded area, for drawing apertures I use watershed algorithm implemented in `scikit` library[5] inspired by the efforts of Lund et al. (2015). This algorithm is particularly adapted for finding the borders between two different objects when the boundary are slightly overlapping.

2.4 Vetting process

Many astrophysical signal can masquerade as the planetary transit signal, hence once a potential transit signal is found, it must be thoroughly vetted. Originally, the community required using complementary methods such as RV follow-up. However, this requirement was considered too high as it is not possible for most of the *Kepler* stars due to the faintness of the targets. In fact, there are still thousands targets that are roaming in the purgatory of KOIs (*Kepler* Object of Interest) because there are no methods available for further validation.

The most common source of such false positive comes from background binaries, and the comparatively low spatial resolution of *Kepler* only serves to make the situation worse. In order to vet any systems found using *Kepler* and *K2*, Morton et al. (2016) developed a code called `vespa`, which attempts to statistically verify the fidelity of planetary signal. However, it has been found that `vespa` alone is not sufficient, and additional vetting analyses, such as aperture contamination and PSF analysis is required (Cabrera et al. 2017). `Vespa` operates by calculating the possibility that the light curve can be obtained by different conditions such as an unblended eclipsing binary, hierarchical-triple eclipsing binary, chance-aligned background/foreground eclipsing binary, and a transiting planet. Also, as mentioned earlier it is also possible to verify the validity of the signal using phase curves through the amplitude of the ellipsoidal variation (Mislis &

[5] http://scikit-image.org/docs/dev/auto_examples/segmentation/plot_watershed.html

Hodgkin 2012), or through dynamics such as transit timing variations (Agol & Fabrycky 2017). But there are only a handful systems that can be verified in this fashion leaving many with no viable methods for validation.

Detrending algorithms with *K2* are getting better with time, and the planet recovery rate are getting higher. It would be interesting to see how *K2* compares with *Kepler*. Understanding how different detrending algorithm fares, and what are the good setup for the knobs for each algorithm is something we will learn with time, and this can be seen as better quality of light curves are being extracted for later campaigns compared to earlier. The data challenges with *K2* has helped in creating a host of new tools and techniques, whose utility is not likely to be limited to astronomy.

Chapter 3

GJ 9827

GJ 9827 (also EPIC 246389858 and K2-135) was observed by *K2* for a total of 78.89 days from 15 December, 2016 to 4 March, 2017 at the boundary of the constellations Aquarius and Pisces at RA of 23:27:04.835 and declination −01:17:10.58 in long cadence mode. It was purposed as a part of nearby star survey by PI Redfield (GO-12039); and additionally proposed in three other programs: GO-12071, PI Charbonneau; GO-12049 PI Quintana; and GO-12123 PI Stello.

Nearby stars, particularly within 100 parsecs, are inherently interesting targets. Temporal monitoring of neighboring stars such as GJ 9827 provides an opportunity to search for nearby planetary systems that are optimal for follow-up studies. These targets tend to be brighter due to their distance, which in turn allows detailed follow-up analysis for planetary atmosphere and habitability, such as the stellar UV emission (Linsky et al. 2014), stellar wind strength (Wood et al. 2005) and stellar magnetic field structure (Alvarado-Gómez et al. 2016).

In our analysis of the light curves of GJ 9827, we detected transits from the three planets (Niraula et al. 2017). At 30.3 ± 1.6 parsecs, it is the nearest planetary system detected by *Kepler* or *K2*. Our analysis of the *Kepler* light curve identifies the presence of three super-Earth planets of radii around GJ 9827. We used the designation of super-Earth for planets with radii from 1.25–2 $R_\oplus$ (e.g., Batalha et al. 2013), even though the density obtained by later RV campaign revealed GJ 9827 d is likely a mini-Neptune. The planets orbit at a distance of 0.020 ± 0.002, 0.041 ± 0.003 and $0.059\ ^{+0.004}_{-0.005}$ AU corresponding to orbital periods of $1.208957^{+0.000012}_{-0.000013}$, 3.64802 ± 0.00011, and $6.20141^{+0.00012}_{-0.00010}$ days respectively. The planetary system is tightly packed, and the periods are close to 1:3:5 commensurability. In addition to the fact that GJ 9827 is a relatively bright star, the planets occur on both sides of the rocky and gaseous threshold of $\sim$1.5 $R_\oplus$ (Weiss & Marcy 2014; Rogers 2015). Hence the system is likely to be a great asset in understanding the nature of this threshold. Also note that there were two simultaneous discovery papers on GJ 9827 (Niraula et al. 2017; Rodriguez et al. 2018).

The GJ 9827 planets are great candidates for atmospheric studies. In the past, ground based telescopes, along with the *Hubble Space Telescope* (*HST*) and *Spitzer*, have been successfully used to characterize the atmospheres of hot Jupiters (Charbonneau et al. 2002; Knutson et al. 2008; Redfield et al. 2008; Sing et al. 2015). With the *James Webb Space Telescope* (*JWST*), this territory will be extended into the super-Earth regime (Deming et al. 2009). Bright, nearby planetary systems like GJ 9827, will provide excellent opportunities to probe the atmospheres of super-Earth planets.

3.1 Stellar Parameters

Finding the size of the planets through transits requires estimating the actual size of the star. In order to derive the stellar parameters, the co-added FIES (Fibre-fed Echelle Spectrograph) spectrum was used. The spectrum has a SNR ratio of $\sim$150 per pixel at 5500 Å. The analysis was performed by the experts in KESPRINT following the procedures already that was used in other *K2* related work (Fridlund et al. 2017; Gandolfi et al. 2017). Our parameters were obtained by using `SpecMatch-Emp` (Yee et al. 2017). This technique is established by looking at the empirical data which takes into account effective temperature ($T_{\rm eff}$), radius ($R_\star$), and iron abundance ([Fe/H]), all of which has been accurately measured by interferometry, spectrophotometry, and spectral synthesis. Our team used empirical relations from Mann et al. (2015) to derive the stellar mass. Our stellar parameters are presented in Table 3.1. The values are consistent with those reported by Houdebine et al. (2016), where stellar parameters for 612 late-K and M dwarfs were derived.

Table 3.1: Stellar Parameters of GJ 9827

V mag	-	10.39[a]
J mag	-	7.984[b]
Distance	pc	30.3 ± 1.6[c]
Spectral Type	-	K6V[d]
Effective Temperature ($T_{\rm eff}$)	K	4255 ± 110[d]
Surface gravity ($\log g$)	cgs	4.70 ± 0.15 [d]
Iron Abundance ([Fe/H])	dex	-0.28±0.12[d]
Radius (R_*)	$R_\odot$	0.651 ± 0.065[d]
Mass (M_*)	$M_\odot$	0.659 ± 0.060[d]
$v \sin i$	km s^{-1}	2 ± 1[d]

[a] Adopted from Zacharias et al. (2013)
[b] Adopted from Cutri et al. (2003)
[c] *Hipparcos* from (van Leeuwen 2007)
[d] Adopted from Niraula et al. (2017)

3.2 Data Reduction

As discussed in Chapter 2, we implement a data reduction pipeline to detrend the systematic *K2* noise. We follow the protocol to decorrelate the data against its arclength (1D) using one of the three standard stars from the Campaign (e.g., Vanderburg & Johnson 2014; Vanderburg et al. 2016). These standard pointing stars are chosen such that their centroid can be found with better precision than an average star in the field. Among these three standards, the light curve is decorrelated with the star whose centroid variation over time is best fit with a fifth-degree polynomial, in this case EPIC 246292491. Besides, we use a modified version of Van Eylen et al. (2016) publicly available code,[1] which detrends the light curve by a simultaneous second order fit for both the centroid coordinates and time, also allowing for a cross term between two centroids. The `k2photometry` (also referred at `k2phot`) pipeline yields a flattened light curve. In our implementation, the final transit removed light curve from `k2photometry` has a standard deviation of 77 ppm compared to 106 ppm from Vanderburg's method. Thus in Figure 3.2, we show the detrended flux obtained from Vanderburg's method and the normalized light curve from `k2photometry`. These values are higher by a factor of $\sim$2 than the expected calculated rms values of 39.2 for a V = 10.5 magnitude star,[2] which is likely a result of pointing induced errors for *K2*.

As for some of the unique aspects of our pipeline, we take the median value in each frame as the background. In order to avoid the effect of the outliers, we perform an iterative spline fitting, rejecting 3σ outliers until convergence. Finally, the background is subtracted from the photometric flux. We reject the data with bad quality flags, which resulted in excluding around 15% of the data flagged for thruster firing, Agrabrightening (a sudden brightening event lasting for a couple of minutes), cosmic ray detection, and pipeline outlier detection. This has led to two instances where the transits are completely missing (refer to Figure 3.2). We did a follow-up test with different aperture sizes from which a circular aperture of $\sim 20''$ radius is chosen as shown in Figure 3.1. Initially we define our aperture

[1] https://github.com/vincentvaneylen/k2photometry
[2] https://keplergo.arc.nasa.gov/CalibrationSN.shtml

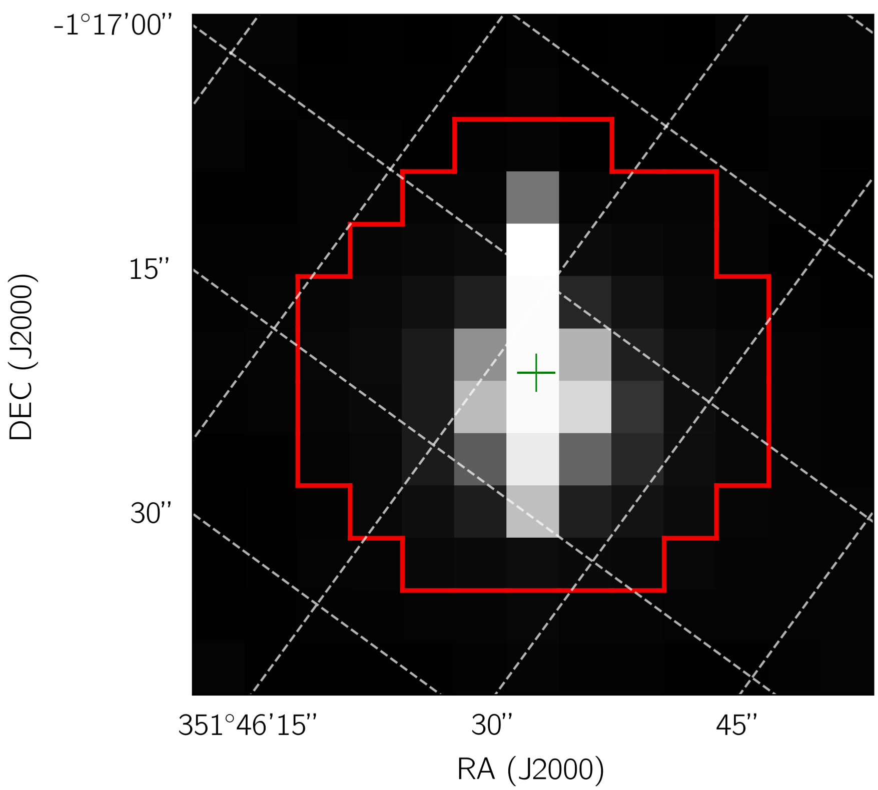

Figure 3.1: Aperture selected for K2 flux extraction and detrending for GJ 9827. Different apertures were used for flux extraction.

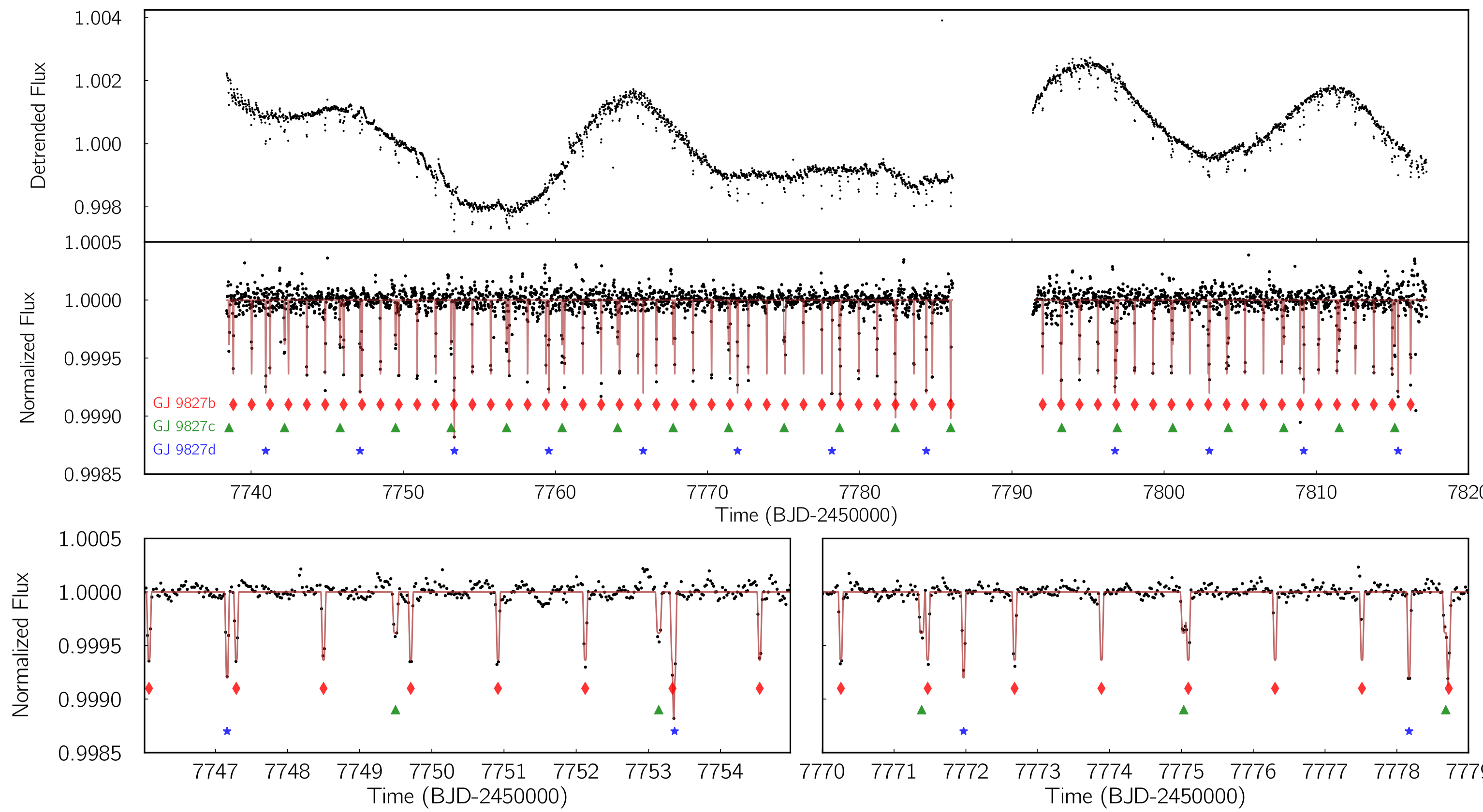

Figure 3.2: Detrended and normalized K2 light curve of EPIC 246389858. Transits of each planet are marked, and the combined fit (brown line) at a finer sampling rate for all transit based on MCMC fits, presented in Table 3.2, is shown. The bottom left and bottom right figure zooms into two different sections of the data.

as the largest contiguous region above twice the median. From this we calculate the centroid of the star. However, the calculated centroid of the star does not coincide with the FITS coordinates probably because GJ 9827 is a high proper motion star (Stephenson 1986).

3.3 Light Curve

Clear stellar modulation, associated with stellar rotation, is evident in the detrended light curve of Figure 3.2. After we remove the first five days of data which shows anomalies probably related to thermal settling, the auto correlation function (ACF) (McQuillan et al. 2013) of the detrended light curve exhibits a peak at $16.9^{+2.14}_{-1.51}$ days, which is consistent with our reported $v \sin i$ value of 2 ± 1 km s^{-1} assuming a stellar inclination of 90°. A Lomb-Scargle periodogram also shows a stronger peak at around the same region as ACF as shown in Figure 3.3. However, we also note an almost comparable secondary peak at 29 days, which is congruous with the value of $1.3^{+1.5}_{-1.3}$ km s^{-1} reported in Houdebine et al. (2016). But given the precision, the real period cannot be uncontestably established. A longer baseline of observations would help to determine the true stellar rotation period. Note it has been established in the field that the auto-correlation function provides a better estimation of the stellar rotation in comparison to other methods such as a Lomb-Scargle periodogram, which as shown in the figure, and has a peak at around 24 days. This debate can be settled with the longitudinal magnetic field data from Zeeman Doppler Imaging monitoring of GJ 9827 (e.g. Hébrard et al. 2016).

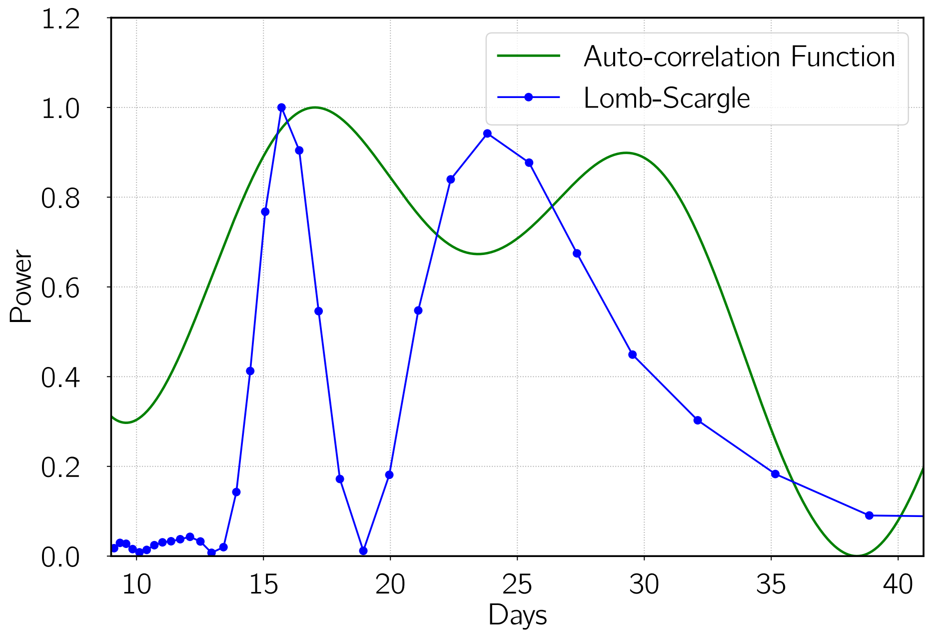

Figure 3.3: Periodograms from auto-correlation function (ACF) method and Lomb-Scargle method. ACF has the primary peak around $16.9^{+2.14}_{-1.51}$ days and the secondary peak around $29.5^{+2.1}_{-2.7}$ days , while Lomb Scargle shows the primary peak at $15.9^{+1.1}_{-1.2}$ daysand a secondary peak at $23.8^{+4.5}_{-2.6}$ days. Maxima of both methods has been normalized to 1.

3.4 Transit Fitting

We perform a Box Least-Squared (BLS; Kovács et al. 2002) search on the flattened light curve to detect the presence of any planetary signals. Once a transit signal is identified, it is fitted and removed from the light curve. In this fashion, we iteratively run the BLS algorithm on the light curve for further detection of additional transit signals. In GJ 9827, this showed a presence of three transiting planets. A simultaneous fit for all of the three identified transits is then performed with the `batman` model supersampled by a factor of 15, and adjusted for *K2*'s long cadence (Kreidberg 2015), which is shown in Figure 3.2. We use the affine invariant MCMC method implemented in `emcee` (Foreman-Mackey et al. 2013) with 100 walkers for 30000 steps; of this, the first 22500 steps were removed as burn-in. The rest of the data is used to build the posterior distributions and estimate the uncertainties in our transit parameters.

We use uniform priors for the period, time of conjunction, scaled planet radius and impact parameter for all three planets. For limb darkening parameters, we use triangular sampling suggested by Kipping (2013). We additionally use Sing (2010) to introduce Gaussian priors on limb darkening based on the stellar parameters. We use the mean value of 0.5782 for u_1, and 0.1428 for u_2, both with 0.1 standard deviation. Since this is a short period multi-planetary system, we assume tidal circularization of the orbits and adopt a fixed eccentricity of $e = 0$ for all three planets (Van Eylen & Albrecht 2015). As for the scaled semi-major axis of GJ 9827 c and d, we assume they are constrained by Kepler's Third Law. As a result, we fit 15 independent variables (Table 3.2). We additionally introduce a Gaussian prior based on the spectroscopically derived stellar density of 3.37 ± 0.51 g cm^{-3}. MCMC runs without Gaussian priors sometimes converged to unrealistic semi-major axis values. From the posterior distribution, most of the variables are well constrained except for limb darkening parameters. Due to short transit duration and long integration time for *K2*, limb darkening parameters are not expected to be well constrained (Kipping 2010). The introduction of Gaussian prior for limb darkening parameters does not noticeably affect the other fit parameters. The corner plot showing posterior distribution from a different run is shown in Figure 3.4, both of which converges to similar set of values.

It is interesting to note that the transit duration, as can be visually estimated from Figure 3.5, is longest for GJ 9827 c, and shortest for GJ 9827 d. This is consistent with the fit's prediction that GJ 9827 d has a higher impact parameter than either GJ 9827 b or c . Additional independent MCMC runs were performed by our team using `pyaneti` (Barragán et al. 2017a), with flattened light curves from independent pipelines developed in our group, and the results are within 1σ errors. Note that the high impact parameter of GJ 9827 d suggests additional planets, if present, are likely to be non-transiting. This possibility has been explored in the follow-up RV campaign (see Section 3.7), however given the low amplitude of the RV signals it has not been possible to identify additional planets.

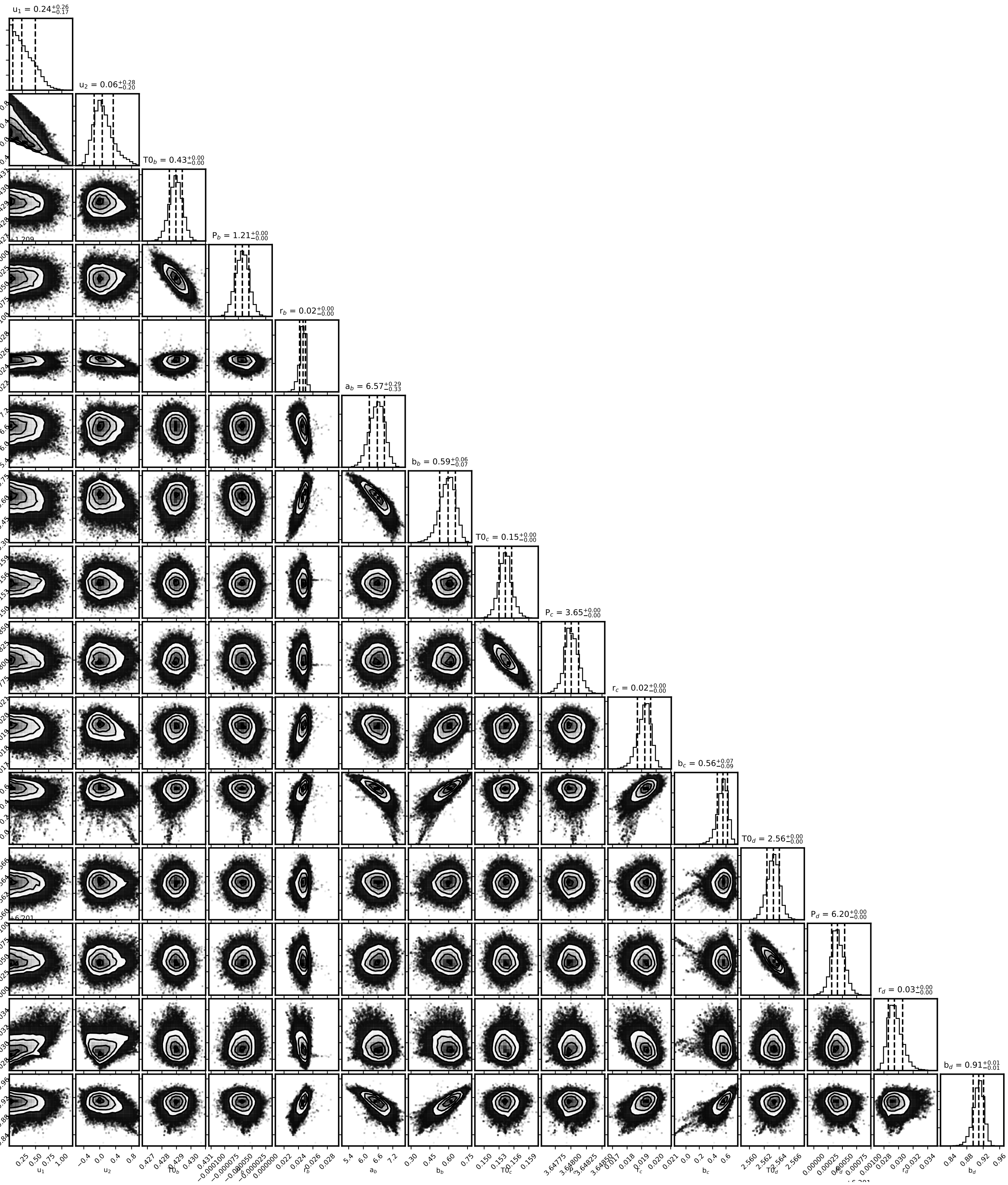

Figure 3.4: Corner plot for 15 different parameters obtained by MCMC run for fitting the transits and all of which are listed in Table 3.2. The contours represent 1σ, 2σ and 3σ values for the parameters in the posterior distribution, and the title at top of each subplot shows 1σ interval.

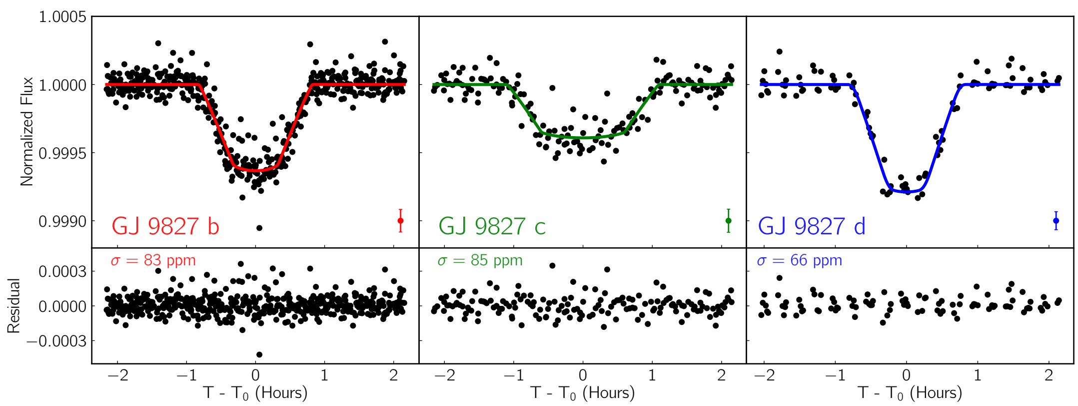

Figure 3.5: Model Fit of MCMC obtained parameters for GJ 9827 b, GJ 9827 c, and GJ 9827 d. The parameters are available in Table 3.2. Note the normalized flux scale is kept constant for comparison. 1σ error bars computed from the respective residuals are shown in the right hand bottom corner for reference. The obtained fit parameters are reported in Table 3.2.

Table 3.2: Planetary Parameters of GJ 9827 b, c, and d obtained by fitting transits as shown in Figure 3.5

Parameter	Unit	GJ 9827b	GJ 9827 c	GJ 9827 d
Transit Epoch BJD–2450000 (T_0)	day	$7738.82671^{+0.00043}_{-0.00046}$	$7738.5519^{+0.0014}_{-0.0014}$	$7740.96100^{+0.00083}_{-0.00087}$
Period (P_{orb})	day	$1.208957^{+0.000012}_{-0.000013}$	$3.64802^{+0.00011}_{-0.00011}$	$6.20141^{+0.00012}_{-0.00010}$
Scaled planet radius (R_p/R_*)	-	$0.0246^{+0.0003}_{-0.0005}$	$0.0192^{+0.0004}_{-0.0005}$	$0.0297^{+0.0010}_{-0.0008}$
Scaled Semimajor axis (a/R_*)	-	$6.55^{+0.30}_{-0.32}$	$13.67^{+0.66}_{-0.63}$	$19.5^{+0.95}_{-0.90}$
Impact Parameter (b)	-	$0.595^{+0.056}_{-0.070}$	$0.558^{+0.068}_{-0.096}$	$0.910^{+0.011}_{-0.013}$
Derived Parameters				
Planet Radius (R_p)	$R_{\oplus}$	$1.75^{+0.18}_{-0.18}$	$1.36^{+0.14}_{-0.14}$	$2.11^{+0.22}_{-0.21}$
Semi Major Axis (a)	AU	$0.020^{+0.002}_{-0.002}$	$0.041^{+0.003}_{-0.003}$	$0.059^{+0.004}_{-0.005}$
Transit Duration (T_{14})	hour	$1.12^{+0.06}_{-0.07}$	$1.69^{-0.11}_{+0.10}$	$1.01^{+0.05}_{-0.05}$
Orbital Inclination (i)	deg	$84.86^{+0.54}_{-0.54}$	$87.66^{+0.30}_{-0.31}$	$87.32^{+0.12}_{-0.13}$
Equilibrium Temperature (T_{eq})	K	1075^{+38a}_{-37}	744^{+26a}_{-26}	623^{-22a}_{-22}

3.5 Validation

Lissauer et al. (2012) showed that the false positive probability for multi-planetary system is less than 1%. However, further efforts were taken in validating the signal. It is standard practice in the field to use `vespa` to validate the detection using statistical method. Rodriguez et al. (2018) used this method and derived giving false positive probability under 1 in 10^{-5} for all three planets. As mentioned earlier, `vespa` considers different population distribution of eclipsing binaries, and calculates the false probability rate for them to masquerade as the planetary transit (Morton et al. 2016).

Given its large proper motion (≈ 400 mas yr^{-1}), we are able to rule out the possibility of an unbound background contamination using archival data. Using the STScI Digitized Sky Survey,[3] we identify GJ 9827 images as early as 1953 (see Figure 3.7). By comparing the image to the latest epoch (2012), we determine that there is no background object coincident with its K2 aperture visible in the 1953 plate. In order to estimate the limiting magnitude of the 1953 image, we considered an object near to our target which is faint, but clearly above the detection threshold of the image. By reference to the SDSS catalog, we determined that this object has $r = 19.0$ (cf. $r = 10.1$ for GJ 9827). We, therefore, conclude that the 1953 plate is sensitive to objects about 9 magnitudes fainter than GJ 9827, and we can rule out the presence of unbound contaminants brighter than this. An equal mass eclipsing binary system with a combined magnitude of $r = 19.0$ would produce at most a 125 ppm deep signal in the light curve of GJ 9827, which is shallower than the observed transits.

Additionally, high contrast images were taken in order to look for near com-

[3]http://stdatu.stsci.edu/cgi-bin/dss_form

panions by KESPRINT (see Figure 3.6), and also by previous surveys (Jódar et al. 2013), which showed absence of any companion stars. Besides, the fitting of the spectral energy distribution did not show the presence of any infrared excess. In addition, an RV campaign covering a couple of weeks showed no strong variation due to stellar companions as was reported in Niraula et al. (2017).

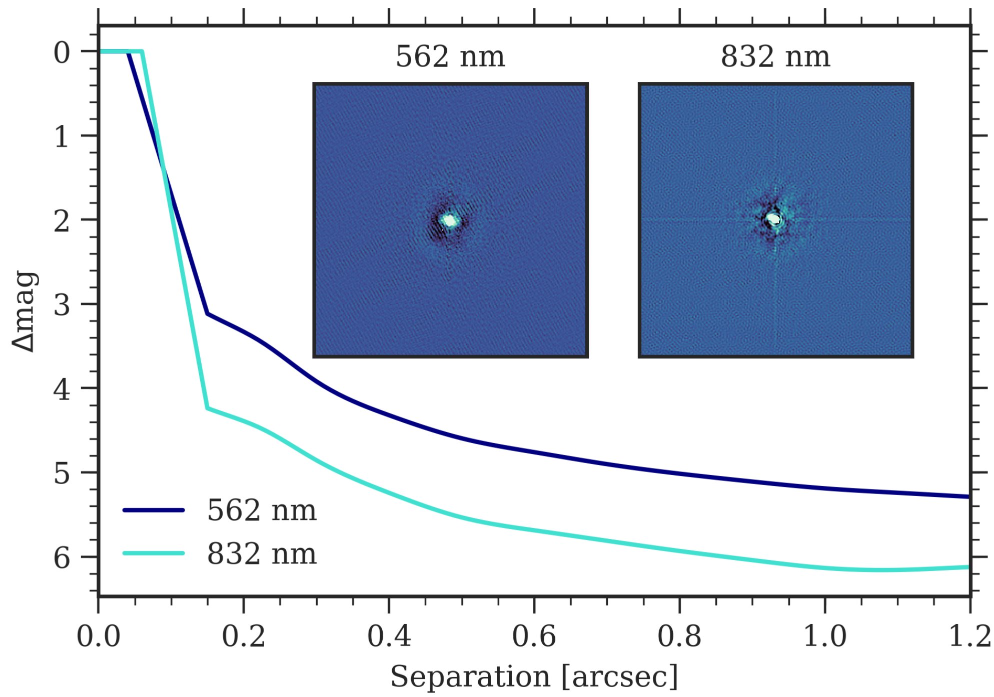

Figure 3.6: Speckle image taken at 562 nm and 832 nm taken with WIYN/NESSI speckle interferometry which shows an absence of companion. Adopted from Prieto-Arranz et al. (2018).

3.6 Transit Timing Variation

No TTV greater than 3 minutes were found for the planets GJ 9827 b, c, and d as shown in Figure 3.8. An order of magnitude calculation of the expected TTV amplitude, based on work by Agol et al. (2005), indicates that the expected amplitude of TTVs is smaller than 3 minutes. Occurring near commensurability

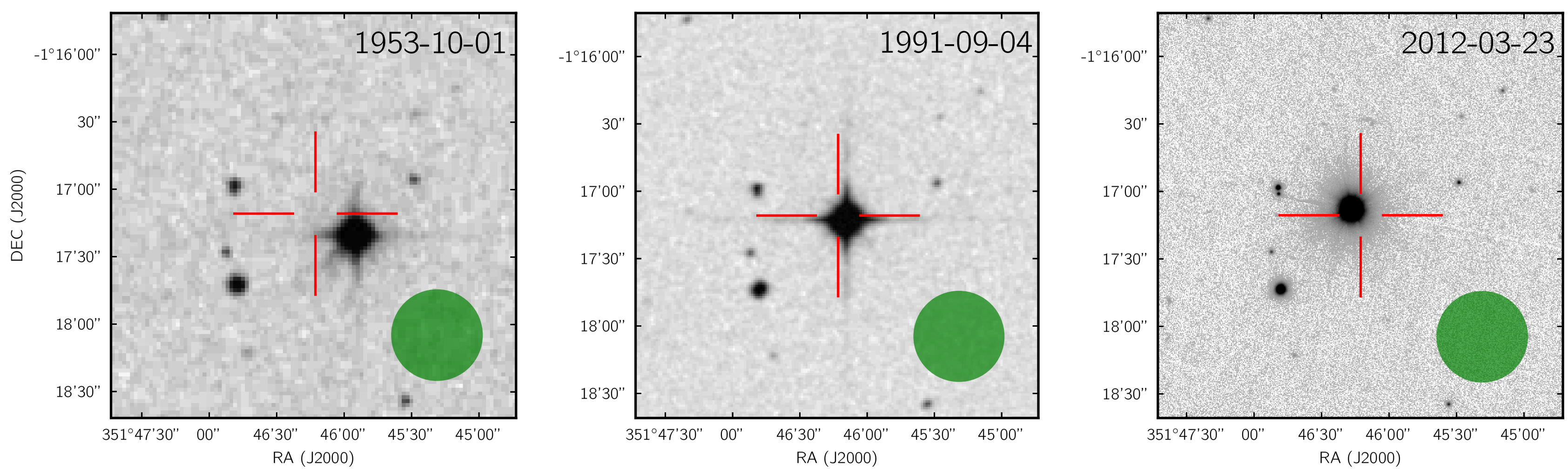

Figure 3.7: GJ 9827 from the POSS-I and II from year 1953 and 1991. The third image is from more recent Pan-STARRS in g band from year 2012. No background objects concurrent with current position of GJ 9827 is seen in the archival image. The green circle in each image shows 20" aperture size used for *K2* photometry, meanwhile the reference position of GJ 9827 at the J2000 epoch is indicated with a red reticle.

of 1:3:5, GJ 9827 c and b period ratio deviate from 3:1 ratio by +0.5%, whereas period of GJ 9827 d and c deviates 5:3 by +2.0%. Such small positive deviation from the exact resonance has been reported in other *Kepler* multiple planet systems (Fabrycky et al. 2014). In fact, the period ratio of GJ 9827 c and d is 1.69994 ± 0.00003 ($\sim$1.7), where Steffen & Hwang (2015) reported the presence of a modest peak in their sample of *Kepler* multiple planet systems. Examples of second order resonances in our own solar system, as well as in exoplanetary architectures have motivated a dynamical explanation regarding their origin (Mustill & Wyatt 2011; Xu & Lai 2017), and a dynamical study of GJ 9827 could be useful in answering questions pertaining to such architecture.

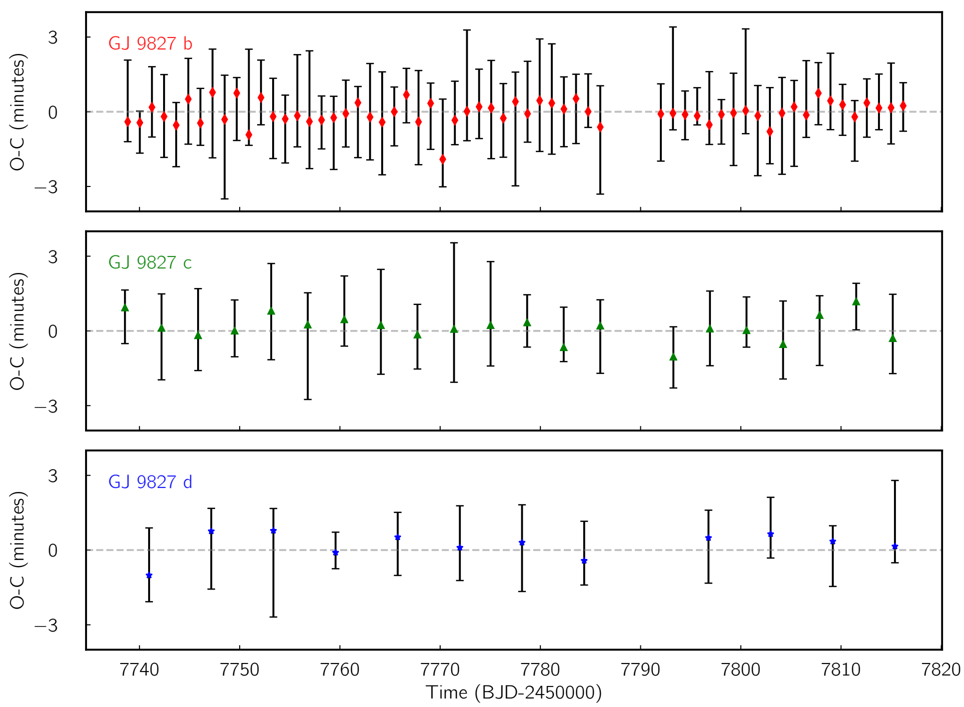

Figure 3.8: O-C Diagram for GJ 9827 b, c and d. The O-C signal and errors are estimated using MCMC fit using model created with transit parameters. No significant TTVs greater than three minutes is detected.

3.7 RV Data

An intense campaign was conducted using FIES, HARPS, and HARPS-N instruments by the `KESPRINT` team in order to determine the mass of the three planets, the result of which has been reported in Prieto-Arranz et al. (2018). While precision of RV data has improved over the years, the systematics such as RV jitter, as well as correlated spot-RV modulation still makes it difficult when looking for a comparatively weaker signals (e.g. 1–5 m s^{-1}). Prior to our effort, Teske et al. (2018) published a paper using a longer RV campaign with data going as far back as 2009. However, the values reported in this paper are discrepant to those reported by `KESPRINT` (see Table 3.3), which additionally performed a Gaussian process to model out spot related RV modulation (see Figure 3.9). The primary reason for this discrepancy is thought to be spot-modulated RV signals which are particularly difficult to model for long time series data, typically longer than a year. Additionally, Prieto-Arranz et al. (2018) obtained higher precision data, which lends greater credibility to the mass derived by `KESPRINT`. While a statistically significant signal for GJ 9827 b planet was found (see Figure 3.10), mass estimations for GJ 9827 c (see Figure 3.11), and GJ 9827 d (see Figure 3.12) are still up for debate. More RV data are being taken on this system, which will likely help to determine the planetary mass with greater confidence. In our analysis, the RV drift due to stellar spot modulation was modeled using Gaussian processes, which is sometimes known to overfit smaller RV signals. The best fit result for three planets are reported in Table 3.3. For a more detailed description the method employed, please refer to Prieto-Arranz et al. (2018).

Using the mass measured from RV observation (Prieto-Arranz et al. 2018), and the radius measured by *K2* (Niraula et al. 2017), the bulk density of the

Table 3.3: Mass and density of GJ 9827 b, c, and d

Parameter	Unit	GJ 9827b	GJ 9827 c	GJ 9827 d
Teske et al. (2018)				
Mass	$M_\oplus$	7.50 ± 1.52	2.65	4.67
Prieto-Arranz et al. (2018)				
Mass	$M_\oplus$	$3.74^{+0.50}_{-0.48}$	$1.47^{+0.59}_{-0.58}$	$2.38^{+0.71}_{-0.69}$
Density	g cm^{-3}	$4.81^{+1.97}_{-1.33}$	$3.87^{+2.38}_{-1.71}$	$1.42^{+0.75}_{-0.52}$

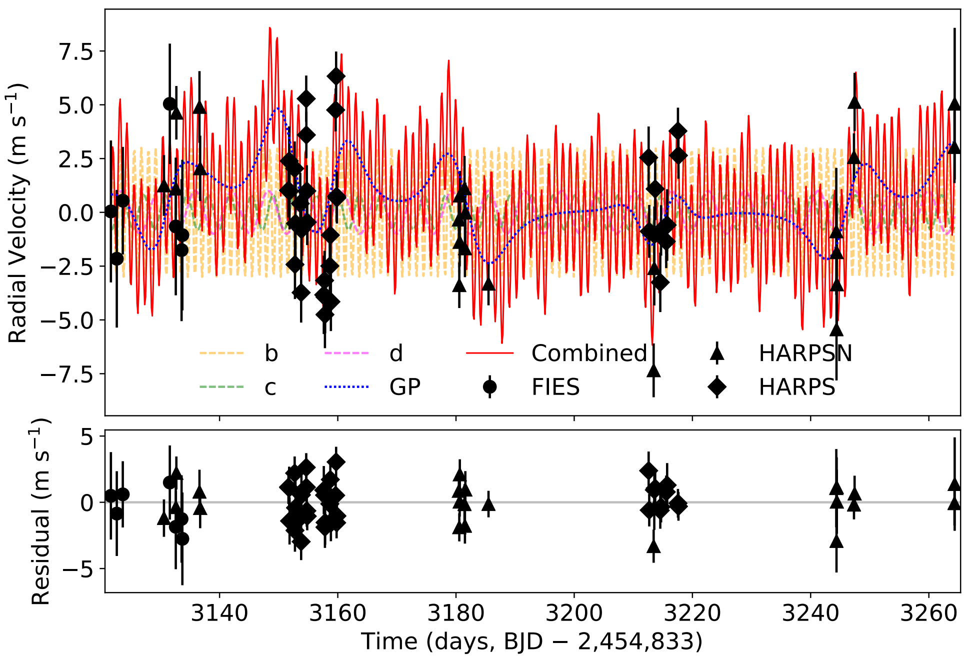

Figure 3.9: Combined RV data taken from different telescopes showing the fit on the top of Gaussian Process adopted from Prieto-Arranz et al. (2018) for all three planets in GJ 9827.

planets was calculated. This showed GJ 9827 b and GJ 9827 c are likely to be rocky planets and GJ 9827 d is likely to be a gaseous planet. Such bulk densities further can be used to see what sort of possible composition the planets can have by assuming a few component models as can be seen in Figure 3.13, and highlight the composition and structure of the planetary interior. It will be possible to have

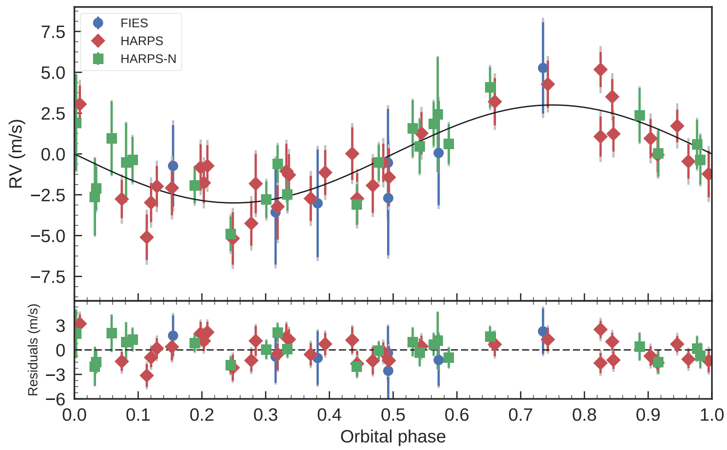

Figure 3.10: RV data phase folded in period of GJ 9827 b as reported in Prieto-Arranz et al. (2018)..

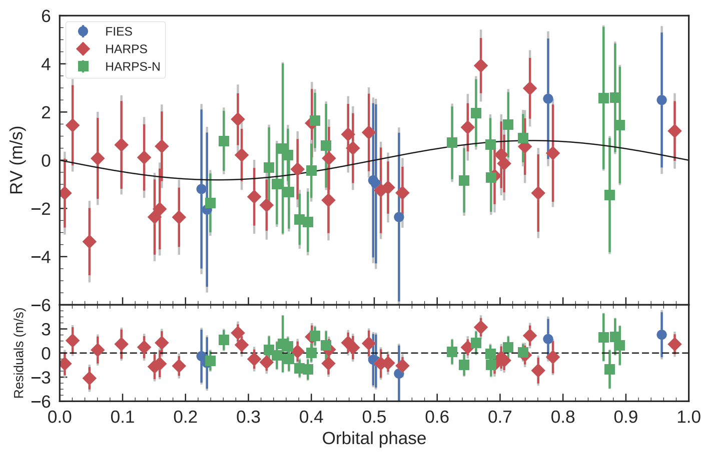

Figure 3.11: RV data phase folded in period of GJ 9827 c as reported in Prieto-Arranz et al. (2018).

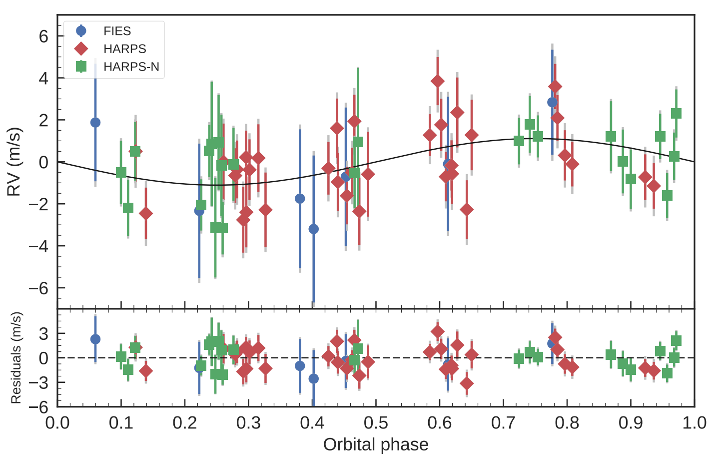

Figure 3.12: RV data phase folded in period of GJ 9827 d as reported in Prieto-Arranz et al. (2018).

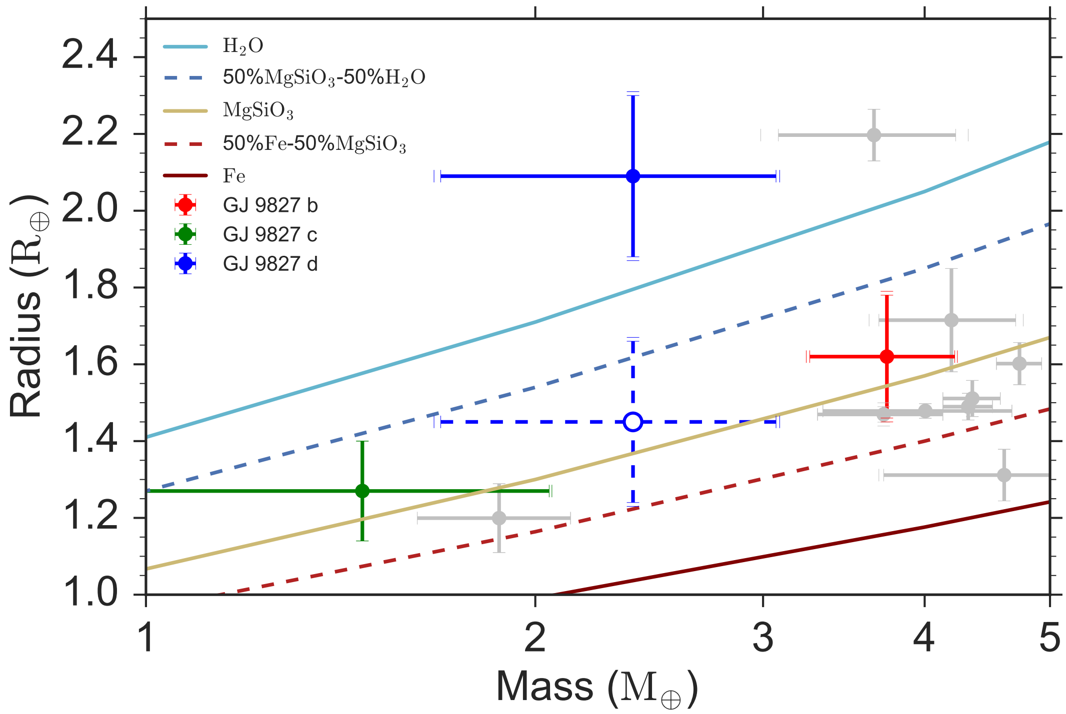

Figure 3.13: Mass-radius relation of GJ 9827 planets against different compositional lines adopted from Prieto-Arranz et al. (2018). Planets are with masses between 1-5 $M_\oplus$ and radii between 1-2.5 $R_\oplus$ as registered in the TEPCat(Transiting Extrasolar Planet Catalogue) database are also shown.

a more informed discussion about the system, as the atmosphere of such planets are characterized.

3.8 Dynamical Studies

Dynamical studies in the past have helped to rule out the solution space where multiple planetary systems are unstable (Wittenmyer et al. 2007). I similarly performed the dynamical stability test of the GJ 9827 system with the help of `rebound` (Rein & Tamayo 2015), using orbital parameters from Niraula et al. (2017), and mass from Prieto-Arranz et al. (2018). A visualization of which is presented in Figure 3.14, which shows a very small mutual inclination of the plan-

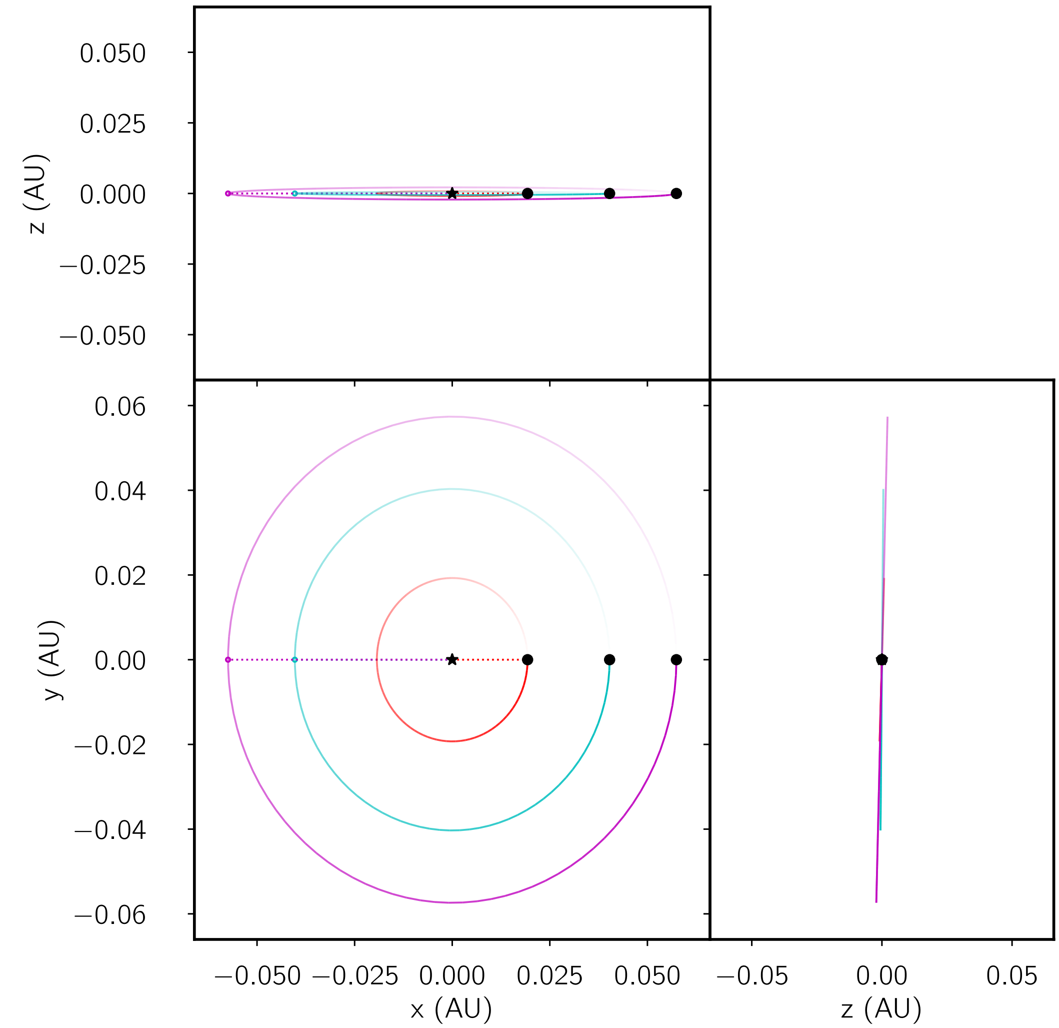

Figure 3.14: Orbital configuration of GJ 9827 made with the help of `rebound`. The $x - y$ plane represents the plane of zero inclination.

ets. Multiple simulations were run (100), and the system was found to be stable for over 100,000 years in most of them (99 out of 100). Small librations ($\sim 10^{-4}$) of eccentricity were observed for all three planets (see Figure 3.15). However, the more interesting question in regards to dynamics of the system itself is how did period ratio close of 1:3:5 originate, which is rare among the multiple planetary systems discovered so far (Prieto-Arranz et al. 2018). Understanding the origins of

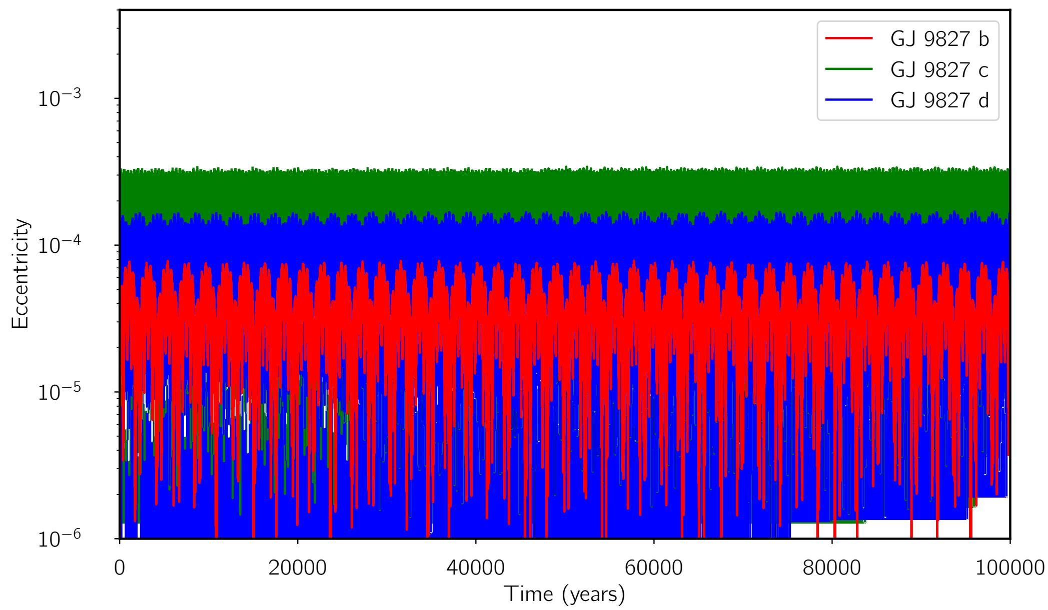

Figure 3.15: The eccentricity libration of planets GJ 9827 b, c and d.

the planetary architecture would also help in distinguishing if the planets formed in-situ or migrated from outer disks. The current paradigm for answering questions pertaining to planetary architecture is to run simulations beginning from the early proto-planetary disk (Tamayo et al. 2017). However, such research is outside the scope of this work.

3.9 Atmospheric Signal

Atmospheric characterization provides an opportunity to not only measure the current conditions in the planetary atmosphere, but also put constraints on formation history and interior structure (Owen et al. 1999), interactions with the host star (Cauley et al. 2017), atmospheric and planetary evolution (Öberg et al. 2011), and biological processes (Meadows & Seager 2010). The planets in the GJ 9827 system offer excellent opportunities to characterize their atmospheres.

Figure 3.16 displays a relative atmospheric detection S/N metric (normalized to GJ 9827 b) for all well characterized exoplanets with $R_p < 3R_\oplus$. The sample of small exoplanets, totaling 603,[4] is taken from the NASA Exoplanet Archive.[5] The atmospheric signal is calculated in a similar way to Gillon et al. (2016) with an effective scale height ($h_{\rm eff} = 7H$; Miller-Ricci et al. 2009) using the equilibrium temperature, a Bond albedo of $\alpha = 0.3$, and an atmospheric mean molecular weight $\mu = 20$. However, since we calculate the relative signal and assume identical properties for all atmospheres, these values do not affect our results but are included for completeness. The atmospheric signal is dominated by the atmospheric scale height, favoring hot, extended atmospheres, and the host star radius, favoring small, cool stars. The relative S/N calculation scales the atmospheric signal with the properties that make it possible to detect and measure this signal,

$$\frac{S/N}{S/N_{\rm Ref}} = \frac{W}{W_{\rm Ref}}\sqrt{10^{-0.4(J-J_{\rm Ref})}}\sqrt{\frac{P_{\rm Ref}T_{14}}{PT_{14_{\rm Ref}}}}, \tag{3.1a}$$

$$W = \frac{2R_p h_{\rm eff}}{R_*^2}. \tag{3.1b}$$

We use the J-band flux (e.g., H_2O measurements with *JWST*; Beichman et al. 2014), and scale by the duration of the transit and the frequency of transits. Given that sensitive atmospheric observations will likely require many transits to build sufficient signal (e.g., Cowan et al. 2015), we have used a metric that optimizes the S/N over a period of time rather than a per-transit metric.

In our initial calculation, all three planets in the GJ 9827 system were among the top 20 candidates in terms of the S/N for atmospheric characterization, which

[4]as of 30 December, 2017

[5]https://exoplanetarchive.ipac.caltech.edu

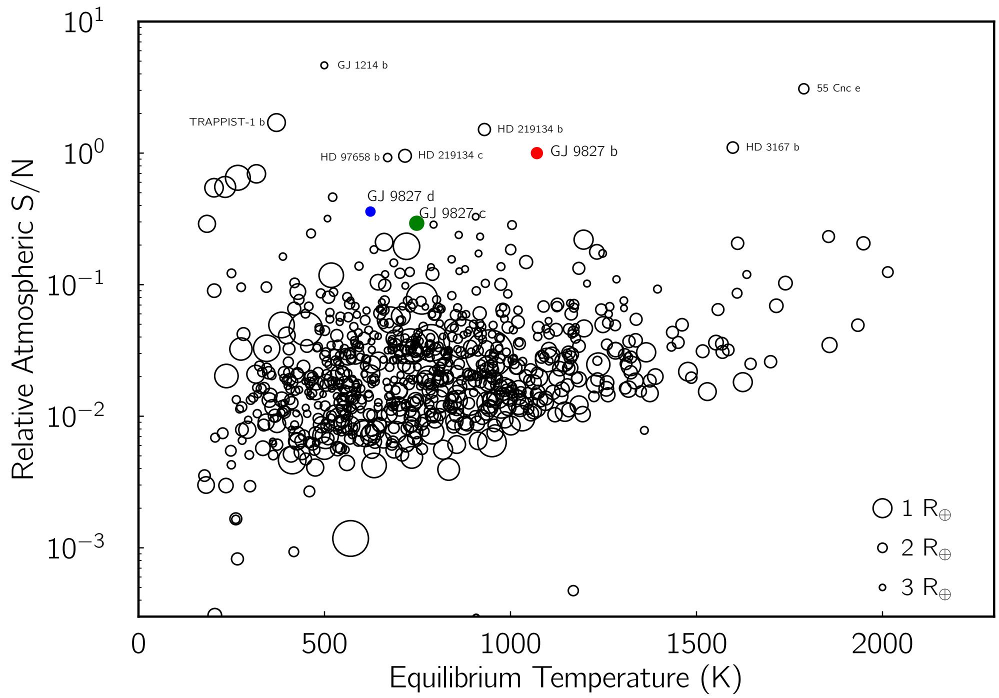

Figure 3.16: Figure adopted from Niraula et al. (2017) showing relative S/N ratio of an atmospheric signal for all exoplanet candidates with $R < 3R_{\oplus}$. The GJ 9827 planets are the filled colored symbols with GJ 9827 b used as the S/N reference. Using this metric, GJ 9827 b is ranked as the sixth most favorable super-Earth for atmospheric characterization.

is mainly a consequence of the brightness of this nearby cool, small, star. This highlights the powerful impact nearby stars have on exoplanet characterization given the relative brightness of even small host stars, providing strong atmospheric signals at high S/N. Using this metric, GJ 9827 b is ranked the 6th best target for atmospheric characterization, after GJ 1214 b, 55 Cnc e, TRAPPIST-1 b, HD 219134 b, and HD 3167 b. After the RV campaign, the planetary masses could be independently estimated. In this improved estimation we found that the planets are even better atmospheric targets than originally estimated. Based on this more recent calculation, GJ 9827 d ranks as the fourth best candidate

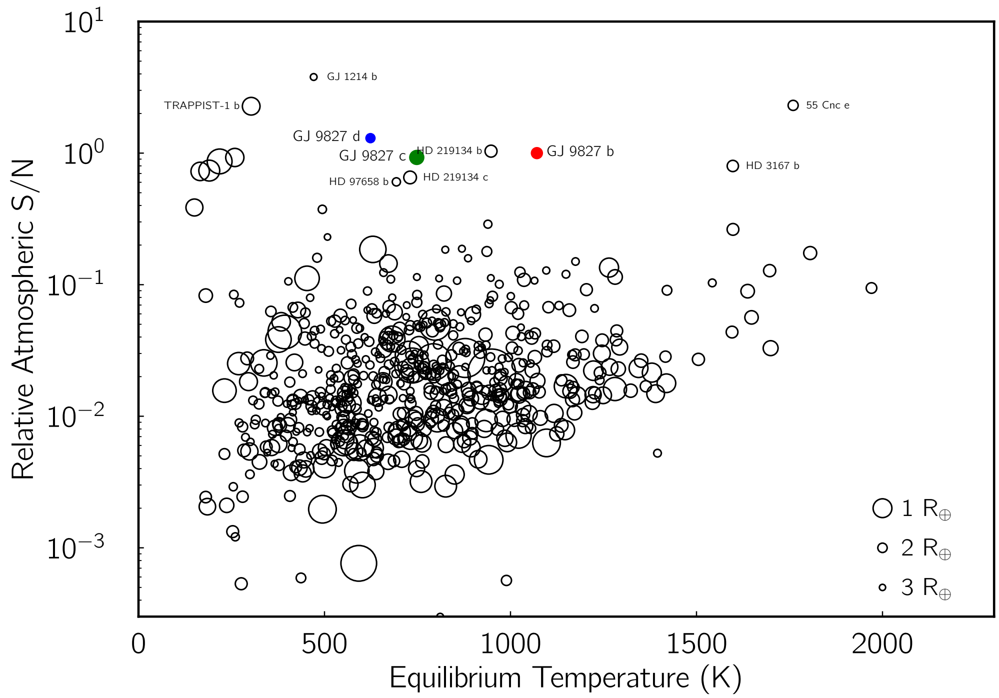

Figure 3.17: An updated version of GJ 9827 figure after the mass estimation which is presented in Prieto-Arranz et al. (2018). With the new mass estimation, GJ 9827 d is expected to have the best SNR among the three planets despite its temperature.

overall (behind GJ 1214 b, 55 Cnc e, and TRAPPIST-1 b), and GJ 9827 b and c rank sixth and seventh, respectively, among the 603 transiting planets with radii $<3R_{\oplus}$, as shown in Figure 3.17.

Given that all three of the GJ 9827 planets are near commensurability, there are regular opportunities to observe two, or even all three transits at approximately the same time. For example, see the *K2* signal at BJD 2457753, which occurs on average every 150 days (assuming 6 hours of observation). The wait is shorter for simultaneous transits of two planets. Transit overlap occurs for GJ 9827 b and c over 6 hours of observation on average every 8.7 days; for GJ 9827 c and d around 53 days, and for GJ 9827 b and d around 15 days. This allows to arrange for a strategic observation session to observe all of three transits.

We, therefore, have submitted a *Spitzer* proposal to obtain IR observations. The simulated data from this observation would look as in Figure 3.18.

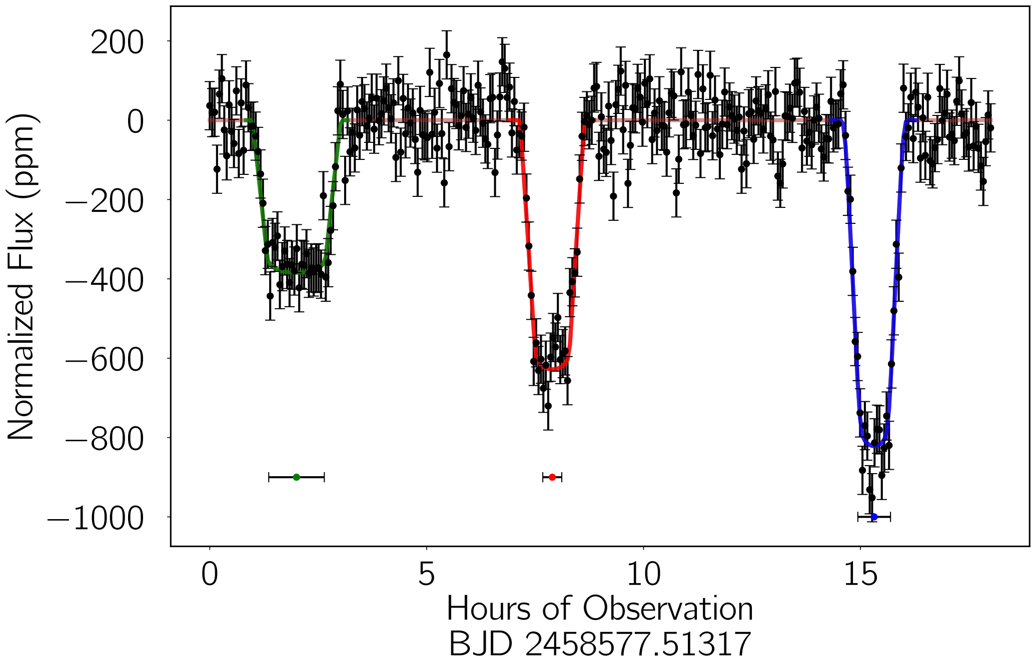

Figure 3.18: Modeled transit in *Spitzer* from one of the recently submitted proposals. Such observations would to be helpful in constraining the atmospheric signal in *Spitzer* band as well as determining the ephemerides of the planets with better precision. The red, green, and blue error bars show the calculated uncertainties in ephemerides for GJ 9827 b, c and d respectively.

Using `exotransmit` and using planetary parameters, I model what the spectral signal of the transmission spectral for three planets would look like (see Figure 3.19). I consider the presence of molecules such as CH_4, CO_2, CO, H_2O, O_2, O_3, OH, TiO, VO, Na, and K, as well as turn on scattering and collision induced absorption flags. `Exotransmit` has been adapted to take into account the mass, temperature, atmospheric composition, surface gravity, and size of the exoplanets, therefore can be used for a range of planetary sizes. For more details on how `exotransmit` works please see Kempton et al. (2017). In our upcoming *Hubble*

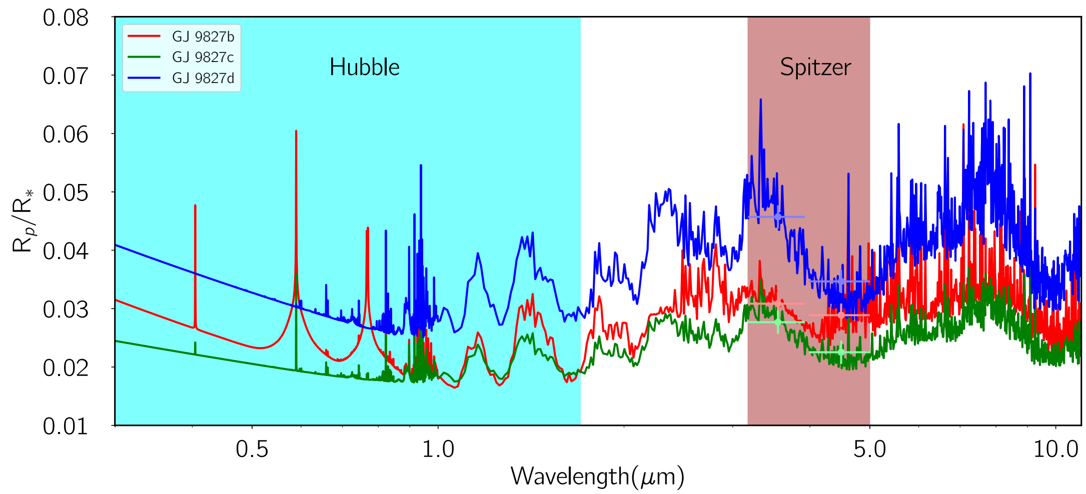

Figure 3.19: Figure showing the atmospheric modeling for three planets using exotransmit. Undergoing atmospheric characterization will constrain different composition models at various wavelength windows.

observations, we will be looking for absorption in the Lyman-α emission line from the atmosphere of GJ 9827 b which will put constraints its the hydrogen content of the atmosphere. Besides, we have also put an *Spitzer* observation at 3.6 μm, which would provide the first step towards infrared atmospheric characterization.

Thus, the discovery of GJ 9827 planetary system is exciting particularly because of the atmospheric characterization possibility it offered. With current instrument such as *Hubble*, super-Earths' atmosphere are still very hard to characterize, and some of the promising candidates had worse than expected transmission spectra (Kreidberg et al. 2014). With the launch of *JWST*, a telescope with larger gathering power, exoplaneteers will have a powerful tool to probe the atmospheres of super-Earths. It will therefore mark the beginning of a new era in the exoplanet atmospheric studies.

Chapter 4

Phase Curves

Phase curves are one of the most powerful tools in the hands of astronomers to characterize an exoplanet, and are particularly useful in the case of hot Jupiters. As the planet moves around the star, the amount of light coming off the system (star and planet) shows characteristic modulation at the orbital period of the planet. Harrington et al. (2006) used Multiband Imaging Photometer for *Spitzer* (MIPS) to first demonstrate phase curve variation in case of υ Andromeda b by taking photometric snapshots at different phases. A year later, Knutson et al. (2007) studied the thermal phase curve in HD 189733 b with data covering the complete phase of the planet. While thermal windows are ideal for observing the phase curves of the planet as the planetary emission often peak in the infrared, the limited number of infrared instruments, ideally placed outside the Earth's atmosphere, has been the primary bottleneck for such studies. This is where high precision optical photometry has come in to fill the void.

With *Kepler*, we are able to obtain precise photometry for thousands of targets in its field of view. With precision approaching 10 ppm, sometimes better, some of transiting *Kepler* hot-Jupiters exhibited optical phase curves (Mislis & Hodgkin 2012; Angerhausen et al. 2015). The phase curves have also been used as a tool of discovery for non-transiting systems (Millholland & Laughlin 2017). Future missions such as *CHEOPS*, *PLATO*, and *TESS* similarly will provide more opportunities for the characterization of planets with the help of the phase curves.

Phase curve analysis has already become a popular technique within the exoplanet transit community. The observation of thermal emission has been used to map the temperature distribution in the planetary atmosphere, which in turn helps to constrain the atmospheric models. Such information can shed light on some of the common features of atmosphere such as superrotating jets (Knutson et al. 2007) or temperature inversions (Wong et al. 2016). Atmospheric circulation models of hot Jupiters had predicted a phase offset for the peak of the phase curve (Showman & Guillot 2002) even before they were detected by Knutson et al. (2007) using *Spitzer* observations of HD 189733 b. Besides, looking at the variation in the phase curve, information on the longitudinal variation of the temperature can be obtained which in turn can be used to model in greater detail the atmospheric patterns in such planets (Rauscher et al. 2008; Showman et al. 2015). Phase curves also help to look into the energy budget of the planets (Demory 2014) providing the heat transport efficiency of the atmosphere and the day-night temperature contrast. Meanwhile, the timing of the secondary eclipse itself is a great way to characterize the orbital parameters such as eccentricity, and longitude of periastron (Huber et al. 2017) which are poorly constrained when obtained by fitting the primary transit alone.

Optical phase curves are often trickier than their thermal counterpart because of the smaller contrast ratio between the planet and its host star. In addition, there are more contributing components. While reflectivity (the stellar light reflected off the planet) is often the dominating factor, there are other contributors such as ellipsoidal variation, thermal emission, and Doppler beaming. Ellipsoidal variation is related to the shape distortion of the star (Esteves et al. 2013), and Doppler boosting is due to relativistic Doppler effects (Esteves et al. 2013). A more complete model would also add other heat sources on the planet such as the effect of the tidal heating of the planet (Demory 2014). When starting the project, I did not expect the photometric precision of *K2* to distinguish between different models, thus only a simplistic model with only reflective component has been considered throughout this work, although later it was observed that more some of the targets did show potential ellipsoidal variation.

4.1 Promising Candidates

There has not been a systematic search for secondary eclipses in *K2*, and only a handful of candidates with phase curve have been reported (Malavolta et al. 2018). In looking for the phase curve, I first searched for the secondary transit, as often the amplitude of the phase curve is comparable to the amplitude of the secondary transit. For this, I consider all the planets detected so far by *K2* as listed in the NASA Exoplanet Archive[1] and calculate the expected Signal to Noise Ratio (SNR) for secondary eclipse using equation Equation 4.2. Note this includes planet hosting systems discovered using ground based telescopes such as WASP-28, WASP-55, WASP-47, WASP-75, WASP-107, WASP-118, WASP-151, QATAR-2, HAT-P-56, HATS-9 and HATS-11, which were specifically proposed for *K2* for refining their orbital parameters as well as potential observation of their phase curves. Altogether, around 307 planets were considered most of which are reported in Crossfield et al. (2016); Dressing et al. (2017); Mayo et al. (2018). These were targets mostly through Campaign 10, as well as from later campaigns if they have been registered in the NASA Exoplanet Archive. One of the targets for which the paper still is under review has been added with the permission of the

[1]exoplanetarchive.ipac.caltech.edu

author. The expected SNR is calculated using Equation 4.1, where an optimistic geometric albedo estimate of A_g=0.4 is used:

$$\delta_{\text{Sec}} = A_g \left(\frac{R_p/R_*}{a/R_*} \right)^2 \ , \tag{4.1}$$

where δ_{Sec} is the expected secondary eclipse depth. The SNR is also affected by phase folding as follows:

$$\text{SNR} = \frac{\delta_{\text{Sec}}}{\sigma} \left(\frac{80}{\text{P days}} \right)^{\frac{1}{2}} , \tag{4.2}$$

where σ is the expected photometric precision of the data is which calculated based on its magnitude, and P is the orbital period. Both equations show how short period planets are preferable for the detection of the secondary eclipse.

In estimating the depth of the secondary eclipse, I have largely ignored the thermal emission of the planet primarily as they are usually negligible, and scales proportionately with the reflected component. Based on this calculation, it is not surprising that neither phase curve nor secondary eclipse was reported in WASP-157b (Močnik et al. 2016), a planetary host which was observed with *K2* with such motivation, for which the calculation estimates the SNR to be below 1. All the planetary candidates with SNR greater than 1 are considered for detailed study during which different combinations of flattening process and detrending algorithms were considered. All such planets are catalogued in Table 4.1 and the distribution of expected SNR are shown in Figure 4.1. The obtained light curves and best attempts to obtain the phase curves are sequentially presented from Figure 4.3 – 4.14 .

Table 4.1: Best Candidates for the Secondary Eclipse Detection

Index	**Name**	**K-Mag**	**Period (Days)**	δ_{sec} **(ppm)**	**SNR**	δ_{sec} **Detection**	**Phase Curve Detection**
1	K2-31	10.78	1.25785	199.2	19	N	**Y**
2	K2-183b	12.85	0.46927	152.8	7.4	N	N
3	HAT-P-56	10.91	2.79083	109.5	6.5	N	N
4	K2-141	11.39	0.28032	31.6	4.6	**Y**	**Y**
5	K2-34	11.55	2.99561	85.2	3.5	N	N
6	K2-131	12.12	0.3693	23.5	2.0	N	N
7	HD 3167b	8.94	0.95964	7.3	1.9	N	N
8	K2-29	12.53	3.25883	72.9	1.7	N	N
9	K2-107	12.92	3.31392	83.3	1.5	**Y**	**Y**
10	WASP-47b	11.9	4.16071	44.1	1.3	N	N
11	K2-106	12.01	0.57134	16.3	1.1	N	N

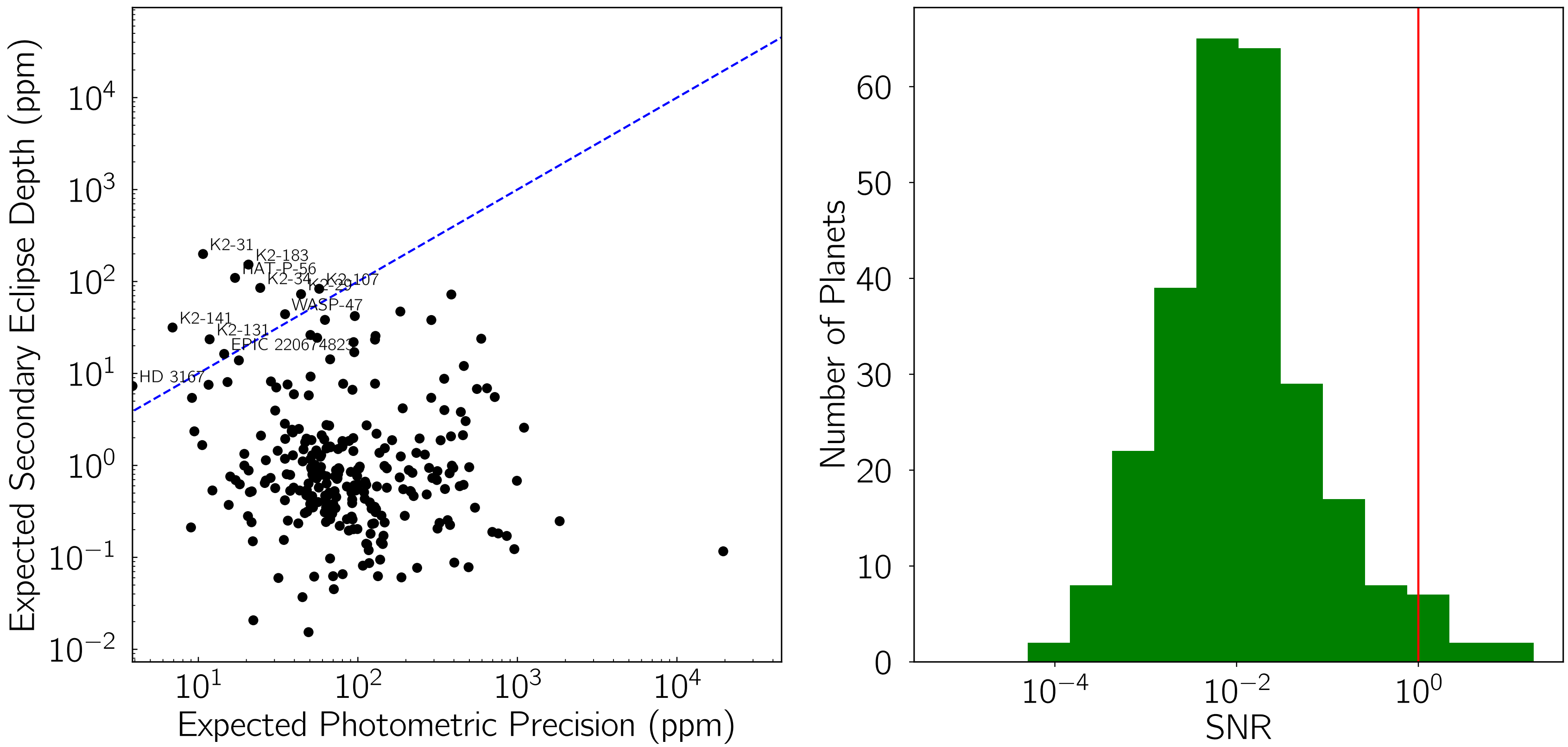

Figure 4.1: A comprehensive search for good candidates for phase curves. The calculation shows 11 candidates are expected to have secondary eclipse with SNR greater than 1. The red region in the left figure shows targets for which secondary eclipse is not statistically significant to be observed.

4.2 Modeling Phase Curve

In order to model the phase curves, it becomes necessary to model the planets motion around its host star. Any motion of the planet around its host star can be parameterized as in Murray & Dermott (1999) using mean anomaly (M), eccentric anomaly (E), and true anomaly (ν). These three quantities are related to each other as the following:

$$\begin{aligned} M(t) &= M_0 + \frac{2\pi t}{P}, \\ E(t) &= M(t) + e \sin E, \\ \nu(t) &= 2 \arctan \left(\sqrt{\frac{1-e}{1+e}} \tan \frac{E(t)}{2} \right). \end{aligned} \tag{4.3}$$

where, M_0 is the initial mean anomaly.

As for the flux from the system itself, it is the combination from the star and planetary systems combined. Thus, it can be written as:

$$f(t) = \frac{F_{\mathrm{Ref}}(t)}{F_*} + \frac{F_{\mathrm{thermal}}(t)}{F_*} + \frac{F_{\mathrm{Ell}}(t)}{F_*} + \frac{F_{\mathrm{Dop}}(t)}{F_*}. \tag{4.4}$$

The reflectivity, thermal phase variation and Doppler beaming due to planet motion around its host star has a characteristic period same as the orbital period, whereas, the ellipsoidal variation has half the period of the orbital period. In addition to these signals, there are modulations associated with stellar oscillation, and stellar rotation. It, therefore, becomes a difficult task to disentangle the signal when the orbital period is comparable with the stellar rotation period as is the case with some of our targets. Each of the variations described in Equation 4.4 can be mathematically characterized. However, as mentioned earlier we only consider the model with the reflective component. Our model is based on Esteves et al.

(2013), which has a comprehensive discussion on all of the different components. For the reflective component, the planet is considered to be a Lambertian sphere, following the cosine emission law. This can be mathematically expressed as:

$$\begin{aligned} \frac{F_{\rm ref}(t)}{F_*} &= \frac{A_g}{2}\frac{R_p^2}{[d(t)]^2}[1+\cos\theta(t)], \\ &= \frac{A_g}{2}\frac{(R_p/R_*)^2}{(d(t)/R_*)^2}[1+\cos\theta(t)], \end{aligned} \tag{4.5}$$

where, the angle ($\theta(t)$) which is the sum of true anomaly (ν(t)) and the argument of periastron ($\omega(t)$) (i.e. $\theta(t) = \nu(t) + \omega$), R_p is the radius of the planet, R_* is the stellar radius, and $d(t)$ is the distance of the planet from the star. For a circular orbit, this is quite easy to model, however for an eccentric orbit it requires solving Kepler's Equation (see Equation 4.3) before calculating how the reflective component varies with the phase.

For a perfectly circular orbit the secondary eclipse is expected to occur at phase=0.5 and the fact that the secondary eclipse depth is comparable to the amplitude of the phase curve can be used to assess the fidelity of the signal. Note that in modeling the phase curve, the deviation from sinusoidal variation occurs only when the planetary orbital has some eccentricity. Thus, we have reason to believe the orbit has been circularized for these close-in planets, the more complicated models with an eccentric orbit will not be considered here.

Phase curves also demand a very thorough understanding and characterization of the light curve. In fact, during a proper characterization of the light curve, one can see the star spots disappearing behind the line of sight (Dai & Winn 2017; Močnik et al. 2017). Such detailed analysis means that any outstanding anomalies would be an indication of the phenomenon that is not previously reported. For example, with this level of detail it might be possible to detect slight dips in the phase corresponding to L4 and L5 points, where Trojan objects can stay orbit in a stable configuration. Usually, L4 or L5 in the planet-star system lead or trail the planet by 60°, which will be discussed in greater detail later. Note this is also true for the eccentric orbits, with a slight modification in the calculation (Todoran & Roman 1992).

4.3 Data Pre-Processing

In the process of extracting the phase curve, it becomes necessary to remove the variation in the light curve primarily associated with spot modulation and other quasi-periodic phenomena. Various techniques are available for flattening the light curve of the stars, but an important question when extracting phase curve signal is what are the chances that it can overfit the phase curve or underfit the stellar modulation signal. In fact, it becomes difficult to detect transit signals around highly variable stars as the photometric variation of the host star can drown the transit signals. For such targets, extracting a phase curve is even more difficult. This bias is clearly observable as most of the planetary optical phase curves are observed in systems where the host star shows smaller amplitude and longer timescale (compared to the orbital period) spot modulation variation.

For this work, I consider three flattening processes: spline fitting, variance fitting, and Gaussian process fitting . For spline fitting, implemented in `scipy`, the knots are drawn at different planetary orbital period intervals, and the degree of polynomial is either 2 or 3. No universal method was found to work. For instance, for fast rotators the spline flattening would underfit the spot modulation. Variance fitting, so called because it fits the data by looking at local variance, overall tended to overfit the phase curve. While this could be remedied by increasing the number of iterations during outlier rejection iterative process, this was not always the ideal solution. While Gaussian process theoretically is the most preferred way (Serrano et al. 2018), the complexity and the computational expenses makes it less desirable. Also as the spots evolve, the spot modulation deviates which although can be modeled can make it difficult to disentangle the signal.

A complete test for fidelity of phase curve signal would require injecting a signal at the target pixels file, and see how each of the detrending algorithm perform. There are different free parameters in every detrending algorithm, and understanding how each one affects the final obtained light curve would be desirable. This is currently outside the scope of my work. However, one of the candidates, K2-141, has a reported phase curve, and it can be used as a benchmark to see how different pipelines handle the phase curve signals. I have also done some preliminary tests, as shown in Figure 4.2 on how different flattening procedures change the reported secondary eclipse depth, and have found that they largely give consistent results. However, note that the spline method is able to best reproduce the phase curve signal that was presented in Malavolta et al. (2018), thus has been primarily used for flattening procedure in obtaining the phase curve.

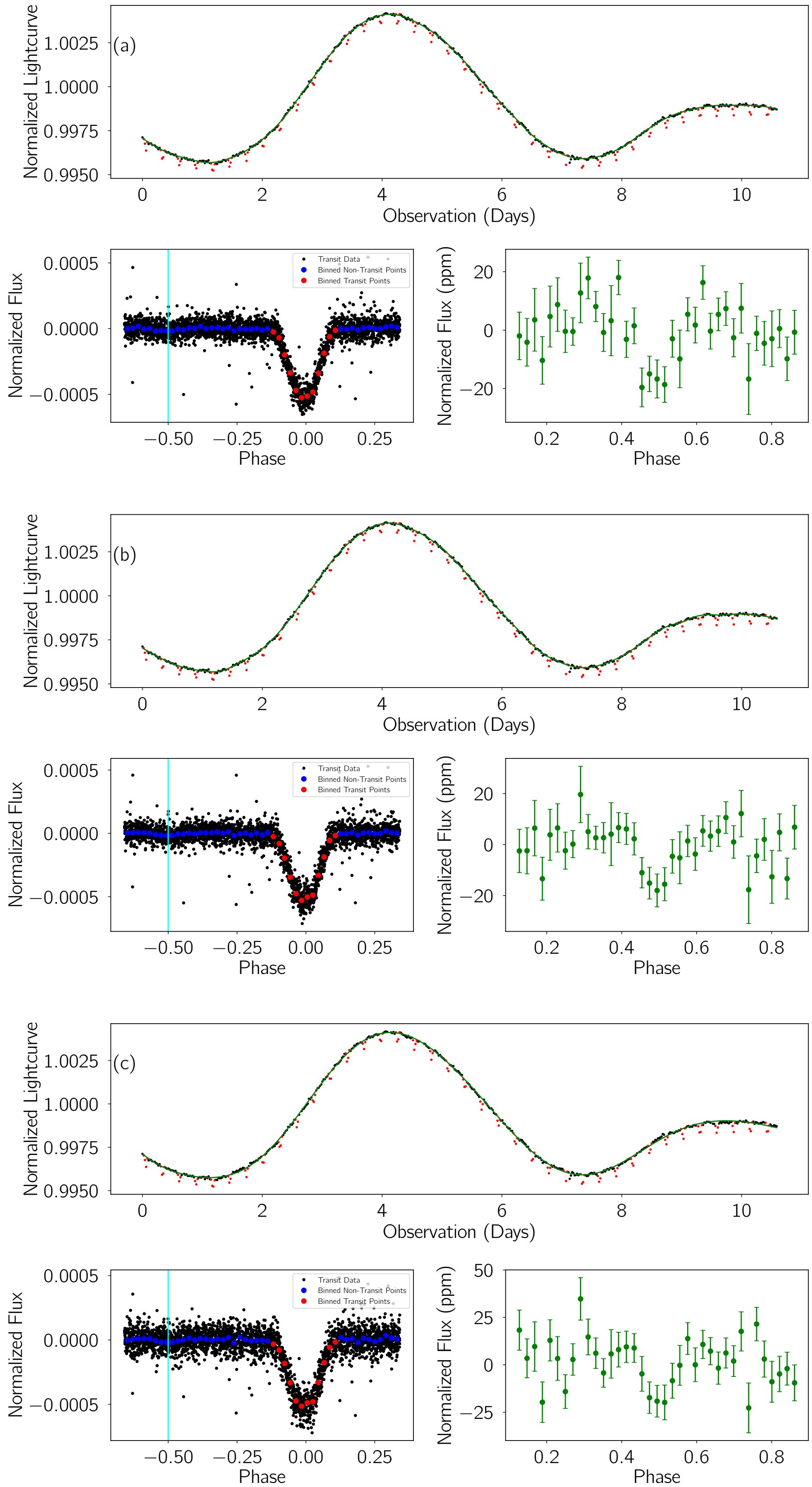

Figure 4.2: A comparison of different flattening methods: (a) spline fitting, (b) variance fitting, and (c) Gaussian Process fitting with sine based exponential kernel (bottom) on the light curve of K2-141. The phase curve is most obvious in the spline based flattening procedure.

4.3.1 K2-141

K2-141 b is one of the ultra-short period planets with period of 0.28032 days (6.7 hours) that was found in Campaign 12 of *K2* (Barragán et al. 2017b; Malavolta et al. 2018). It clearly exhibited a phase curve as was reported in (Malavolta et al. 2018). We obtained data from the authors, and performed spline flattening procedure, and detect the secondary eclipse at depth of 26 ± 3 ppm , and amplitude of reflective component at 11.3 ± 1.3 ppm. The secondary depth signal is higher than twice the amplitude. A similar case was observed in 55 Cnc e (Demory et al. 2016), although why that can be the case is still under discussion.

Table 4.2: Parameters for K2-141 b

Parameters	**Units**	**Malavolta et al. (2018)**	**This work**
Amplitude	ppm	23 ± 4	11.3 ± 1.3
$\delta_{secondary}$	ppm	23 ± 4	26 ± 3
A_g	-	0.30 ± 0.06	0.33 ± 0.04

4.3.2 K2-107

Table 4.3: Parameters for K2-107 b

Parameters	Unit	Value
Eccentricity	-	$0.046^{+0.029}_{-0.019}$
W	Degrees	240±14
$\delta_{secondary}$	ppm	57 ± 7
A_g	-	0.34 ± 0.26

K2-107 was observed to have a secondary eclipse but not at 0.5 phase (see Figure 4.12). Based on the fit, the value of eccentricity is $0.046^{+0.029}_{-0.019}$, which is consistent with the value reported for eccentricity for non-circular fit of 0.06 ± 0.05 in Eigmüller et al. (2017). All other relevant values are reported in Table 4.3. The secondary eclipse was also found by using the methods ascribed in (Huber et al. 2017), and were consistent to what was seen with spline flattening method. Also like K2-141 b, the depth of secondary eclipse of K2-107 b is found to be deeper than the amplitude of the phase curve.

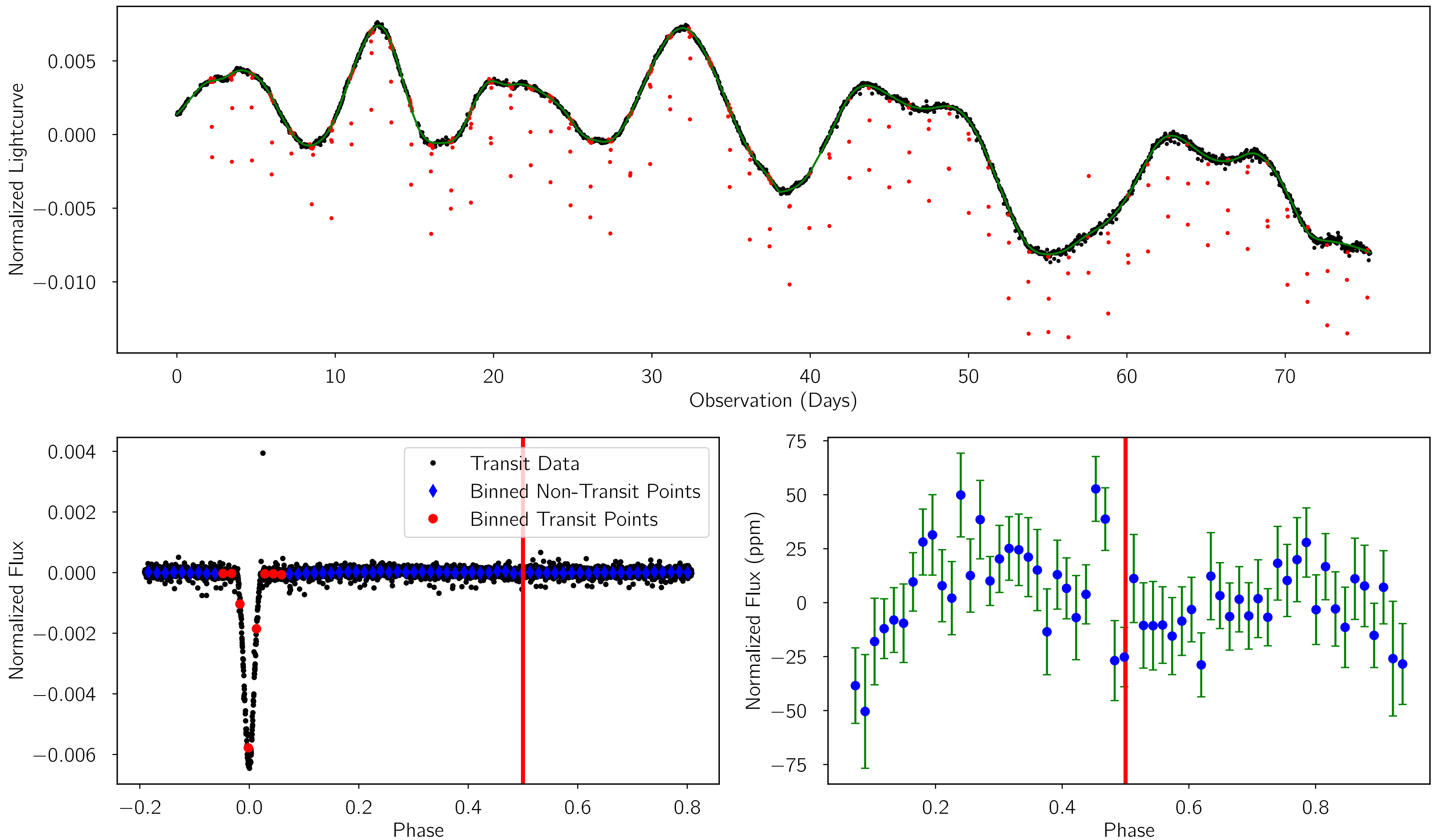

Figure 4.3: Spline fitting of the `K2SFF` detrended light curve of K2-31 which is a planet with period of 1.25785 days. The top panel shows the flattening after rejecting the transit points marked in red. The lower left panel shows the phase folded light curve with potential phase curve related to ellipsoidal variation. The lower right panel shows the binned version after removing the transit. A vertical red line is drawn at the phase=0.5, where the secondary transit is expected to occur.

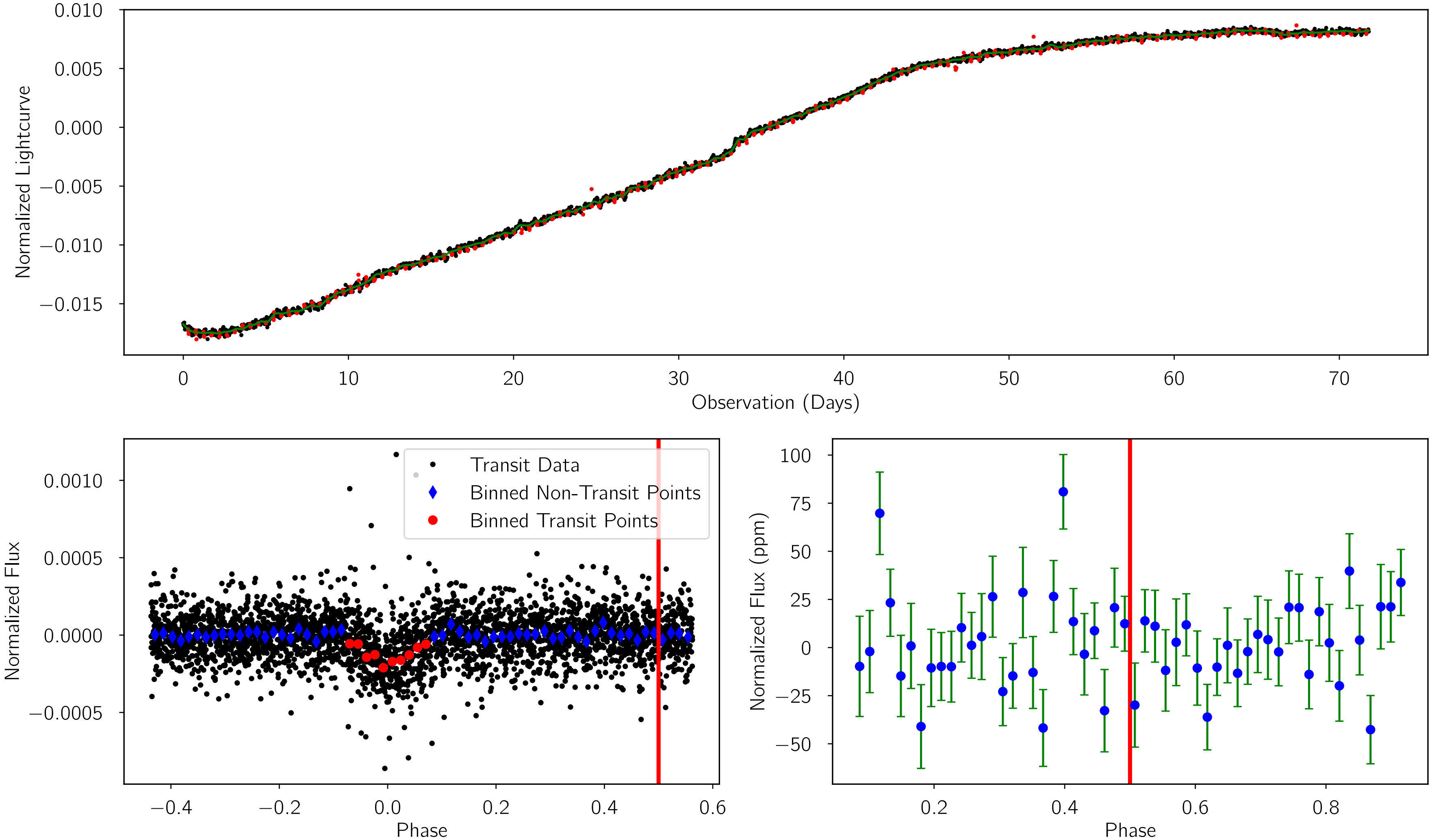

Figure 4.4: Spline fitting of the `K2SFF` detrended light curve of K2-183 which is a planet with period of 0.46927 days. The top panel shows the flattening after rejecting the transit points marked in red. The lower left panel shows the phase folded light curve. The lower right panel shows the binned version after removing the transit. A vertical red line is drawn at the phase=0.5, where the secondary transit is expected to occur.

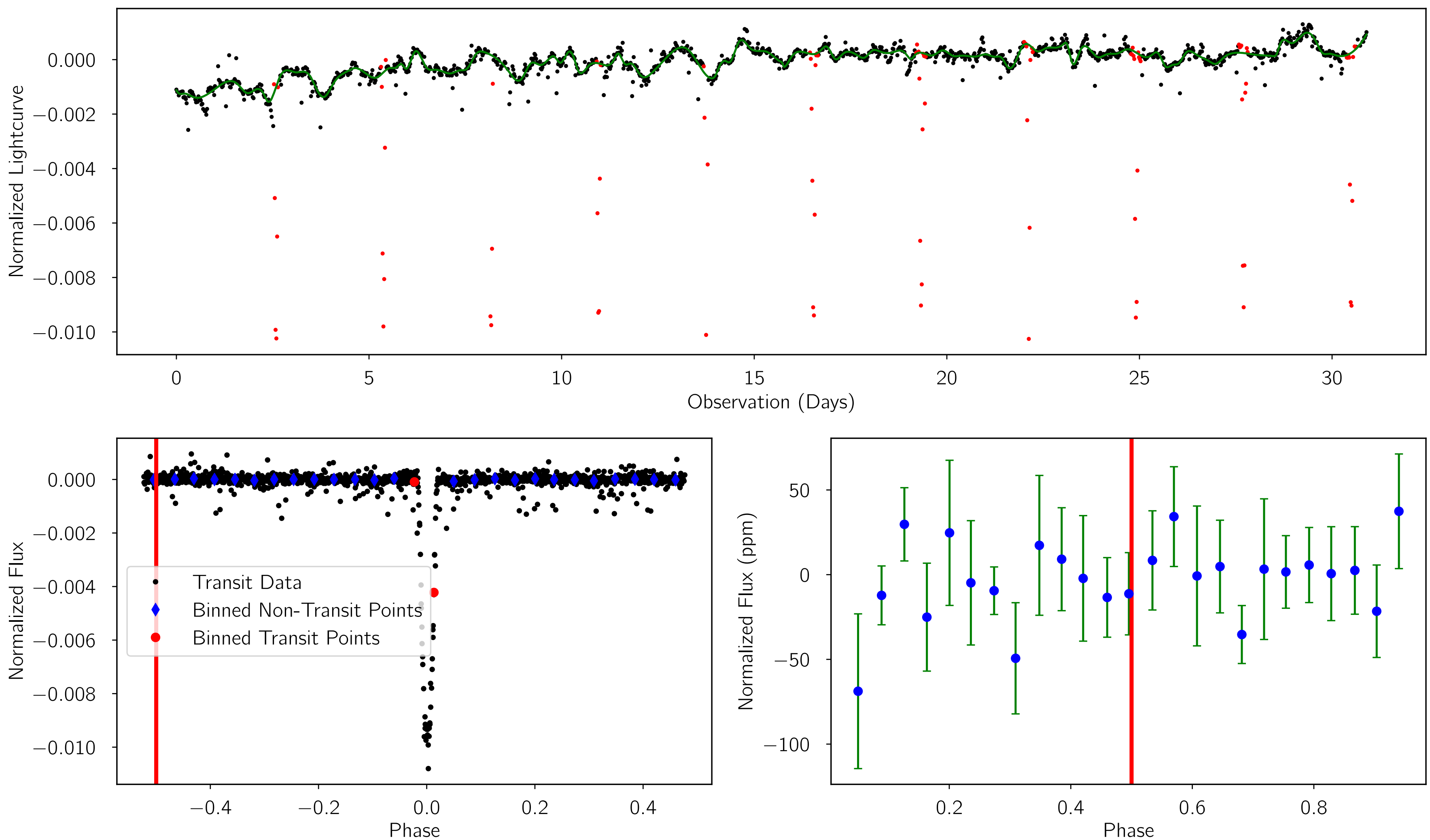

Figure 4.5: Spline fitting of the `K2SFF` detrended light curve of HAT-P 56 which is a planet with period of 2.79083 days. The light curve is much noiser than the expected precision.

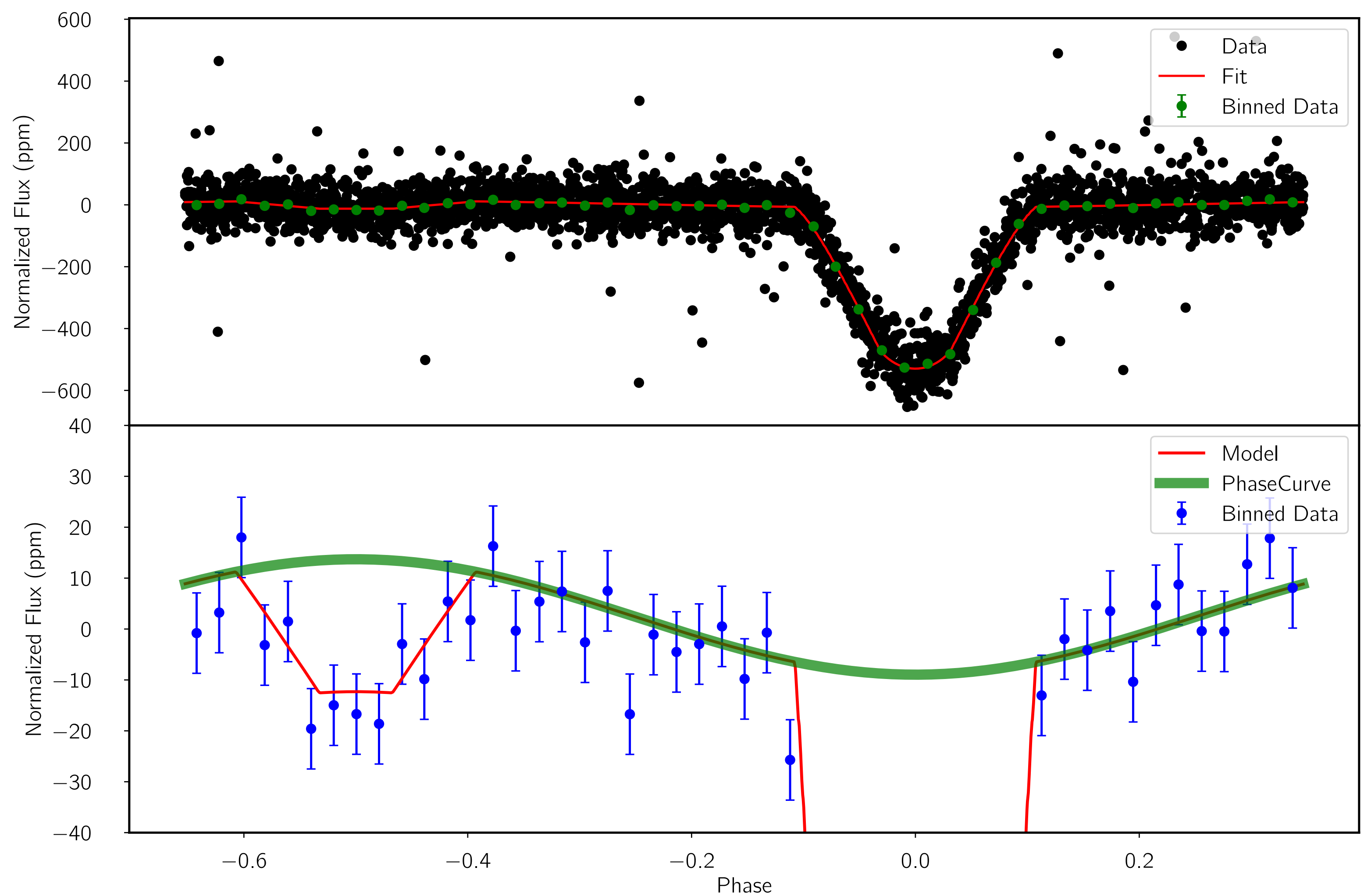

Figure 4.6: Fitting of the phase curve of K2-141 b. The light curve used in this analysis was provided by Dr. Andrew Vanderburg and fitted using `batman`. The upper panel shows both primary and secondary transit, and the lower panel focuses on the secondary transit as well as the phase curve.

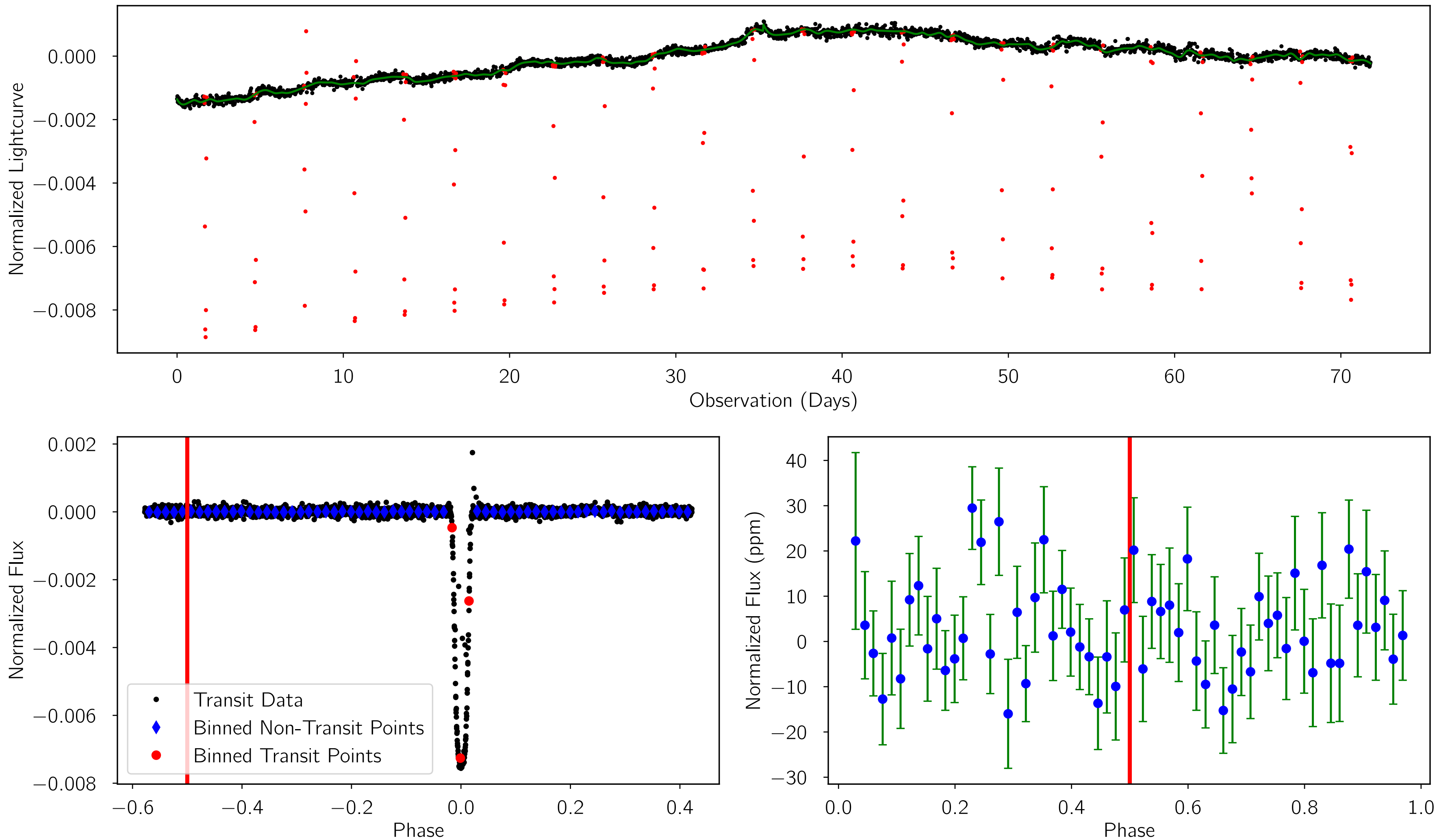

Figure 4.7: most obviouse of the `K2SFF` detrended light curve of K2-34 which is a planet with period of 2.99561 days. The top panel shows the flattening after rejecting the transit points marked in red. The lower left panel shows the phase folded light curve. The lower right panel shows the binned version after removing the transit. A vertical red line is drawn at the phase=0.5, where the secondary transit is expected to occur.

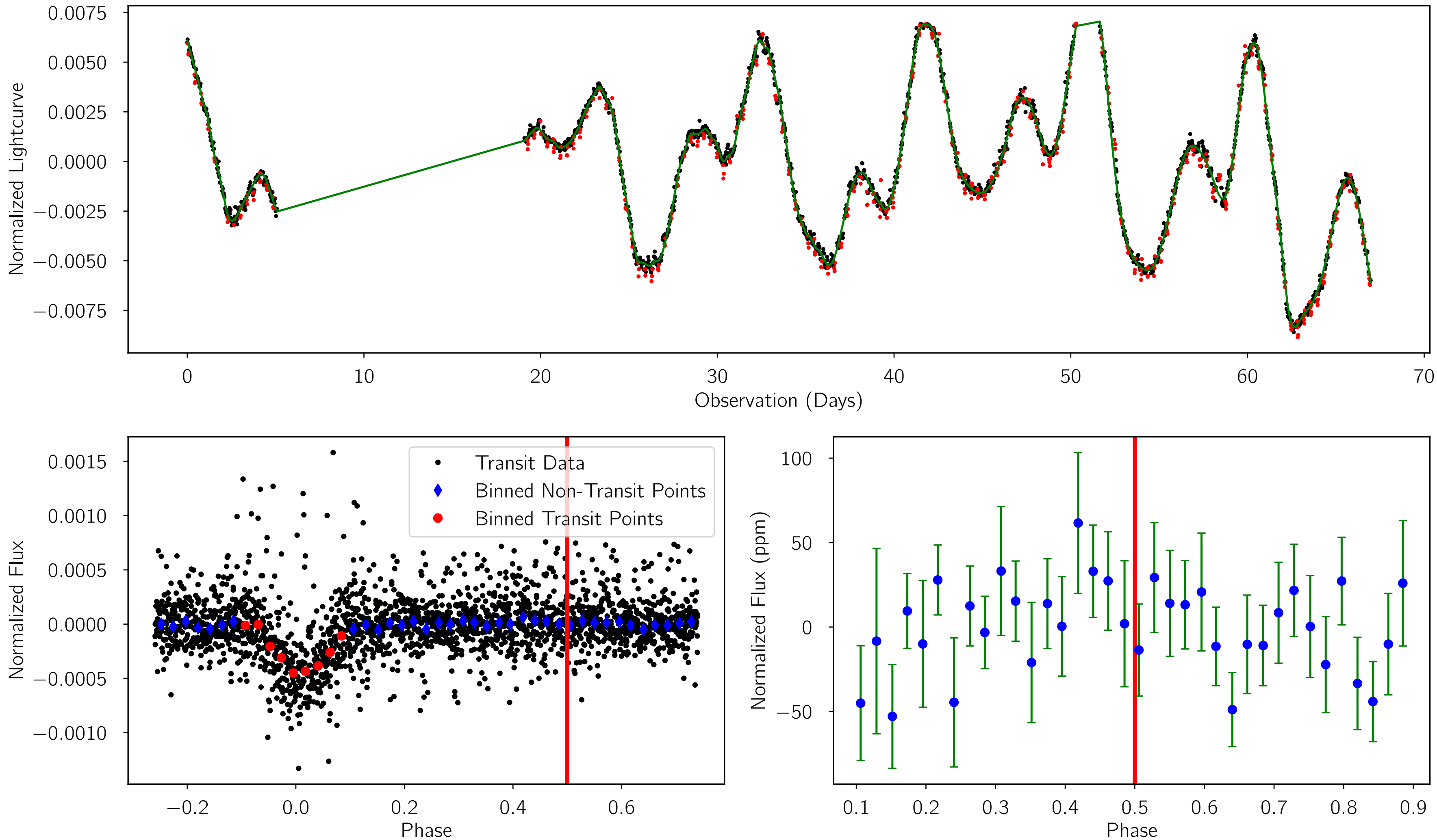

Figure 4.8: Spline fitting of the `K2SFF` detrended light curve of K2-131 which is a planet with period of 0.3693 days. The top panel shows the flattening after rejecting the transit points marked in red. The lower left panel shows the phase folded light curve. The lower right panel shows the binned version after removing the transit. A vertical red line is drawn at the phase=0.5, where the secondary transit is expected to occur.

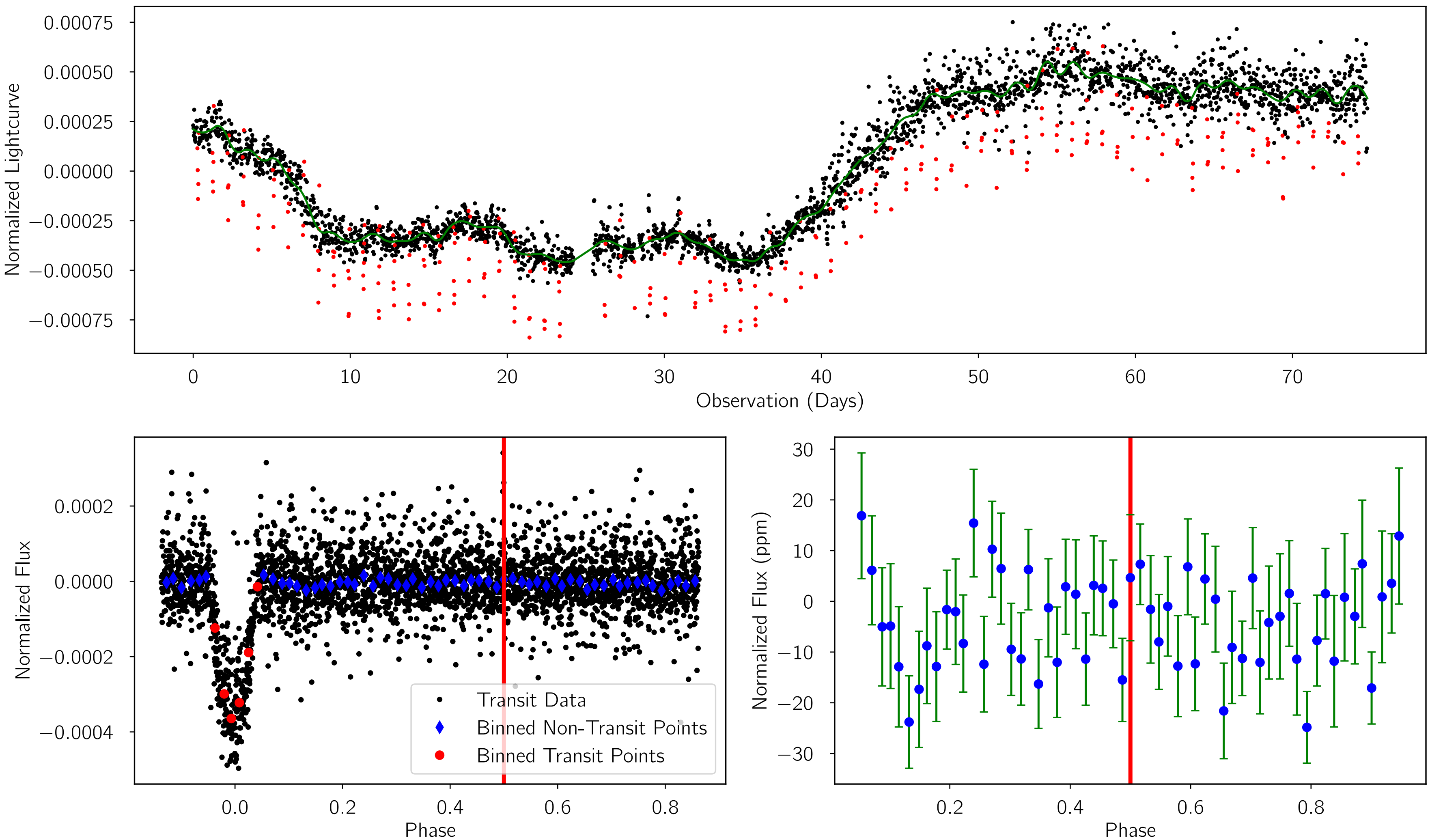

Figure 4.9: Spline fitting of the K2SFF detrended light curve of HD 3167 which is two planets, the inner with period of 0.95964 days. The top panel shows the flattening after rejecting the transit points marked in red. The lower left panel shows the phase folded light curve. The lower right panel shows the binned version after removing the transit. A vertical red line is drawn at the phase=0.5, where the secondary transit is expected to occur.

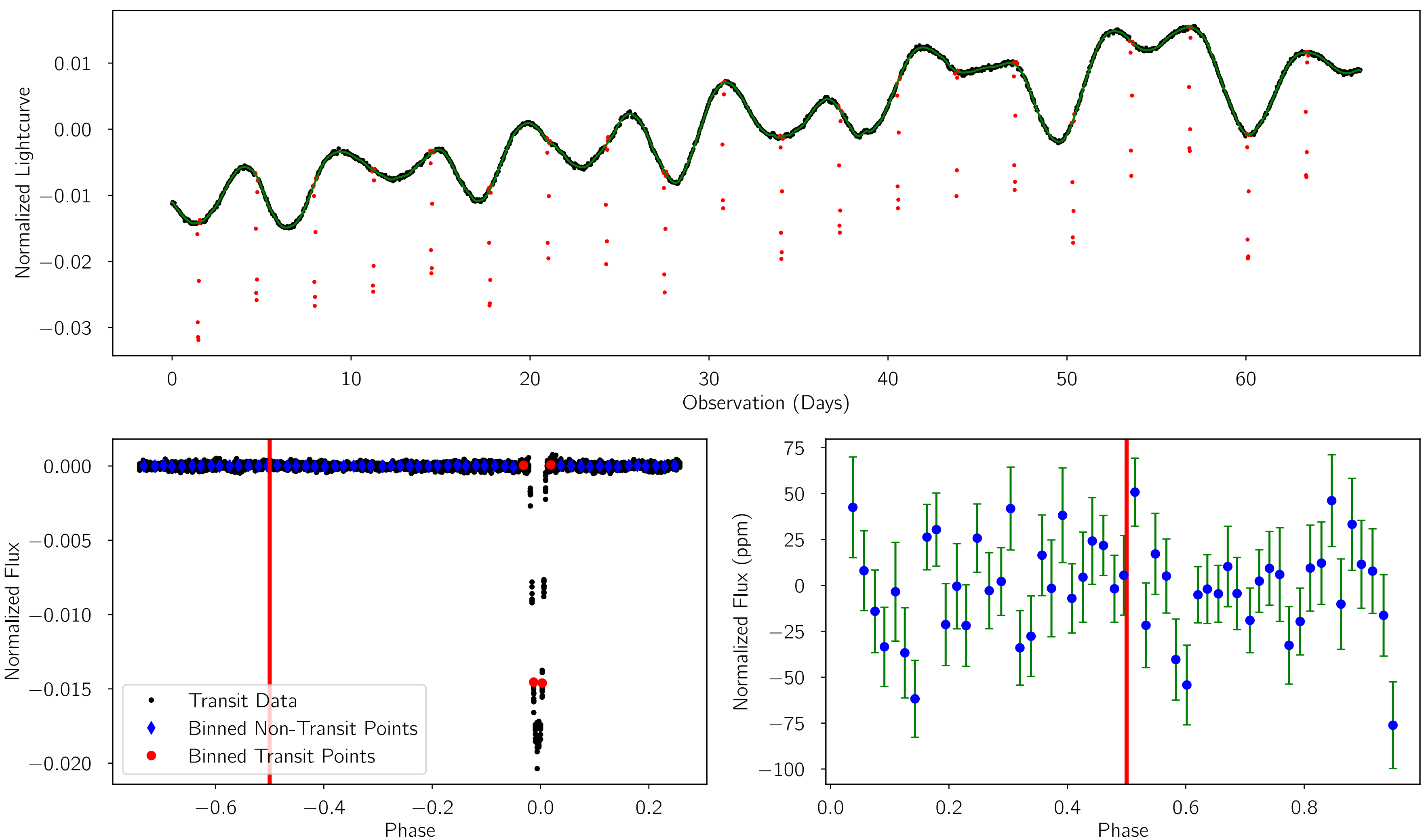

Figure 4.10: Spline fitting of the `K2SFF` detrended light curve of K2-29 which is a planet with period of 3.25883 days. The top panel shows the flattening after rejecting the transit points marked in red. The lower left panel shows the phase folded light curve. The lower right panel shows the binned version after removing the transit. A vertical red line is drawn at the phase=0.5, where the secondary transit is expected to occur.

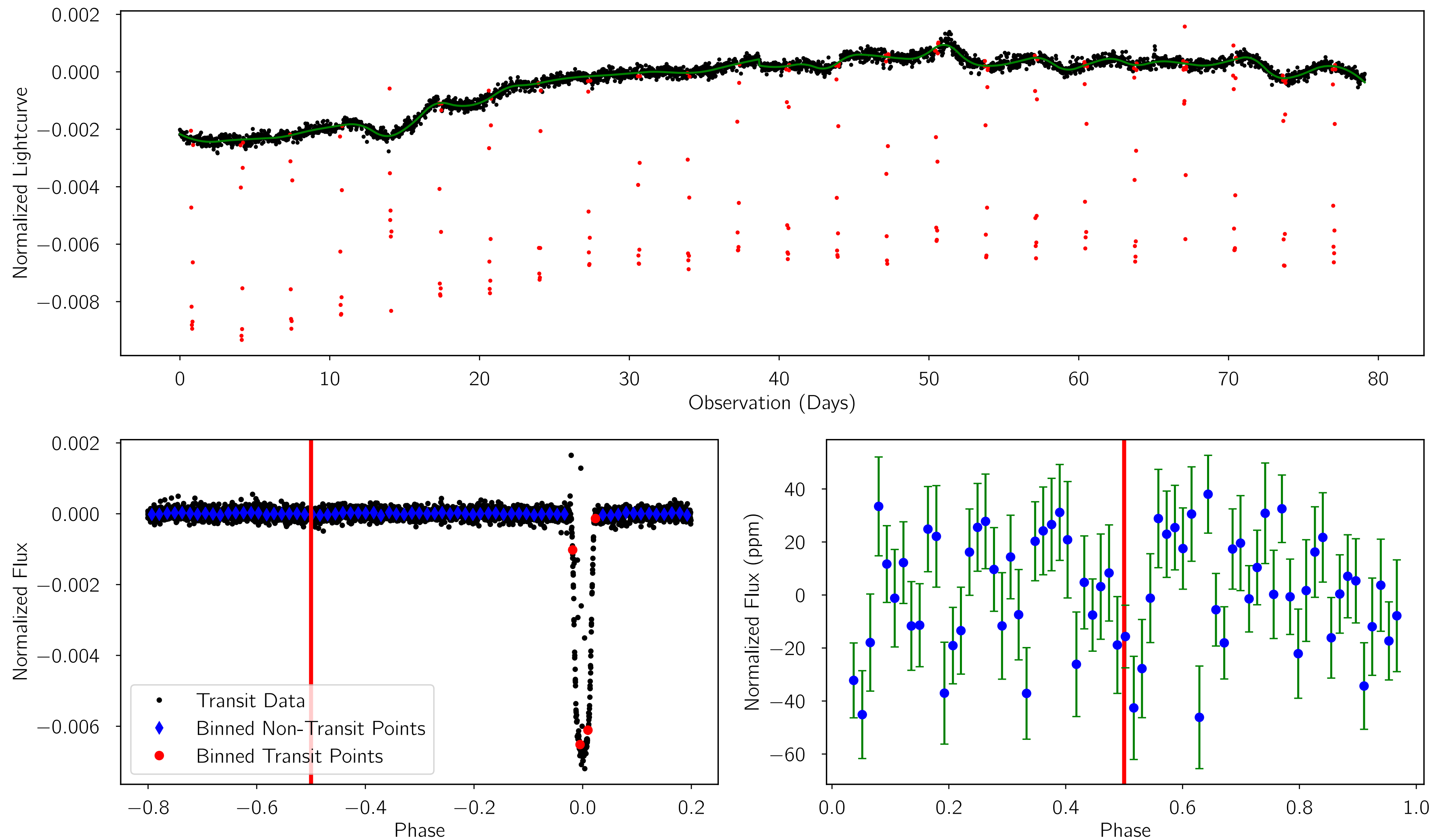

Figure 4.11: Spline fitting of the `K2SFF` detrended light curve of K2-107 which is a planet with period of 3.31392 days. The top panel shows the flattening after rejecting the transit points marked in red. The lower left panel shows the phase folded light curve. The lower right panel shows the binned version after removing the transit. A vertical red line is drawn at the phase=0.5, where the secondary transit is expected to occur.

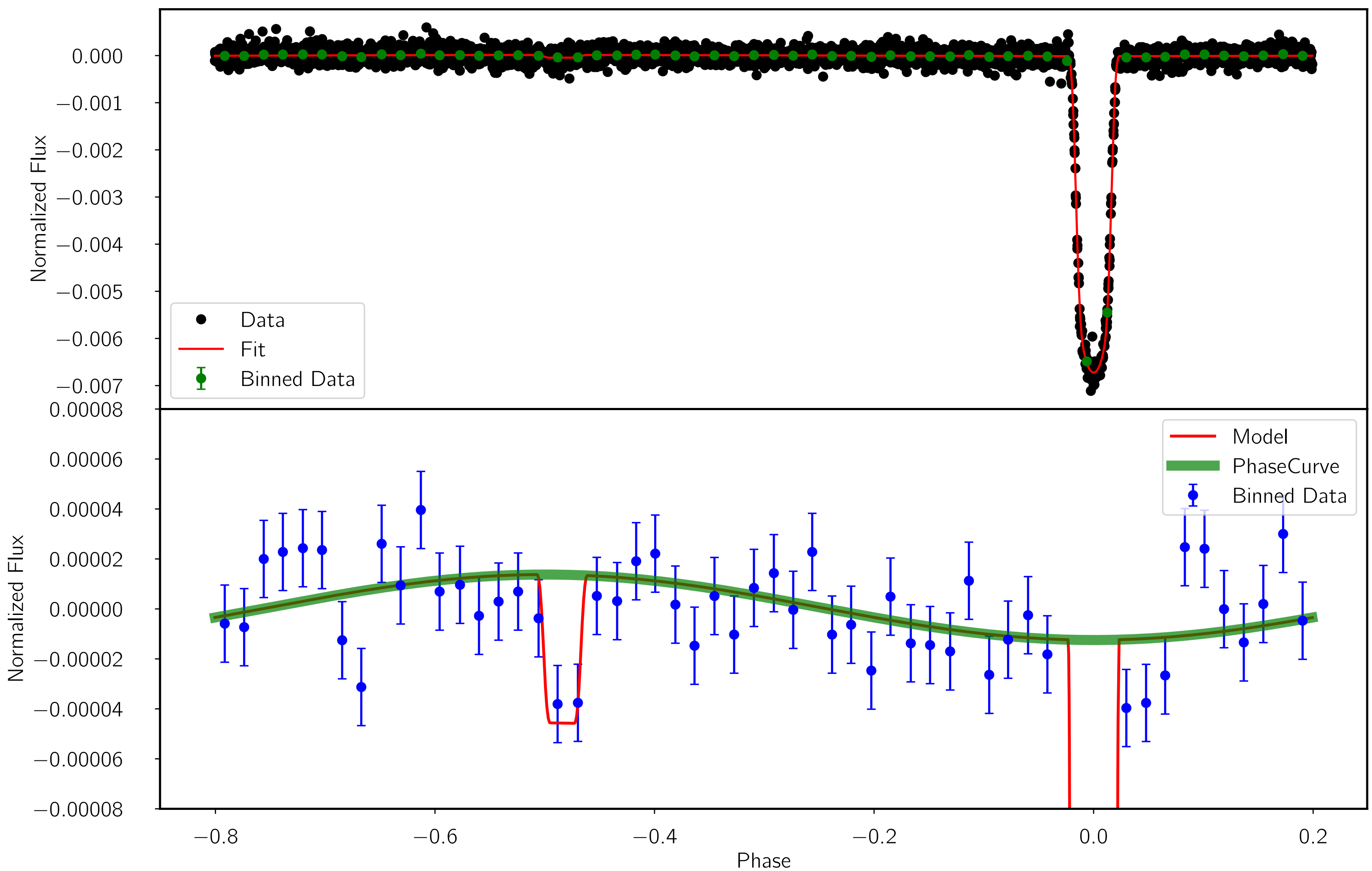

Figure 4.12: Fitting of K2 107 of both primary transit and the secondary transit using `batman`. The upper panel shows both the primary and secondary panel, and the lower right panel focuses on secondary eclipse as well as the phase curve.

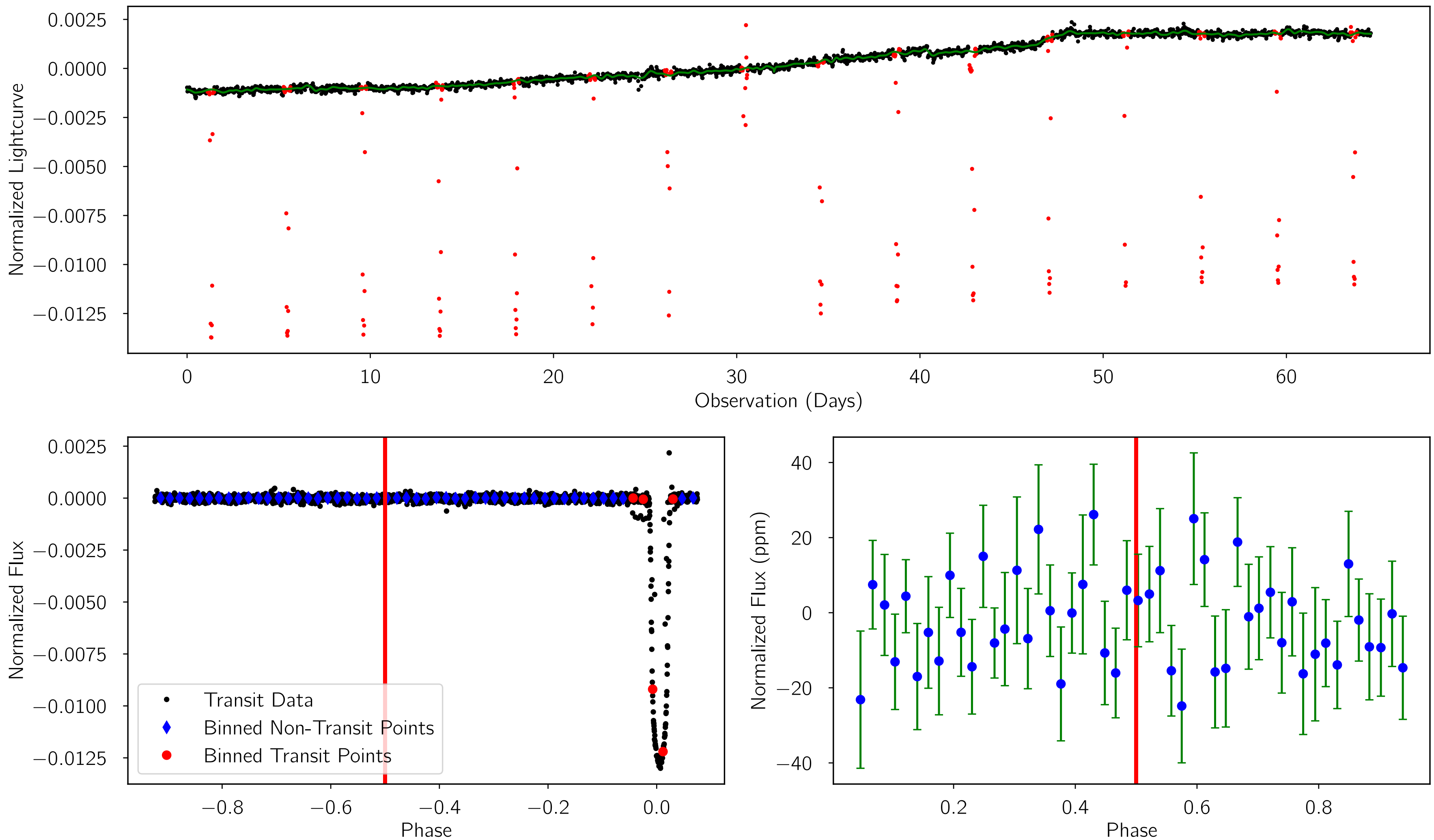

Figure 4.13: Spline fitting of the `K2SFF` detrended light curve of WASP-47 which is innermost planet with period of 4.16071 days. The top panel shows the flattening after rejecting the transit points marked in red. The lower left panel shows the phase folded light curve. The lower right panel shows the binned version after removing the transit. A vertical red line is drawn at the phase=0.5, where the secondary transit is expected to occur.

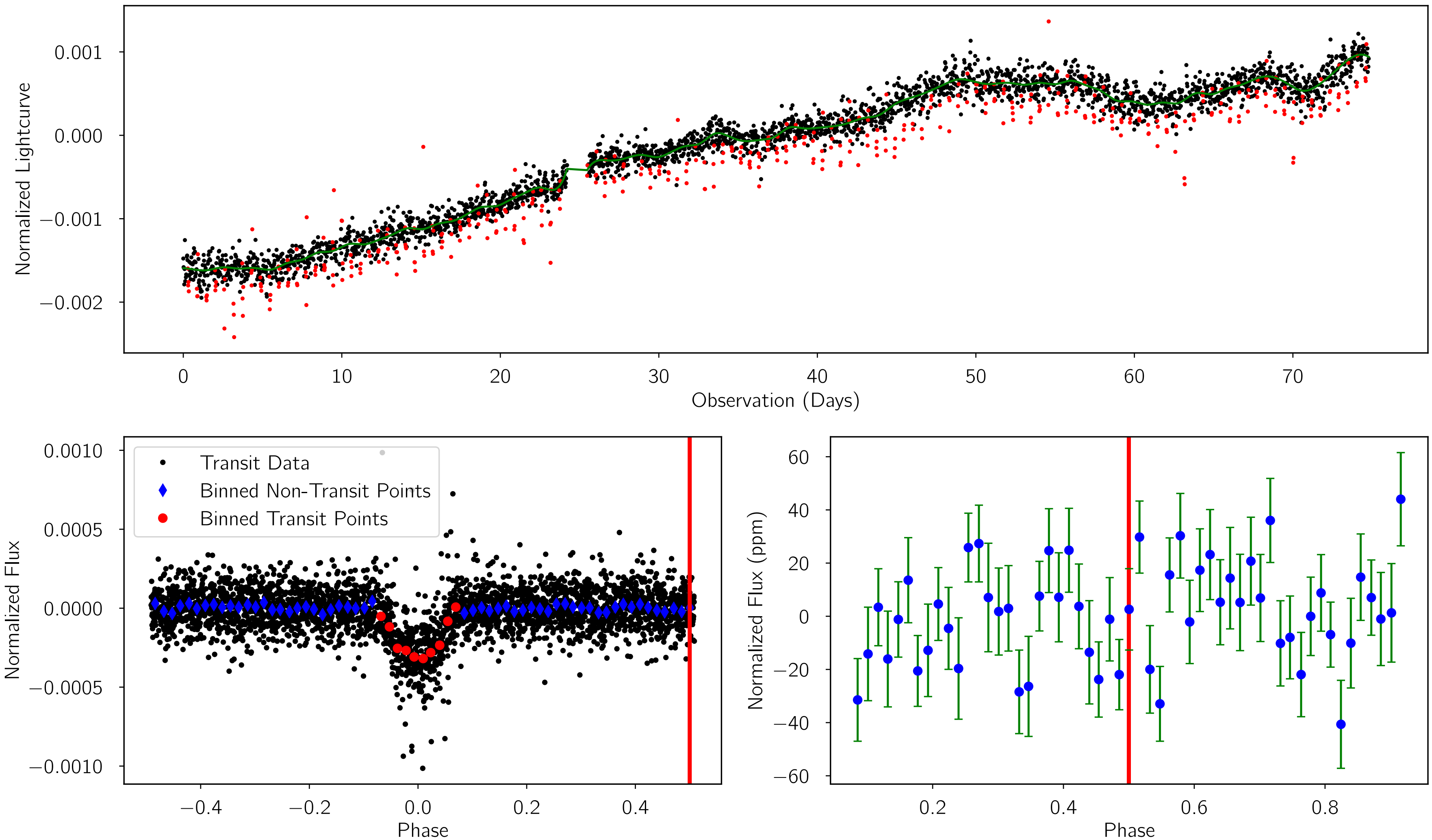

Figure 4.14: pline fitting of the `K2SFF` detrended light curve of K2-106 which is a planet with period of 0.57134 days. The top panel shows the flattening after rejecting the transit points marked in red. The lower left panel shows the phase folded light curve. The lower right panel shows the binned version after removing the transit. A vertical red line is drawn at the phase=0.5, where the secondary transit is expected to occur.

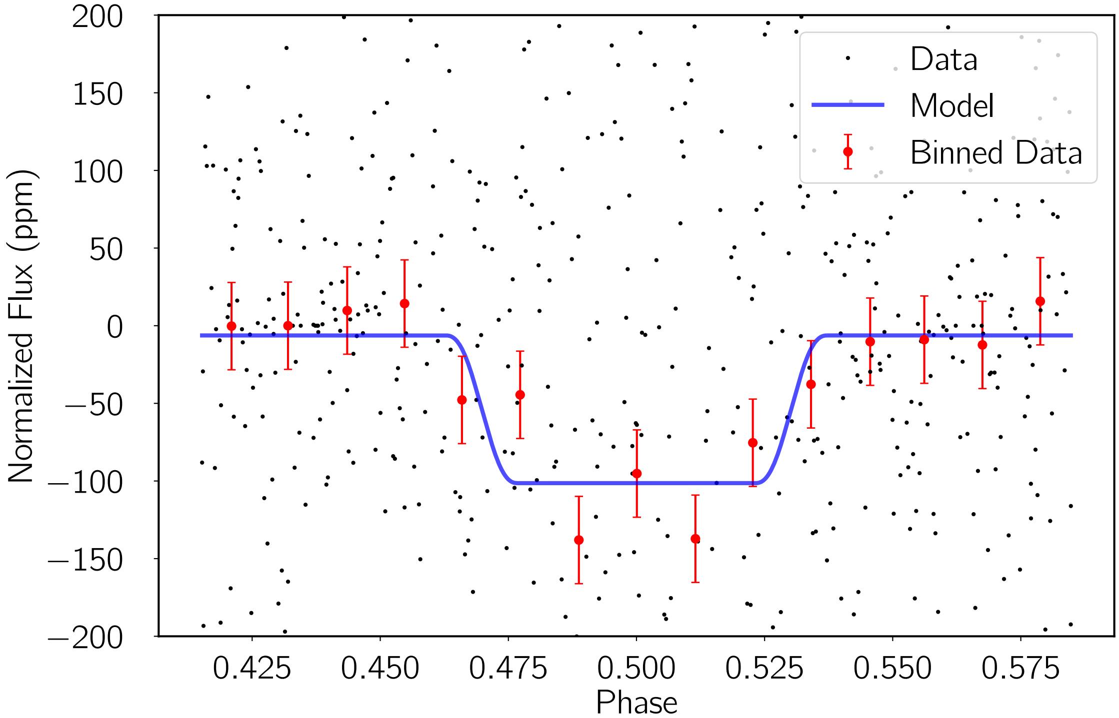

Figure 4.15: A secondary eclipse of 97 ± 7 ppm is observed in `everest` detrended light curve of hot jupiter EPIC 246911830 b.

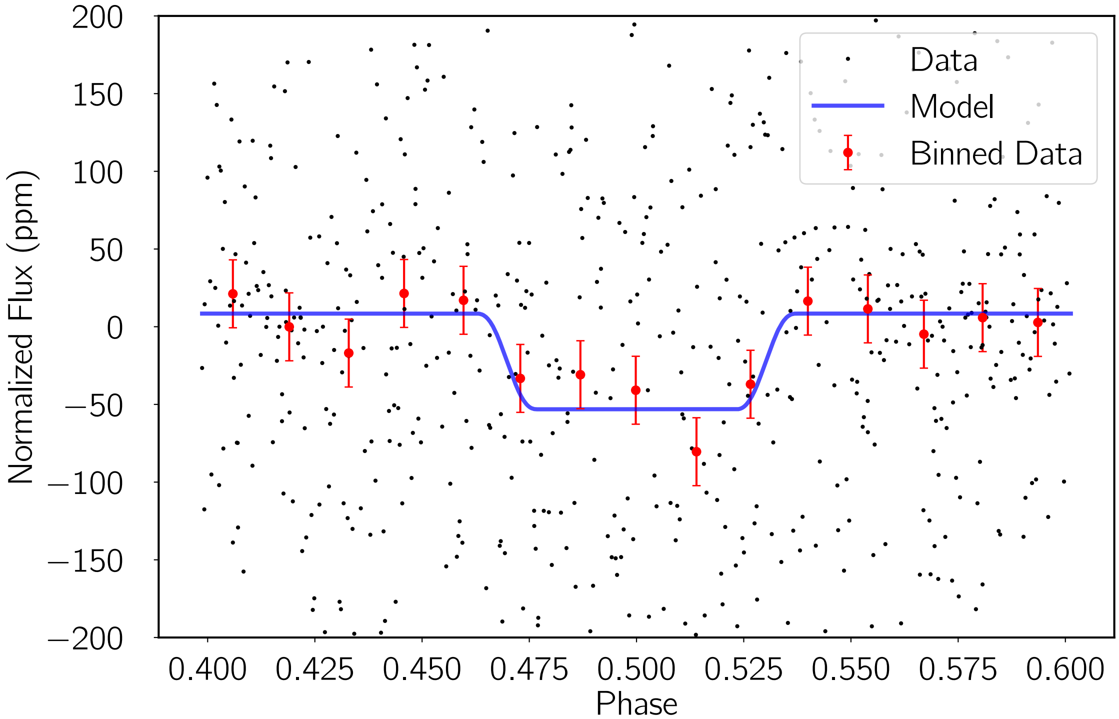

Figure 4.16: A secondary eclipse of 61 ± 7 ppm is observed in `K2SFF` detrended light curve of hot jupiter EPIC 246911830 b.

4.3.3 EPIC 246911830

Johnson et al. (2018) has submitted a paper on a new hot Jupiter reporting a secondary eclipse of depth 71 ± 15 ppm. Using the technique described in Huber et al. (2017), I obtain statistically significant secondary eclipse (see Figure 4.15 - 4.16). The secondary eclipse of 61 ± 7 ppm was obtained for `K2SFF` detrended light curve corresponding to A_g of 0.18 ± 0.02, whereas a secondary eclipse depth of 97 ± 7 pm was obtained from `everest` detrended light curve which corresponds to A_g of 0.29 ± 0.02. These two values are not consistent with one another, and shows how different detrending procedures can affect the final light curves obtained. Note that this planet is not catalogued in Table 4.1, and a K2 number has yet to be assigned as the paper is in the peer review process. Also, the stellar rotational period is found comparable with the orbital period of the planet, which makes it particularly difficult to disentangle the phase curve signal.

4.3.4 Other planets

For many of the planets catalogued in Table 4.1, no phase curve was observed. Since A_g =0.4 for geometric albedo is an optimistic assumption, we did not expect to see phase curves in many of the planetary candidates as the typical values for super-Earths, mini-Neptunes and super-Neptunes are respectively 0.11 ± 0.06, 0.05 ± 0.04, and 0.11 ± 0.08 (Sheets & Deming 2017). But for some, such as HAT-P-56, the light curve was found to be particularly noisy (see Figure 4.5), therefore lacking the precision required for the phase curve detection. This potentially was due to crowding near the source. In addition, my code has not been fully optimized to work in multi-planetary system for systems to handle planetary systems such as HD 3167 as well as WASP-47, which will be developed in the future. As for

K2-31 b, it does show the distinctive signature of ellipsoidal variation, however as this work began by considering only the reflective part, no further analysis is presented. Such work will be conducted in the future. This has demonstrated shown that even with *K2* considering additional optical phase components is not as a bad of an idea as originally thought.

4.4 Trojan Objects

Trojan objects are any celestial objects that have the same rotational period as does the planets around its host star. Looking for Trojan objects is not a new quest (see Janson 2013; Placek et al. 2015), and various techniques have already been proposed with photometry (Placek et al. 2015), RV (Ford & Gaudi 2006), as well as TTVs (Ford & Holman 2007). However, no Trojan objects have been discovered. In this work, I try to assess how feasible is the discovery of Trojan objects with *K2*.

For the presence of the Trojan objects, I consider the gravitational potential of two objects. In order to derive the points for L4 and L5 points consider a two-body configuration, whose center is arranged such that the center of mass lies in the origin. Let m_1 and m_2 be the mass of the two celestial objects, then for the co-rotation frame the Jacobi integral C is defined as the following:

$$\begin{aligned}
\mu &= \frac{M_2}{M_1 + M_2}, \\
r_1 &= \sqrt{(x+\mu)^2 + y^2)},\ r_2 = \sqrt{(x-1+\mu)^2 + y^2}, \\
r &= \sqrt{x^2 + y^2}, \\
W &= \frac{1}{2} r^2 + \frac{(1-\mu)}{r_1} + \frac{\mu}{r_2}, \\
C &= 2W.
\end{aligned} \tag{4.6}$$

where μ is the reduced mass of two bodies, x and y are the positions in the grids.

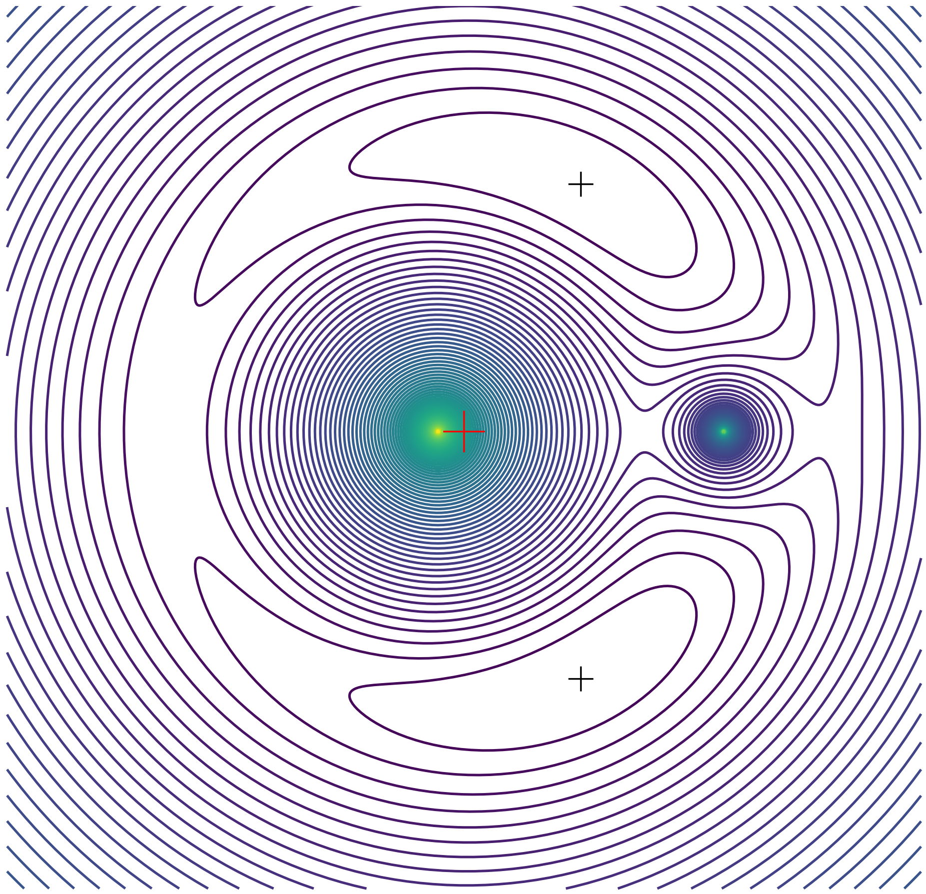

Figure 4.17: Lagrangian for two objects with mass ratio of 0.1. The center of mass is shown by the green cross hair at the center of the figure. The two black cross hair shows the exact location of L_4 and L_5 points. The contours represent the Jacobian integral from Equation 4.6.

I present the contour map for C in Figure 4.17. Note the phase by which the Trojan objects lead or follow the planet is the function of the mass ratio of the two bodies (see Figure 4.18). Even though, the objects can be stable over the time scale of giga-years as has been the case in Trojan asteroids in the Sun-Jupiter system, the stability can only be achieved when certain criteria are met.

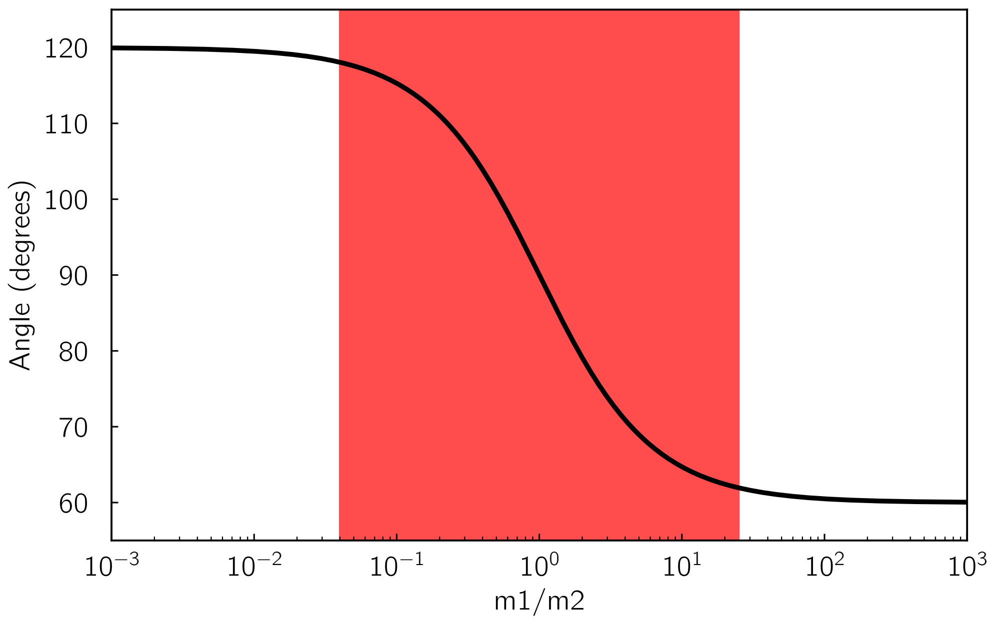

Figure 4.18: The L4 and L5 points in a two body system will occur 60° before or after the transit when the mass of the primary is dominant. However, as the secondary body has mass approaching the mass of the primary object, the L4 and L5 points occur at 90° as is shown in the figure. However, when the secondary body is around 0.04 times the mass of the primary, the orbits of the Trojan objects become unstable.

For instance, in 1843 Gascheau showed that Trojans objects are linearly held in equilibria until:

$$\frac{M_P M_T + M_T M_* + M_P M_*}{(M_T + M_P + M_*)^2} < \frac{1}{27} \tag{4.7}$$

This shows that for $M_p > 0.04 M_*$, the Trojans are not stable, which I was able to numerically verify using simulations in `rebound`.

4.4.1 Libration

In our numerical simulation, I found that Trojan objects can be stably captured at L4 and L5 even while librating with a phase amplitude of 0.03. The libration is caused by the interaction between the planetary object and the Tro-

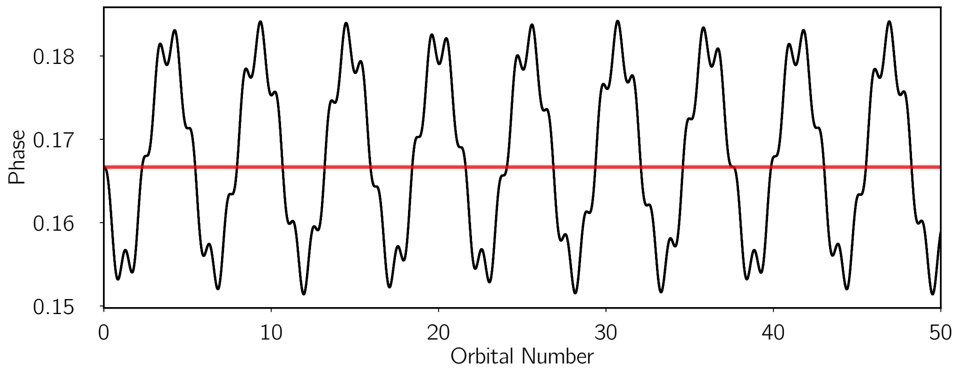

Figure 4.19: Libration of Trojan object around L4 points for 1 $M_\odot$ star and 0.001 $M_\odot$ planet.

jans, thus larger the mass of the primary object larger the libration. This further complicates the detection of Trojan objects as any libration dilutes the transit signals, which is already a challenge because the Trojan objects are expected to be much smaller than the planets, and therefore generate much smaller signals. Additionally, Trojan objects can librate with even larger amplitude depending on how they were captured in the first place.

As demonstrated in this chapter, with proper detrending applied *K2* is capable of detecting the phase curves of the close-in hot Jupiters. However, finding Trojan object poses an even bigger challenge as it requires precision of about 1–2 ppm (Hippke & Angerhausen 2015). Such depth is shallower than the precision that *K2* is able to offer, but might be possible for planets in short orbital periods such as HAT-P-7b system in the original *Kepler* mission after phase folding. Note that the Trojan objects does not necessarily have to be small objects like in our solar system, but anything with a substantial mass in a co-orbital radius will induce transit timing variation, which is much readily detectable. Given all these complications, looking for Trojan objects in the original *Kepler* is the best bet for finding them, and if successful, only then should be tried with *K2*.

Chapter 5

Conclusion

In writing this thesis, I hope to have shown how precision photometry has been a game changer in the field of exoplanets. With *K2*, the legacy of *Kepler* as the discoverer of smaller planets continues. In fact, currently *K2* is the only operational facility that is capable of making discoveries of small planetary system such as GJ 9827. At the same time by observing targets beyond its classical regime, *K2* has shown how precision photometry can be beneficial for different divisions of astronomy such as asteroseismology, Active Galactic Nuclei or galactic astronomy. While *Kepler*'s four yearlong photometric coverage will probably be unmatched for its precision, length and coverage for some decades to come, *K2* expansion of the scope of precision photometry has irreversibly changed the field of astronomy.

5.1 Comparative Phase Curve

The launch of *TESS*, an instrument with comparable photometric capability to *Kepler* but working in different bandpass, will provide an interesting opportunity to re-observe many of the planets discovered and studied by *Kepler*. Since their bandpasses are different, it will allow us to see how the radius of the planet changes with wavelength, and therefore will provide some preliminary indication of the presence of the atmosphere. For hot Jupiters, if the phase curves are observable, the reflective component and the thermal component can be disentangled from these two different photometric time series as has been described in Placek et al. (2016), thereby opening new avenues of research. However, *TESS* will not be observing the ecliptic, which means only for targets observed by *Kepler* would such study be possible. But there is a plethora of interesting targets such as HAT-P-7b, and multiple *Kepler* discovered planets which will provide a broad ground for such studies.

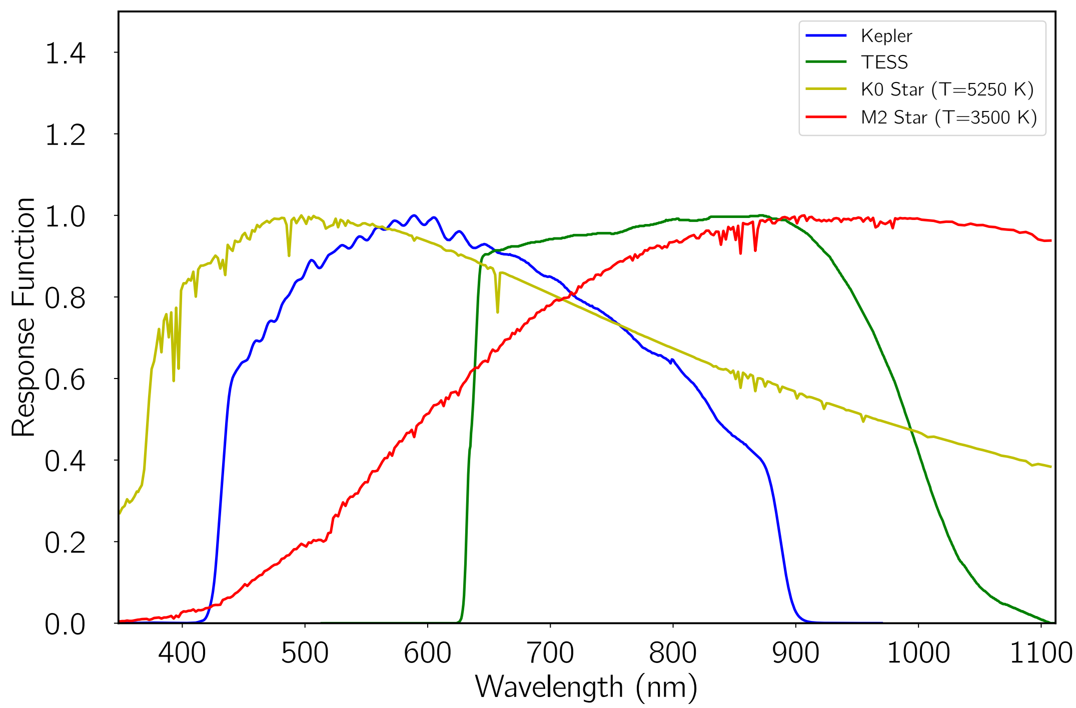

Figure 5.1: Function showing different along with spectral of different spectral type star. The *TESS* response function was kindly provided by Prof. Ben Placek, Wentworth Insititute of Technology.

Currently, atmospheric clouds pose a major challenge in characterizing the atmosphere of some of the most promising candidates such as GJ 1214 b (Kreidberg et al. 2014). A comparative phase curve and photometry could be particularly helpful in finding out if the targets are as good as expected for atmospheric characterization follow-up. And with *JWST* launch on the horizon, the field of exoplanet characterization is likely to make progress in leaps and bounds, particularly in making definitive progress towards studying the atmospheric composition, as well as providing better quality data to test our models of the atmospheres.

5.2 Future Work

K2 will likely continue for a few more campaigns, and its gamble for observing bright targets seems to be paying off. As recent as Campaign 16, there was a super-Earth sized planetary candidate around a bright target HD 73344 with $V = 6.9$ (Yu et al. 2018). If confirmed, this would be among the brightest target to have a planetary candidate, therefore great for atmospheric characterization follow-up. Besides, more campaigns are planned, which will keep the stream of discoveries of planets flowing. But, *K2* will likely run out of fuel before or during Campaign 19, which would conclude one of the most prolific missions for exoplanet discovery. But this would mean we are still anticipating new data to analyze, and continue our hunt for planets.

Besides, the *K2* data set is likely to hold many interesting targets which will be discovered as the data will be progressively combed with more optimized data processing techniques. One such avenue would be to look for serendipitously captured targets in the frame of the bright stars as was described in Chapter 2. I intend to carry on this work during this summer. So far, I have only looked into a subset of serendipitously observed targets in a smaller subset, and looking into a larger dataset is likely to yield some interesting targets. In fact, in the smaller data set, I have already found a few interesting targets which I have not reported in this work. And some of the major challenges for such a study include finding the suitable aperture to extract the photometric data, which ties into the traditional data challenges.

Additionally, the phase curve for K3-31 (see Figure 4.3) was an unexpected last minute find, and calculation using the planet-star parameters tells that the observed ellipsoidal variation of about 50 ppm which is higher than from expected ellipsoidal variation of amplitude 12 ppm (i.e. peak to peak value of 24 ppm), the discrepancy can be explained away with reflective as well as Doppler beaming effects. A similar phase curve was shown to be present for Qatar-2b in Dai et al. (2017) as shown in Figure 5.2. In our future work, we will be looking to answer

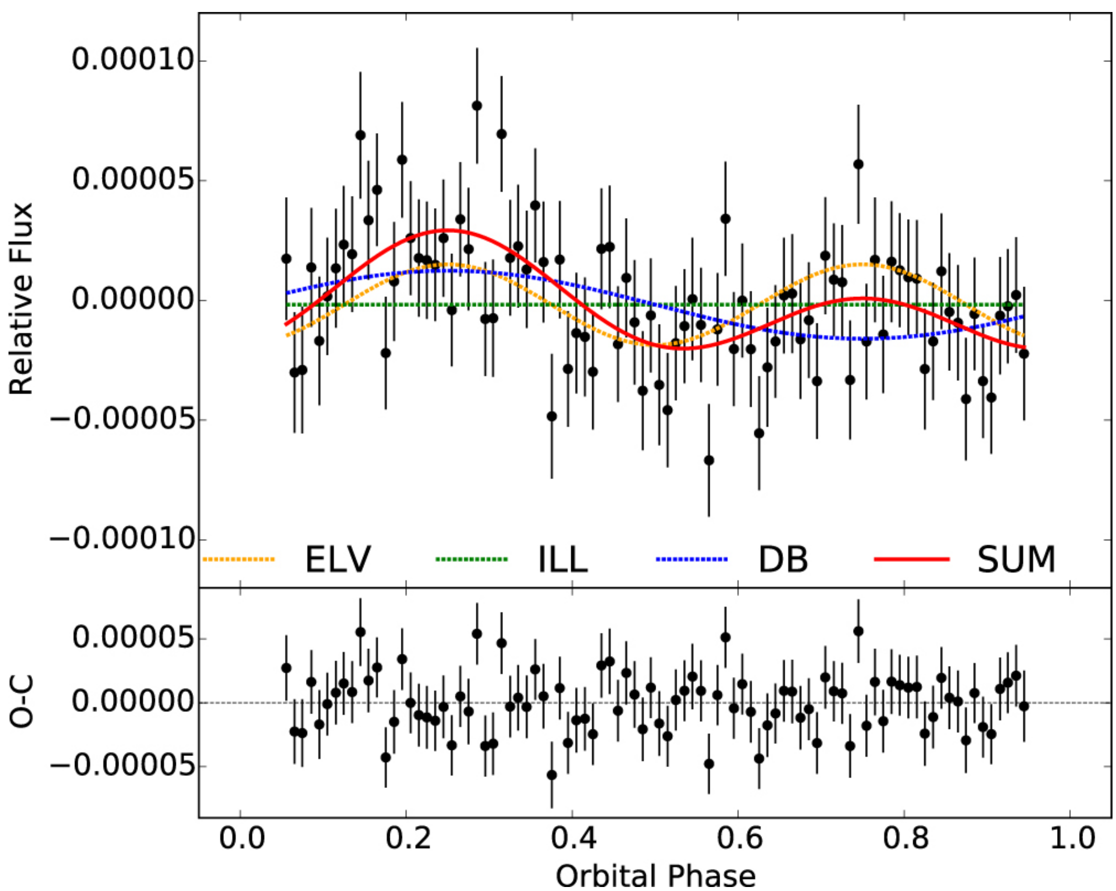

Figure 5.2: Combination of ellipsoidal variation (ELV) and Doppler beaming (DB) seen in Qatar-2b in *K2* light curve as reported in Dai et al. (2017).

if any additional steps in detrending would allow to better preserve the fidelity of the phase curve signal. Also, once the phase curve pipeline is ironed out, it could potentially be used to validate some of the planetary candidates as has been done in the past (Mislis & Hodgkin 2012). For this line of research, we will be particularly looking for the ellipsoidal variation among the planetary candidates, from which we intend get a rough estimate on the mass.

All of this effort in finding more planets ultimately ties into more fundamental questions about the occurrence rates of the planets, and their size distribution, which in turn helps to address even more fundamental questions about their origins. In fact, looking into the current data set already some of the interesting patterns have emerged. For instance, a gap known as Fulton gap in the planet size distribution as shown in Figure 5.3 is reported. This is already a major improvement on what was reported a few year ago (see Figure 1.5). Similarly, the relationship between the metallicity of the host star and the planet occurrence rates that was discussed by Fischer & Valenti (2005) are being revisited with studies such as Petigura et al. (2017), which in turn has shown the relationship is strongest for hot Jupiters, and not as much as was expected for other categories of exoplanets. These are examples of how our findings of more planets will facilitate answering some of the deeper questions in the field of exoplanets.

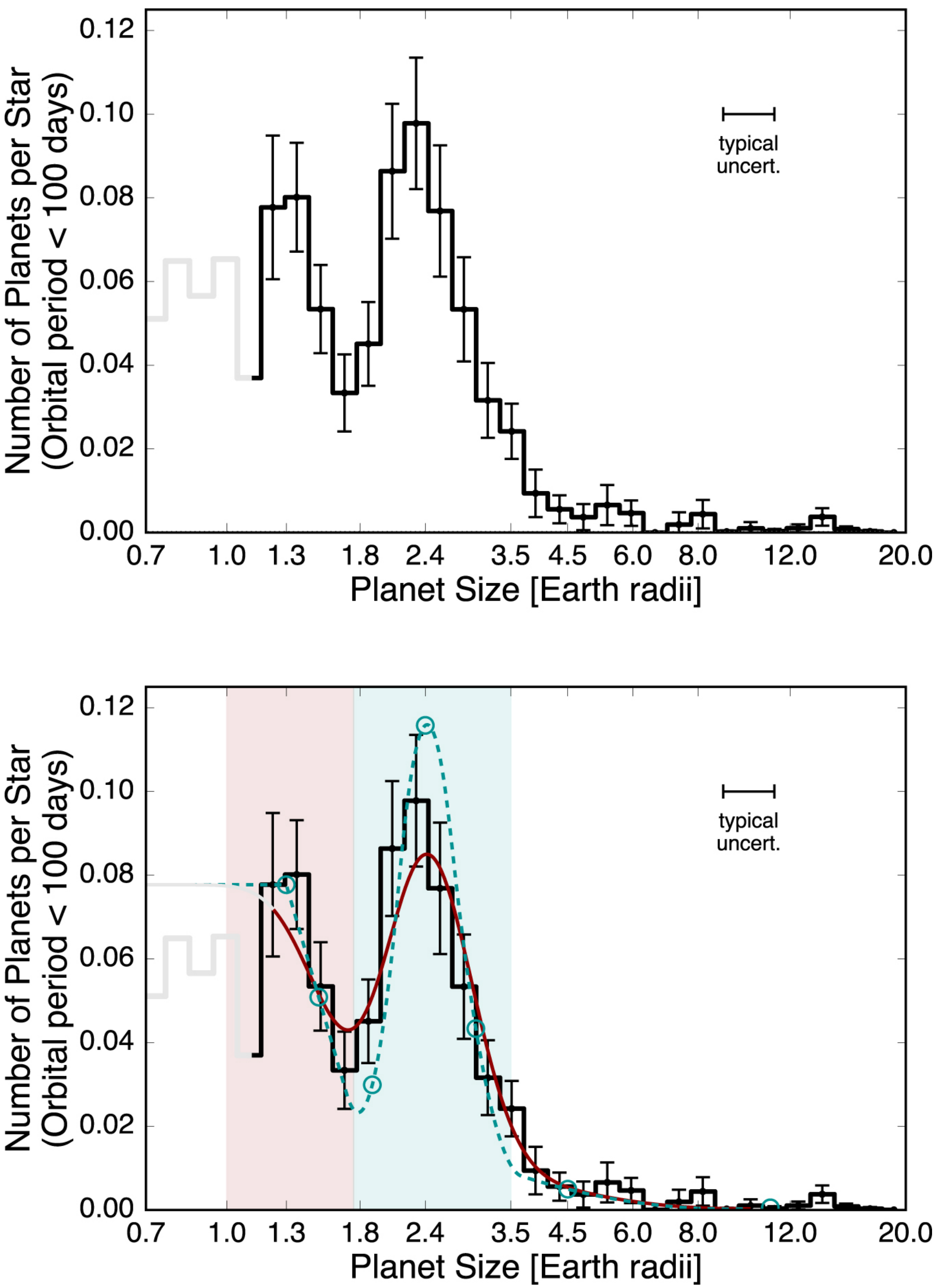

Figure 5.3: An interesting gap (called Fulton's gap) is seen in the planet's occurrence rate vs their size commonly around $1.8 R_{\oplus}$ as seen in the figure above adopted from Fulton as seen in Fulton et al. (2017).

5.3 Prospects of the field

We have seen rapid progress in different fronts of the planetary science. For instance, in the solar system exploration, the recent visits to the moons of giant planets as well as asteroids have garnered a wealth of information. The recent *Juno* mission, which is mapping Jupiter with an unprecedented detail, has led into interesting insights into Jupiter's atmosphere. For instance, cyclonic activities at the poles of Jupiter were seen (Kaspi et al. 2018; Adriani et al. 2018) which showed atmosphere of Jupiters are more complex than expected. We have been modeling the atmosphere of hot-Jupiters for more than a decade now with some success, and such new observations within our solar system will definitely assist modelers to refine the atmospheric models of the hot Jupiters.

At the same time the field of planetary formation has taken a leap of its own with the recent developments of new radio tools such as Atacama Large Millimeter/submillimeter Array (*ALMA*) (ALMA Partnership et al. 2015). ALMA has been a game changer, as for the first time we are finding the gaps in the proto-planetary disks (Andrews et al. 2016) and learning in great detail about the evolution of the disk into the planets (Hughes et al. 2018). Thus, there has been progress in answering the puzzles of the planetary science at different stages. The easier ones will act as a stepping stone towards finding solutions of the harder ones.

Exoplanet research as a young field and growing at an accelerating pace. In the next two to three decades, it will very likely have even bigger breakthroughs. The majority of this will come as different tools are developed, or as technological innovation will allow to probe things that previously were impossible or simply not imagined about. As the saying goes, a rising tide raises all boats, the progress made in different branches in science as well as technology will impact the field of exoplanets by facilitating more in-depth research. The universe is a big jigsaw puzzle, and as more pieces fall in their right location, it will become easier to narrate the story.

Bibliography

Abbot, D. S., & Switzer, E. R. 2011, *ApJL*, 735, L27

Adriani, A., et al. 2018, *Nature*, 555, 216

Agol, E., & Fabrycky, D. C. 2017, Transit-Timing and Duration Variations for the Discovery and Characterization of Exoplanets, 7

Agol, E., Steffen, J., Sari, R., & Clarkson, W. 2005, *MNRAS*, 359, 567

Aigrain, S., Parviainen, H., & Pope, B. J. S. 2016, *MNRAS*, 459, 2408

ALMA Partnership et al. 2015, *ApJL*, 808, L3

Alvarado-Gómez, J. D., Hussain, G. A. J., Cohen, O., Drake, J. J., Garraffo, C., Grunhut, J., & Gombosi, T. I. 2016, *A&A*, 594, A95

Andrews, S. M., et al. 2016, *ApJL*, 820, L40

Angerhausen, D., DeLarme, E., & Morse, J. A. 2015, *PASP*, 127, 1113

Anglada, G., et al. 2017, *ApJL*, 850, L6

Anglada-Escudé, G., et al. 2016, *Nature*, 536, 437

Aranzana, E., Körding, E., Uttley, P., Scaringi, S., & Bloemen, S. 2018, *MNRAS*, 476, 2501

Armstrong, D. J., de Mooij, E., Barstow, J., Osborn, H. P., Blake, J., & Saniee, N. F. 2016, Nature Astronomy, 1, 0004

Barragán, O., Gandolfi, D., & Antoniciello, G. 2017a, pyaneti: Multi-planet radial velocity and transit fitting, Astrophysics Source Code Library

Barragán, O., et al. 2017b, ArXiv e-prints

Batalha, N. M., et al. 2013, *ApJS*, 204, 24

Beichman, C., et al. 2014, *PASP*, 126, 1134

Black, D. C. 1980, *SSRv*, 25, 35

Bordé, P., Rouan, D., & Léger, A. 2003, *A&A*, 405, 1137

Borucki, W., et al. 2008, in IAU Symposium, Vol. 249, Exoplanets: Detection, Formation and Dynamics, ed. Y.-S. Sun, S. Ferraz-Mello, & J.-L. Zhou, 17–24

Borucki, W. J., et al. 2010, Science, 327, 977

—. 2009, Science, 325, 709

Brahm, R., et al. 2016, *PASP*, 128, 124402

Broeg, C., et al. 2013, in European Physical Journal Web of Conferences, Vol. 47, European Physical Journal Web of Conferences, 03005

Bryan, M. L., et al. 2016, *ApJ*, 821, 89

Cabrera, J., et al. 2017, *A&A*, 606, A75

Carter, J. A., et al. 2012, Science, 337, 556

Cauley, P. W., Redfield, S., & Jensen, A. G. 2017, *AJ*, 153, 217

Charbonneau, D., Brown, T. M., Noyes, R. W., & Gilliland, R. L. 2002, *ApJ*, 568, 377

Christiansen, J. L., et al. 2018, *AJ*, 155, 57

Cowan, N. B., et al. 2015, *PASP*, 127, 311

Crossfield, I. J. M., et al. 2016, *ApJS*, 226, 7

Cuntz, M., & Guinan, E. F. 2016, *ApJ*, 827, 79

Cutri, R. M., et al. 2003, VizieR Online Data Catalog, 2246

Dai, F., & Winn, J. N. 2017, *AJ*, 153, 205

Dai, F., Winn, J. N., Yu, L., & Albrecht, S. 2017, *AJ*, 153, 40

Delorme, P., et al. 2017, *A&A*, 602, A82

Deming, D., et al. 2015, *ApJ*, 805, 132

—. 2009, *PASP*, 121, 952

Demory, B.-O. 2014, *ApJL*, 789, L20

Demory, B.-O., et al. 2016, *Nature*, 532, 207

Dressing, C. D., et al. 2017, *AJ*, 154, 207

Eigmüller, P., et al. 2017, *AJ*, 153, 130

Esteves, L. J., De Mooij, E. J. W., & Jayawardhana, R. 2013, *ApJ*, 772, 51

—. 2015, *ApJ*, 804, 150

Fabrycky, D. C., et al. 2014, *ApJ*, 790, 146

Faigler, S., Tal-Or, L., Mazeh, T., Latham, D. W., & Buchhave, L. A. 2013, *ApJ*, 771, 26

Fischer, D. A., & Valenti, J. 2005, *ApJ*, 622, 1102

Ford, E. B., & Gaudi, B. S. 2006, *ApJL*, 652, L137

Ford, E. B., & Holman, M. J. 2007, *ApJL*, 664, L51

Foreman-Mackey, D., Hogg, D. W., Lang, D., & Goodman, J. 2013, *PASP*, 125, 306

Foreman-Mackey, D., Montet, B. T., Hogg, D. W., Morton, T. D., Wang, D., & Schölkopf, B. 2015, *ApJ*, 806, 215

Foreman-Mackey, D., Morton, T. D., Hogg, D. W., Agol, E., & Schölkopf, B. 2016, *AJ*, 152, 206

Fressin, F., et al. 2013, *ApJ*, 766, 81

Fridlund, M., et al. 2017, *A&A*, 604, A16

Fujii, Y., et al. 2017, ArXiv e-prints

Fulton, B. J., et al. 2017, *AJ*, 154, 109

Gandolfi, D., et al. 2017, *AJ*, 154, 123

Gillon, M., et al. 2016, *Nature*, 533, 221

Harrington, J., Hansen, B. M., Luszcz, S. H., Seager, S., Deming, D., Menou, K., Cho, J. Y.-K., & Richardson, L. J. 2006, Science, 314, 623

Hébrard, É. M., Donati, J.-F., Delfosse, X., Morin, J., Moutou, C., & Boisse, I. 2016, *MNRAS*, 461, 1465

Heller, R. 2018, *A&A*, 610, A39

Hippke, M., & Angerhausen, D. 2015, *ApJ*, 811, 1

Hirano, T., et al. 2016, *ApJ*, 825, 53

Houdebine, E. R., Mullan, D. J., Paletou, F., & Gebran, M. 2016, *ApJ*, 822, 97

Howell, S. B., et al. 2014, *PASP*, 126, 398

Huang, C. X., Penev, K., Hartman, J. D., Bakos, G. Á., Bhatti, W., Domsa, I., & de Val-Borro, M. 2015, *MNRAS*, 454, 4159

Huber, K. F., Czesla, S., & Schmitt, J. H. M. M. 2017, *A&A*, 597, A113

Hughes, A. M., Duchene, G., & Matthews, B. 2018, ArXiv e-prints

Janson, M. 2013, *ApJ*, 774, 156

Jódar, E., Pérez-Garrido, A., Díaz-Sánchez, A., Villó, I., Rebolo, R., & Pérez-Prieto, J. A. 2013, *MNRAS*, 429, 859

Johnson, M. C., et al. 2018, *MNRAS*

Kaltenegger, L., Traub, W. A., & Jucks, K. W. 2007, *ApJ*, 658, 598

Kaspi, Y., et al. 2018, *Nature*, 555, 223

Kempton, E. M.-R., Lupu, R., Owusu-Asare, A., Slough, P., & Cale, B. 2017, *PASP*, 129, 044402

Kipping, D. 2017, *AJ*, 153, 277

Kipping, D. M. 2010, *MNRAS*, 408, 1758

—. 2013, *MNRAS*, 435, 2152

Knutson, H. A., Charbonneau, D., Allen, L. E., Burrows, A., & Megeath, S. T. 2008, *ApJ*, 673, 526

Knutson, H. A., et al. 2007, *Nature*, 447, 183

Kovács, G., Zucker, S., & Mazeh, T. 2002, *A&A*, 391, 369

Kreidberg, L. 2015, *PASP*, 127, 1161

Kreidberg, L., et al. 2014, *Nature*, 505, 69

Libralato, M., Bedin, L. R., Nardiello, D., & Piotto, G. 2016, *MNRAS*, 456, 1137

Lillo-Box, J., et al. 2016, *A&A*, 594, A50

Lindegren, L., & Perryman, M. A. C. 1996, *A&AS*, 116, 579

Linsky, J. L., Fontenla, J., & France, K. 2014, *ApJ*, 780, 61

Lissauer, J. J., et al. 2012, *ApJ*, 750, 112

Lovis, C., & Fischer, D. A. 2011, in Exoplanets, ed. S. Seager (Tuscon, AZ: The University of Arizona Press)

Lubin, P. 2016, ArXiv e-prints

Luger, R., Agol, E., Kruse, E., Barnes, R., Becker, A., Foreman-Mackey, D., & Deming, D. 2016, *AJ*, 152, 100

Luger, R., et al. 2017, Nature Astronomy, 1, 0129

Lund, M. N., Handberg, R., Davies, G. R., Chaplin, W. J., & Jones, C. D. 2015, *ApJ*, 806, 30

Lund, M. N., et al. 2017, *ApJ*, 835, 172

MacGregor, M. A., Weinberger, A. J., Wilner, D. J., Kowalski, A. F., & Cranmer, S. R. 2018, *ApJL*, 855, L2

Malavolta, L., et al. 2018, *AJ*, 155, 107

Mann, A. W., Feiden, G. A., Gaidos, E., Boyajian, T., & von Braun, K. 2015, *ApJ*, 804, 64

Marcy, G. W., & Butler, R. P. 1995, in Bulletin of the American Astronomical Society, Vol. 27, American Astronomical Society Meeting Abstracts, 1379

Mayo, A. W., et al. 2018, *AJ*, 155, 136

Mayor, M., & Queloz, D. 1995, *Nature*, 378, 355

McQuillan, A., Aigrain, S., & Mazeh, T. 2013, *MNRAS*, 432, 1203

Meadows, V., & Seager, S. 2010, Terrestrial Planet Atmospheres and Biosignatures, ed. S. Seager, 441–470

Miller-Ricci, E., Seager, S., & Sasselov, D. 2009, *ApJ*, 690, 1056

Millholland, S., & Laughlin, G. 2017, *AJ*, 154, 83

Mislis, D., & Hodgkin, S. 2012, *MNRAS*, 422, 1512

Morton, T. D., Bryson, S. T., Coughlin, J. L., Rowe, J. F., Ravichandran, G., Petigura, E. A., Haas, M. R., & Batalha, N. M. 2016, *ApJ*, 822, 86

Močnik, T., et al. 2016, *PASP*, 128, 124403

Močnik, T., Hellier, C., Anderson, D. R., Clark, B. J. M., & Southworth, J. 2017, *MNRAS*, 469, 1622

Murray, C. D., & Dermott, S. F. 1999, Solar system dynamics

Mustill, A. J., & Wyatt, M. C. 2011, *MNRAS*, 413, 554

Nardiello, D., Libralato, M., Bedin, L. R., Piotto, G., Borsato, L., Granata, V., Malavolta, L., & Nascimbeni, V. 2016, *MNRAS*, 463, 1831

Niraula, P., et al. 2017, *AJ*, 154, 266

Öberg, K. I., Murray-Clay, R., & Bergin, E. A. 2011, *ApJL*, 743, L16

Obermeier, C., et al. 2016, *AJ*, 152, 223

Owen, T., Mahaffy, P., Niemann, H. B., Atreya, S., Donahue, T., Bar-Nun, A., & de Pater, I. 1999, *Nature*, 402, 269

Pál, A., et al. 2008, *ApJ*, 680, 1450

Perryman, M., Hartman, J., Bakos, G. Á., & Lindegren, L. 2014, *ApJ*, 797, 14

Petigura, E. A., et al. 2017, *AJ*, 154, 107

Placek, B., Knuth, K. H., & Angerhausen, D. 2016, *PASP*, 128, 074503

Placek, B., Knuth, K. H., Angerhausen, D., & Jenkins, J. M. 2015, *ApJ*, 814, 147

Prieto-Arranz, J., et al. 2018, ArXiv e-prints

Puig, L., Pilbratt, G. L., Heske, A., Escudero Sanz, I., & Crouzet, P.-E. 2016, in Proc. SPIE, Vol. 9904, Space Telescopes and Instrumentation 2016: Optical, Infrared, and Millimeter Wave, 99041W

Rauer, H., et al. 2014a, Experimental Astronomy, 38, 249

—. 2014b, Experimental Astronomy, 38, 249

Rauscher, E., Menou, K., Y-K. Cho, J., Seager, S., & Hansen, B. M. S. 2008, *ApJ*, 681, 1646

Redfield, S., Endl, M., Cochran, W. D., & Koesterke, L. 2008, *ApJL*, 673, L87

Rein, H., & Tamayo, D. 2015, *MNRAS*, 452, 376

Ricker, G. R., et al. 2015, Journal of Astronomical Telescopes, Instruments, and Systems, 1, 014003

Rizzuto, A. C., Mann, A. W., Vanderburg, A., Kraus, A. L., & Covey, K. R. 2017, *AJ*, 154, 224

Rodriguez, J. E., Vanderburg, A., Eastman, J. D., Mann, A. W., Crossfield, I. J. M., Ciardi, D. R., Latham, D. W., & Quinn, S. N. 2018, *AJ*, 155, 72

Rogers, L. A. 2015, *ApJ*, 801, 41

Sagan, C., Thompson, W. R., Carlson, R., Gurnett, D., & Hord, C. 1993, *Nature*, 365, 715

Sahlmann, J., Lazorenko, P. F., Ségransan, D., Martín, E. L., Queloz, D., Mayor, M., & Udry, S. 2013, *A&A*, 556, A133

Serrano, L. M., Barros, S. C. C., Oshagh, M., Santos, N. C., Faria, J. P., Demangeon, O., Sousa, S. G., & Lendl, M. 2018, *A&A*, 611, A8

Sheets, H. A., & Deming, D. 2017, *AJ*, 154, 160

Showman, A. P., & Guillot, T. 2002, *A&A*, 385, 166

Showman, A. P., Lewis, N. K., & Fortney, J. J. 2015, *ApJ*, 801, 95

Shporer, A., et al. 2017, *ApJL*, 847, L18

Sing, D. K. 2010, *A&A*, 510, A21

Sing, D. K., et al. 2015, *MNRAS*, 446, 2428

Soter, S. 2006, *AJ*, 132, 2513

Steffen, J. H., & Hwang, J. A. 2015, *MNRAS*, 448, 1956

Stephenson, C. B. 1986, *AJ*, 91, 144

Struve, O. 1952, The Observatory, 72, 199

Sullivan, P. W., et al. 2017, *ApJ*, 837, 99

Tamayo, D., Rein, H., Petrovich, C., & Murray, N. 2017, *ApJL*, 840, L19

Teske, J. K., Wang, S., Wolfgang, A., Dai, F., Shectman, S. A., Butler, R. P., Crane, J. D., & Thompson, I. B. 2018, *AJ*, 155, 148

Todoran, I., & Roman, R. 1992, Astronomische Nachrichten, 313, 315

Tsiganis, K., Gomes, R., Morbidelli, A., & Levison, H. F. 2005, *Nature*, 435, 459

Van Cleve, J. E., et al. 2016, Kepler Data Characteristics Handbook, Tech. rep.

van de Kamp, P. 1969, *AJ*, 74, 757

Van Eylen, V., & Albrecht, S. 2015, *ApJ*, 808, 126

Van Eylen, V., et al. 2016, *ApJ*, 820, 56

van Leeuwen, F. 2007, *A&A*, 474, 653

Vanderburg, A., & Johnson, J. A. 2014, *PASP*, 126, 948

Vanderburg, A., et al. 2015, *Nature*, 526, 546

—. 2016, *ApJS*, 222, 14

Vida, K., Kővári, Z., Pál, A., Oláh, K., & Kriskovics, L. 2017, *ApJ*, 841, 124

Weiss, L. M., & Marcy, G. W. 2014, *ApJL*, 783, L6

White, T. R., et al. 2017, *MNRAS*, 471, 2882

Winn, J. N. 2010, ArXiv e-prints

Wittenmyer, R. A., Endl, M., Cochran, W. D., & Levison, H. F. 2007, *AJ*, 134, 1276

Wolszczan, A., & Frail, D. A. 1992, *Nature*, 355, 145

Wong, I., et al. 2016, *ApJ*, 823, 122

Wood, B. E., Müller, H.-R., Zank, G. P., Linsky, J. L., & Redfield, S. 2005, *ApJL*, 628, L143

Xu, W., & Lai, D. 2017, *MNRAS*, 468, 3223

Yee, S. W., Petigura, E. A., & von Braun, K. 2017, *ApJ*, 836, 77

Yu, L., et al. 2018, ArXiv e-prints

Zacharias, N., Finch, C. T., Girard, T. M., Henden, A., Bartlett, J. L., Monet, D. G., & Zacharias, M. I. 2013, *AJ*, 145, 44